

Department of Space Physics, Institute of Experimental Physics,

Slovak Academy of Sciences, Košice, Slovakia

Authors: Simon Mackovjak, Pavol Bobík, Marián Putiš

ESA Contract No: 4000117740/16/NL/NDe

# **Feasibility study to observe ionospheric disturbances by one pixel UV detector**

**Final report**

1. Introduction .....	3
2. Airglow study – time and space dynamic of airglow production (WP2).....	4
2.1 Global maps production and optimal observation points selection .....	4
2.1.1 Simulations with empirical input parameters.....	4
2.1.2. Simulations for non and very disturbed magnetosphere .....	9
2.2 Airglow production and analysis of magnetospheric disturbances.....	13
2.2.1. Slope method.....	15
2.2.2. Preceding time window in Slope method analysis.....	21
2.2.3. Slope method dependency on Solar cycle.....	24
3. Study of radiative transfer in Earth's atmosphere (WP3).....	27
3.1.1 Selection of radiative transfer tool .....	27
3.1.2 Effect of atmospheric properties to the radiative transfer.....	29
3.1.3 Estimation of clear sky probability .....	41
3.1.4 Influence of starlight and zodiacal light.....	42
3.1.5 Overview of successful detections of space weather impacts in airglow measurements by other authors.....	43
3.2.1 The airglow spectra time series for proposed observational sites.....	44
3.2.2 The Optimal wavelength range for geomagnetic storms detection.....	50
4. Data analysis review (WP4).....	52
4.1.1 Description of the airglow monitor detector prototype.....	52
4.1.2 Selection of the suitable data for the analysis .....	53
4.1.3 Analysis of AMON measurements – general view .....	59
4.1.4 Analysis of AMON measurements - detailed view .....	63
4.1.5 Statistical analysis of UV airglow data .....	71
5. Programmatic section.....	75
6. Conclusion .....	77
References .....	79

# 1. Introduction

The geographical and time variability of night-time airglow light that is produced in lower ionosphere is still among not well understood phenomena. The influence of the solar cycle, magnetospheric disturbances, and changes in Earth atmosphere to the airglow emission are not sufficiently measured and described. The objective of the project is a study of the night-time UV airglow models and data with the aim to realize feasibility study of ionospheric disturbances observation by one pixel UV detector. The available models for UV airglow production and radiative transfer in the Earth's atmosphere are analyzed and data are compared with the measurements of relatively simple and inexpensive ground-based one pixel UV detector.

The project is divided into four Work packages. First work package (WP1) is management and reporting package that provided information about the work progress in the project. The second work package (WP2) is described in Section 2 and it contained simulations of global airglow production. Based on these simulations, the global airglow production maps were generated and optimal points for observation of changes in airglow production induced by geomagnetic disturbances were selected. Development of statistical method quantifying an effect of geomagnetic disturbances to simulated airglow production data was realized also during WP2. The third work package (WP3) is described in Section 3 and it consisted of the study of radiative transfer models from top of the atmosphere to the ground and analysis if the variations of atmospheric conditions might preclude the detection of ionospheric disturbances by observation of airglow intensity with one pixel UV detector. The calculations of overall spectrum (airglow spectrum + zodiacal light spectrum + star light spectrum) and radiative transfer for the seven locations selected in WP2 were also performed. The fourth work package (WP4), described in Section 4, included data processing and data analysis of one pixel UV detectors that were operated within the separated activity. The connections to the ionospheric disturbances caused by geomagnetic storm were indicated in several cases of one pixel UV detector measurements. But it was not possible to achieve clear evidence of feasibility with satisfactory statistics due to low geomagnetic activity.

## 2. Airglow study – time and space dynamic of airglow production (WP2)

### 2.1 Global maps production and optimal observation points selection

To select optimal positions for observation of geomagnetic disturbances effects in the airglow light production, two main categories of simulations were done. The simulation with empirically measured input values and simulations with typical values for very disturbed and non disturbed magnetosphere.

#### 2.1.1 Simulations with empirical input parameters

The maps of airglow production over the globe was produced for the 25 years from the year 1970 till the year 1994. The airglow intensities were evaluated in AURIC model (Atmospheric Ultraviolet Radiance Integrated Code, Strickland (1999)) for empirical/measured input parameters (i.e. Ap indexes, F10.7 index and geomagnetic coordinates).

Maps cover the globe with 10 degrees grid latitudinal and longitudinal step. All results presented in this study are evaluated for night hours when Sun is enough deep under the local horizon, i.e. for night hours when Sun zenith angle is higher than 110°. The example of airglow light production map in wavelength range 300-500 nm for 23:00 UT 9. January 1980 is presented in the Figure 2.1.1.

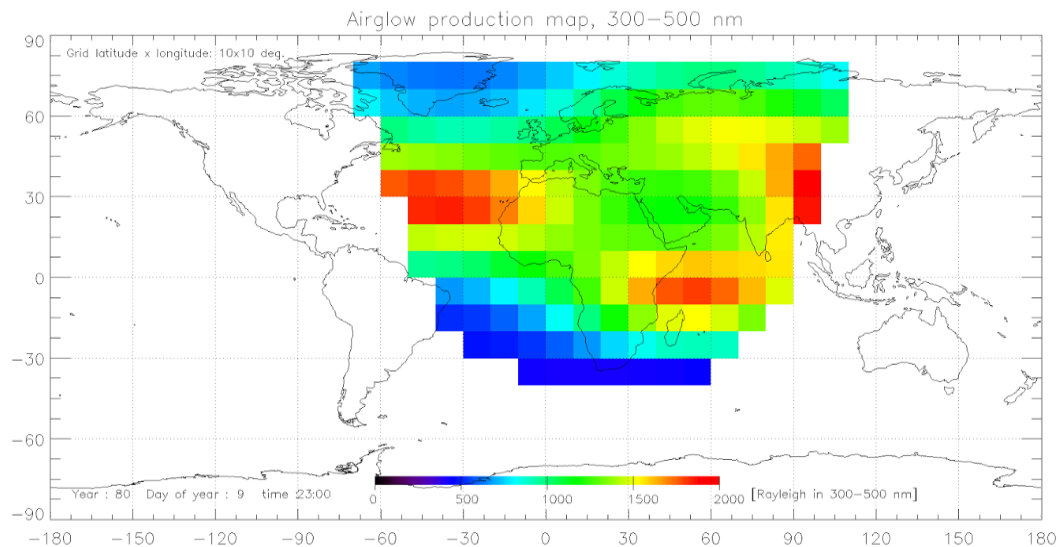
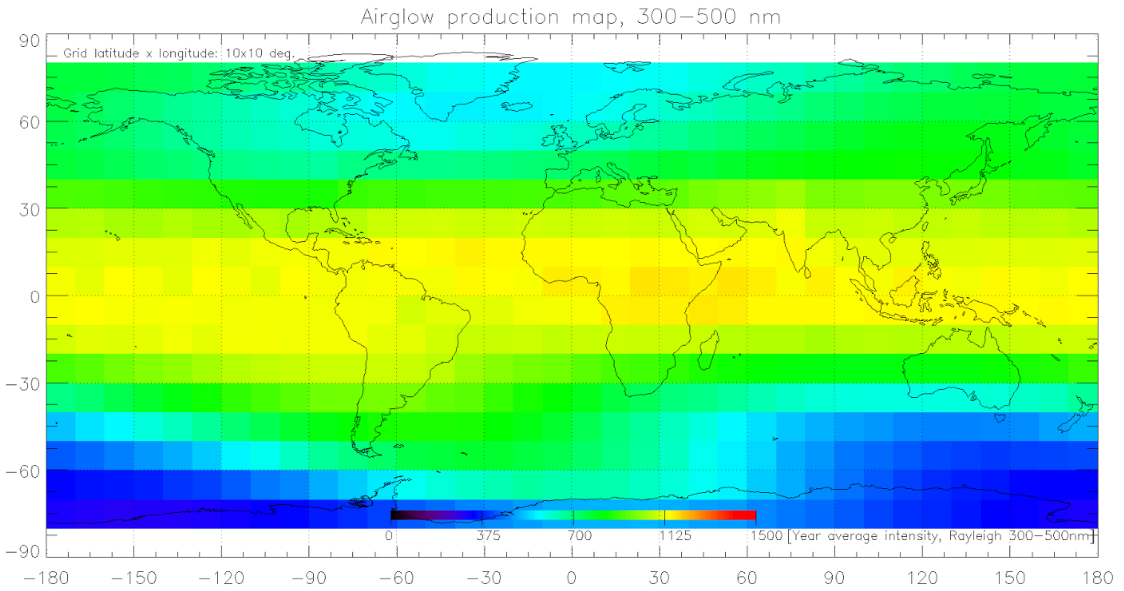


Figure 2.1: Airglow production at 9. January 1980, 23:00 UT, in the wavelength range 300-500 nm.

The Figure 2.1 displays airglow light production on different geographical positions in the Earth night regions where the Sun is more than 20 degrees under the local horizon. The maximum production in some regions is few times higher than in the most dark regions.

Airglow intensities were evaluated for one whole night in every month, i.e. for 12 nights per year at every point of grid. In summary 7 200 maps were evaluated, 288 for every year (12 nights x 24 hours) of tested 25 years long period.



*Figure 2.2: Airglow light production average for year 1980 (see text for details).*

The map of average intensities in the year 1980 presented in Figure 2.2 displays airglow production averaged from all night hours during the evaluated 12 nights. Figure illustrates geographical dependence of airglow light production. The production in the wavelength range 300-500 nm is the highest in the equatorial regions.

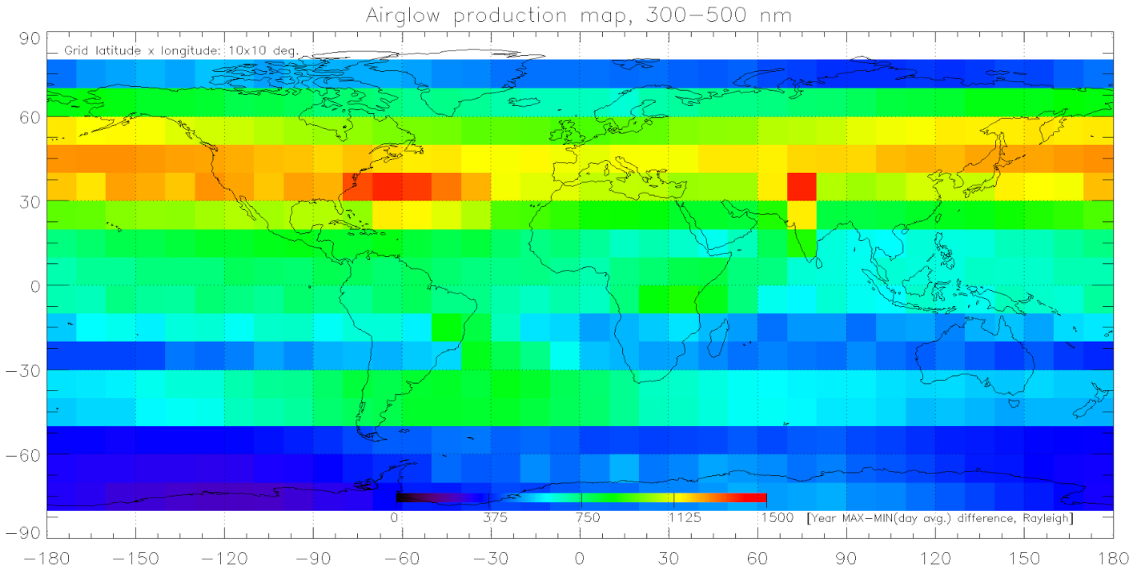


*Figure 2.3: Seasonal variation of airglow light production in the year 1980.*

In the Figure 2.3 we show map of seasonal changes in the airglow light production. The averaged night intensities was used and difference between nights with maximal and minimal intensity values during the year is presented. Figure indicate that seasonal variation is strongest in the middle latitudes of north hemisphere.

The one of two most visible characteristics in the produced maps is seasonal, one year long, variation of airglow intensity. Figure 2.4 displays two examples of seasonal variation on the positions with longitude 0 degrees and latitudes 0 and 40 degrees. Points in the figure are averaged night intensities. As figure illustrates, the airglow production also shows clear dependence on a solar cycle. The solar sunspot numbers are presented in the figure by the black line.

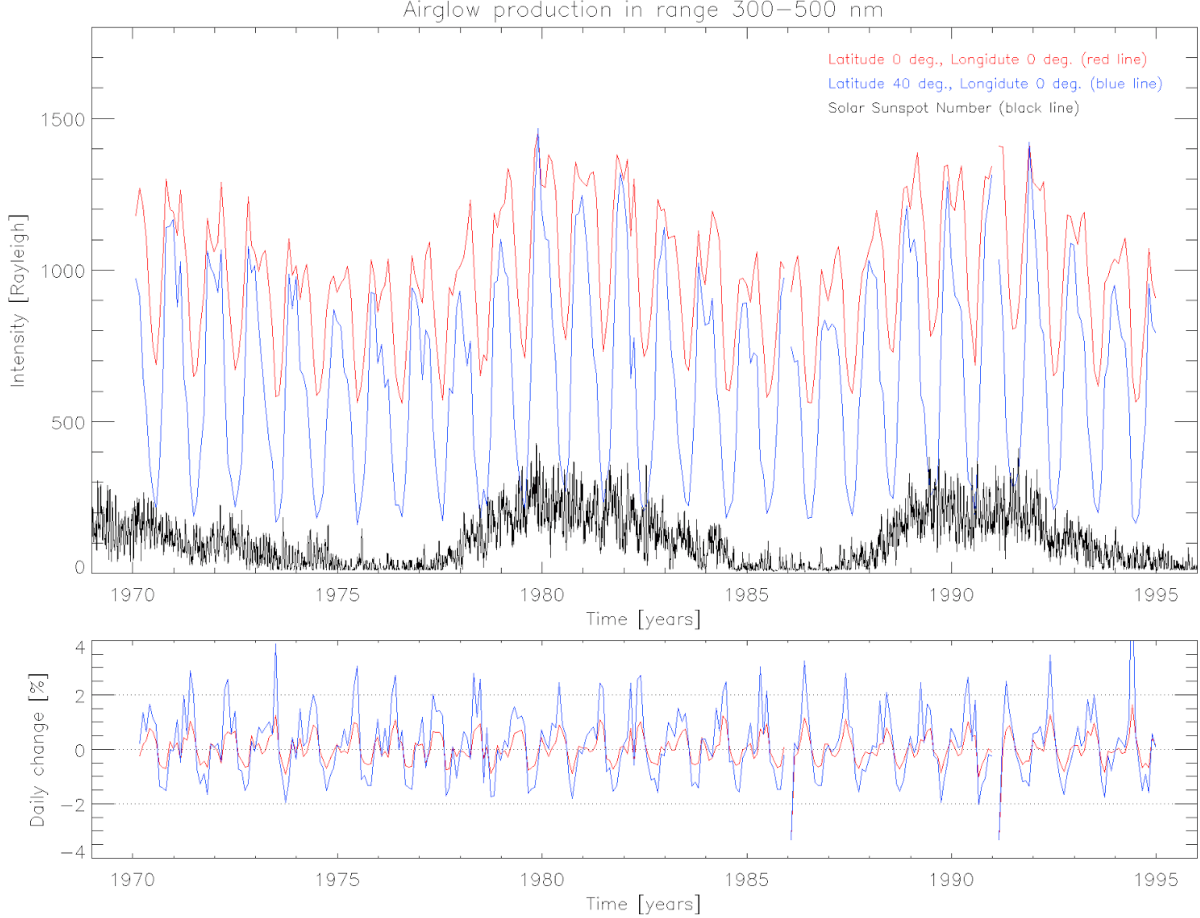


*Figure 2.4: Upper panel shows airglow light production on two positions. Equatorial position (latitude 0°, longitude 0°) intensities are denoted by red line, middle latitude position (lat. 40°, lon. 0°) by blue line. Bottom panel shows average changes of intensity during one day due to seasonal variation.*

The seasonal and night variation in airglow production timelines are smoother in the periods with undisturbed magnetosphere. The magnetospheric disturbances create noise on the timelines of airglow production.

The knowledge of temporal evolution of airglow intensities is useful to distinct them from the changes created during magnetospheric disturbances. The seasonal variation is smooth and slow in comparison to variations caused by geomagnetic events. Seasonal variation on daily basis has one order of magnitude smaller size in comparison with changes from disturbances. Seasonal variation changes airglow intensity during one day in most cases less than 2 % (see bottom panel of Figure 2.4). Expected changes in airglow production from geomagnetic disturbances reach several tens percents for strong storms (see section 2.2) on similar time scale. Night variation in the case of non disturbed period have predictable shape and is relatively smooth. Geomagnetic event will be

observable by comparison of consequent nights intensities and also by analyzing timeline shape of night radiation. Figure 2.5 represents example of night variation for several consecutive days at randomly selected position ( $-45^{\circ}$ ,  $170^{\circ}$ ) for low disturbed period. The Dst index (Sugiura, 1991; WDC Kyoto) during presented 4 days long period changes in the range from -7 nT to 24 nT.

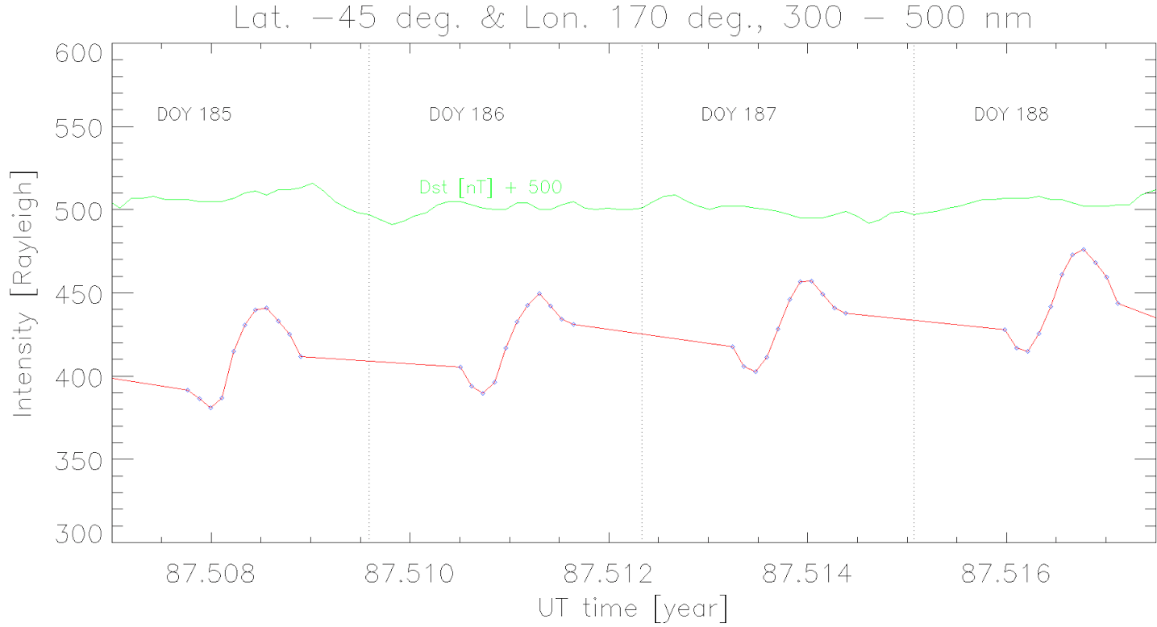


*Figure 2.5: Airglow production at the position with latitude  $-45^{\circ}$  and longitude  $170^{\circ}$ . Time is in the UT and DOY (day of the year) is shown in the figure. Dst index in units nT+500 is signed by green line to show that presented period was undisturbed.*

The nights airglow production variation together with changes created by disturbances in 25 years long tested period are presented in the figure 2.6. The histogram shows relative deviations from averaged night intensities for all geographical grid positions. The changes vary from 0 to more than 100 %. The histogram describes situations over the globe. To see geographical dependency we created a maps presented in side and bottom panels of the Figure 2.6. Small changes shown in 0-10%, 20-30% and 40-50% maps are concentrated in the equatorial and low latitude positions. Higher changes are concentrated in the high latitudes (maps for 60-70% and 80-90%). Figure 2.6 indicates better sensitivity to disturbances at higher latitudes. Because we see here situation which mix night and disturbance variabilities, we created sets of maps presented in the section 2.1.2. Figure 2.7 presents the same histogram and maps created from the set of maps where magnetosphere was undisturbed. From figure 2.7 we could see that changes from the night variations reach values 50%. Those are smaller than in previous histogram. The highest night variations are in the equatorial region. This is a further support argument that geomagnetic disturbances have better observability in airglow in higher latitudes.

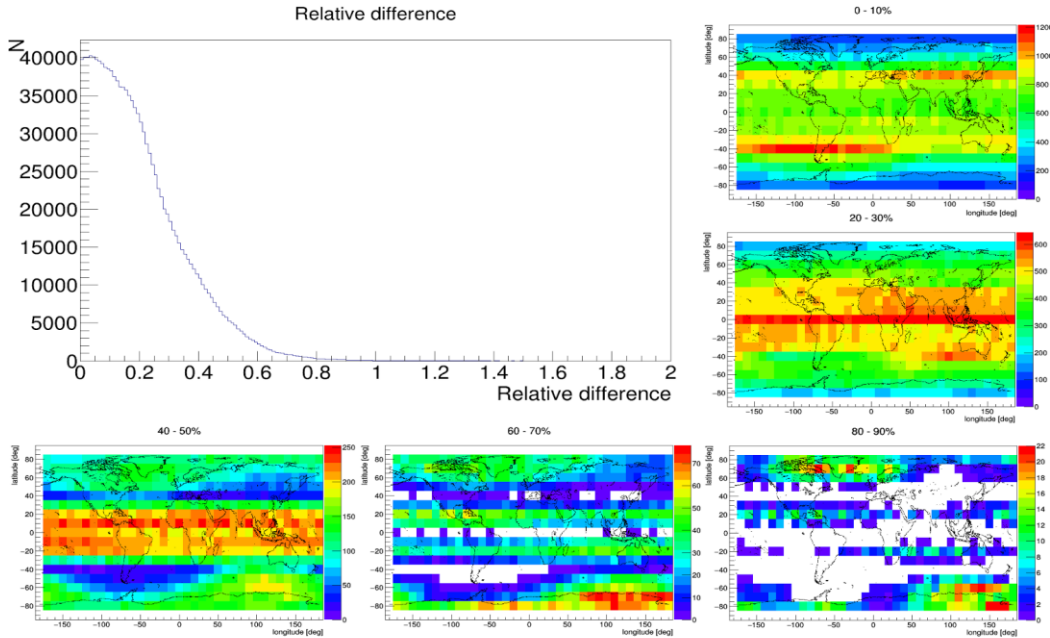


*Figure 2.6: Top left: Histogram of hourly relative deviations from averaged night intensities for all geographical grid positions. Deviations reached more than 100%. Top right and bottom: For given relative deviations interval histograms shows number of occurrences for each position at map. Relative deviations are for period between 1970 and 1994 for real empirical input parameters of Ap. Figures show mixed night and disturbance variabilities.*

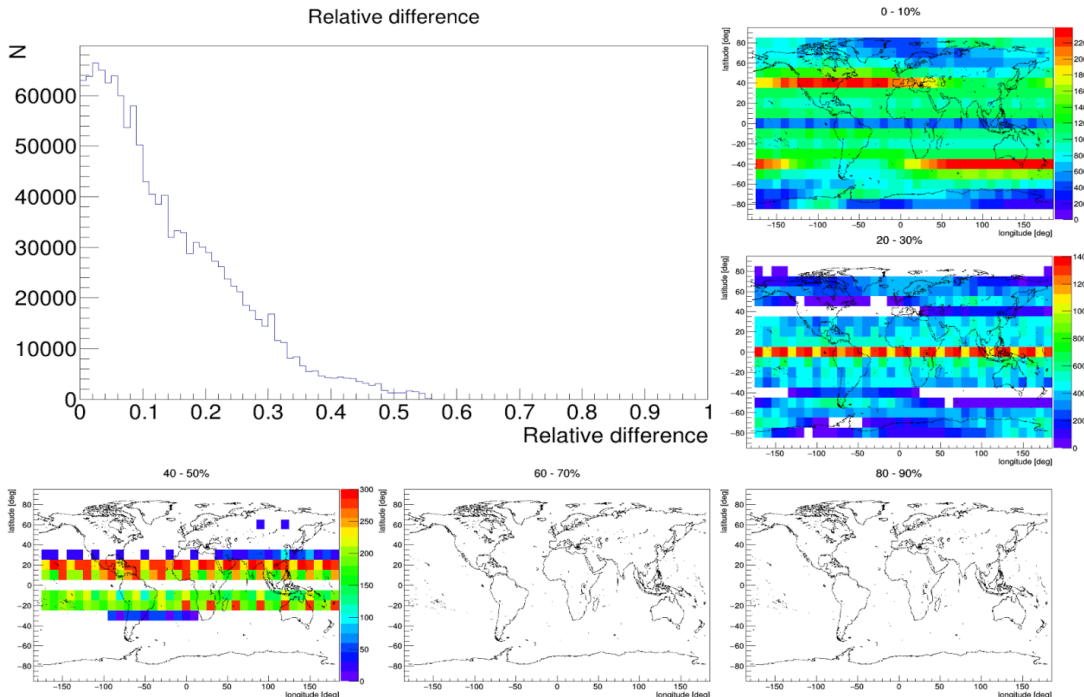


*Figure 2.7: Top left: Histogram of hourly relative deviations from averaged night intensities for all geographical grid positions. Deviations reached ~ 60%. Top right and bottom: For given relative deviations interval histograms show number of occurrences for each position at map. Relative deviations are for period between 1970 and 1994 for Ap=0. Figures show night variabilities.*

## 2.1.2. Simulations for non and very disturbed magnetosphere

To more clearly distinguish variations of airglow production presented in undisturbed periods from those created by the magnetospheric storms we evaluated maps for non disturbed and very disturbed situation.

For the same 25 years long period (1970-1994) we produced two sets of maps with identical time step and geographical grid as in previous case, both with constant geomagnetic and solar F10.7 indices over the whole tested period. First set has parameters for geomagnetically undisturbed periods ( $Ap=0$ ), second for very disturbed periods ( $Ap=250$ ). F10.7 is constant at value 140 for both calculations to prevent its influence. First set shows temporal airglow production in the Earth atmosphere not influenced by magnetospheric disturbances. Second set shows very disturbed situation. The comparison between both sets shows the most sensitive regions to geomagnetic disturbances in sense of airglow light production. The Figure 2.8 displays average decreases/changes of airglow production between non disturbed and very disturbed situation. Average decrease/changes on one grid point is average of hourly differences between airglow intensity when  $Ap=0$  and intensity when  $Ap=250$  from 25 years long period and is expressed as:

$$Average\ changes = \frac{1}{N} \sum_{i=1}^N |(I_{iAp=0} - I_{iAp=250})| \quad (2.1)$$

where  $I$  is intensity of airglow in Rayleigh units and  $N$  is number of calculated nights hours for given position. Figure 2.8 shows that the effect of geomagnetic disturbances to airglow production is raising with increasing of geomagnetic latitude.

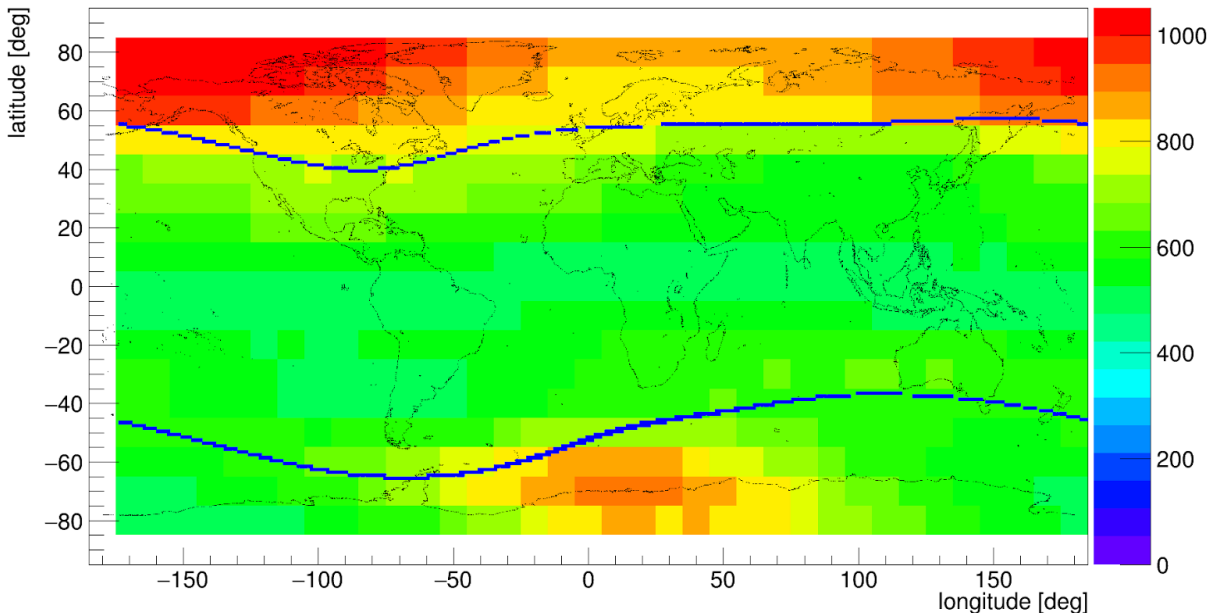


*Figure 2.8: Average changes (see formula (2.1) in the text) during period between 1970 and 1994.  
Blue lines represent borders of auroral oval at  $Kp=8$ .*

Relative average deviation is expressed as:

$$\text{Average relative deviation} = \frac{1}{N} \sum_{i=1}^N \frac{|(I_{iAp=0} - I_{iAp=250})|}{I_{iAp=0}} \quad (2.2)$$

and it shows similar scenario (Figure 2.9). Relative airglow production deviation during strong geomagnetic storm varies/changes from roughly 35 % in equatorial regions to over the 90 % in polar regions. The 100 % level are intensities during undisturbed periods with geomagnetic index Ap=0. Situation in relative scale is presented in the Figure 2.9.

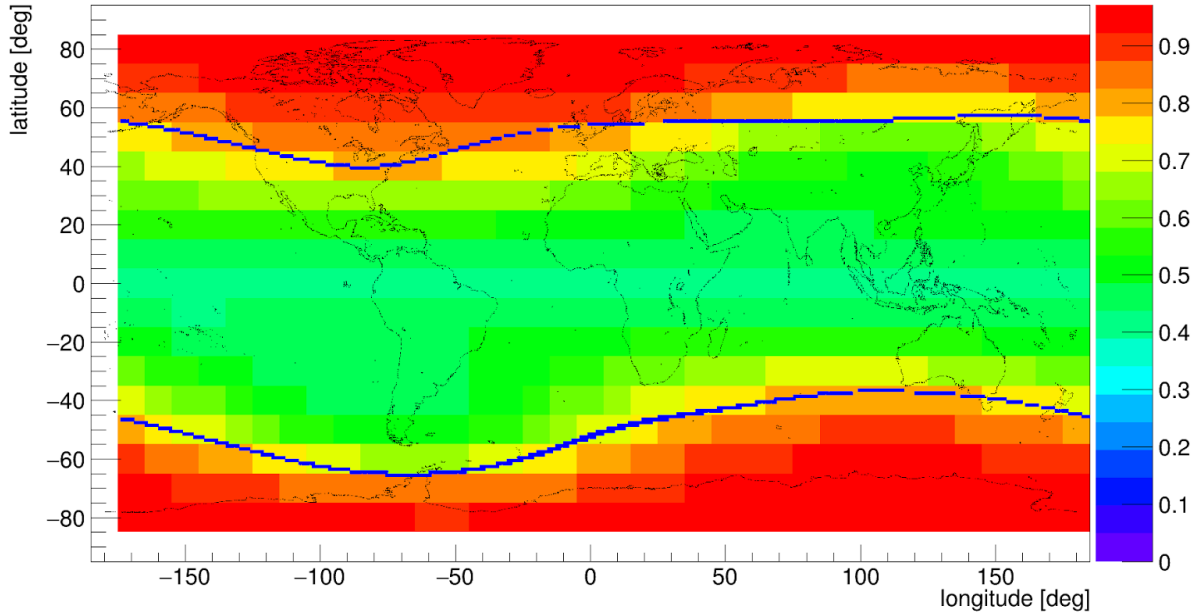


*Figure 2.9: Average relative deviation (see formula (2.2) in the text) during period between 1970 and 1994. Blue lines represent borders of auroral oval at Kp=8.*

The similar versions of Figure 2.9 were prepared also for separate relative deviation intervals (0-10%), (10-20%), ... (90,100%) and they are displayed in the Figure 2.10. This was done to confirm that averaging didn't mix regions with very low and very high relative deviation. However some degree of mixing is present, in general regions with highest relative deviation (60-100%) are relatively good separated from regions with low relative deviation (0-60%).

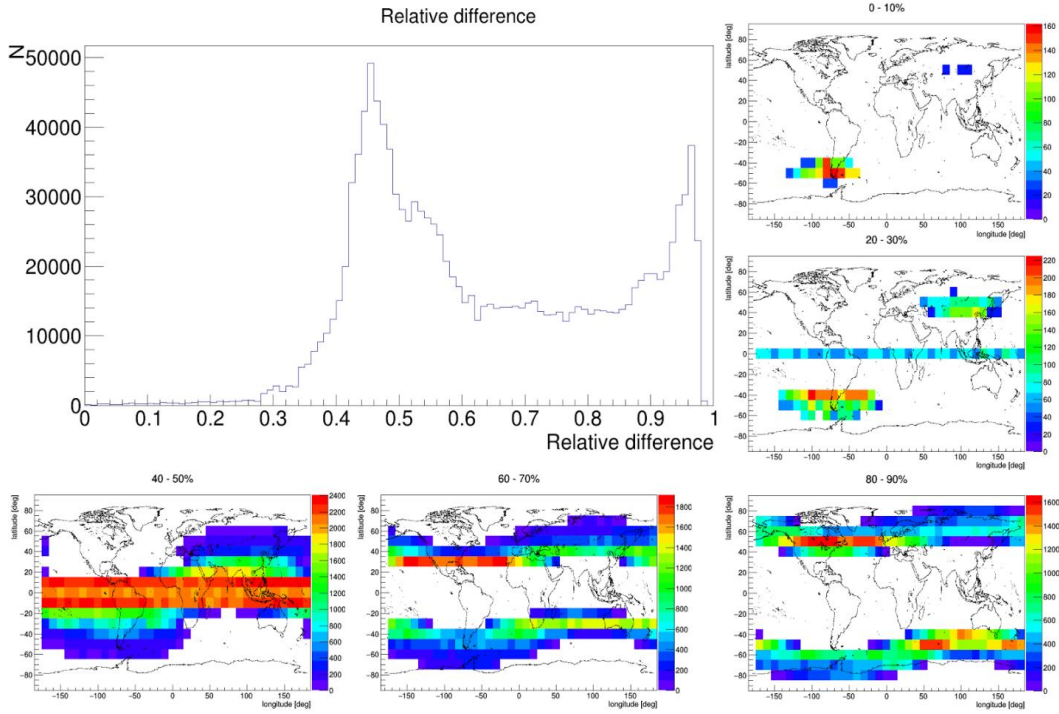


*Figure 2.10: Airglow sensitivity to magnetospheric disturbances. Top left: Histogram of relative deviation ( $Ap=0$  vs  $Ap=250$ ) for all geographical grid positions. Top right and bottom: For given interval, histograms show number of occurrences for each position at map. Relative deviations are for period between 1970 and 1994.*

Effect of variation in F10.7 index (increase of airglow emission with increase of F10.7) was also considered, because it has opposite effect than variation in Ap index (decrease of airglow emission with increase of Ap index). Same simulation as for Ap was done for F10.7. Two sets of maps for maximal and minimal value of F10.7, allowed by AURIC code was produced (with  $Ap=0$ ). Analysis showed that most of variations are at the level 20-40%. They are distributed mostly uniformly around the globe. We assume their effect is negligible to observation of geomagnetic disturbances. Minor fraction of disturbances in 40-60% interval is located mainly in the area between Australia and Antarctica.

The obtained results will suggest as best observational points those, with the highest geomagnetic latitudes. These points are most sensitive to geomagnetic disturbances and most stable with respect to time variation of airglow production. However, this will be limited by appearance of auroras in the polar regions. Light from auroras will hamper observation of airglow light. Taking in to account position of auroral oval for very disturbed periods ( $Ap=250$ ), we assume as meaningful points for disturbances observations in airglow light those on the most equatorward position/border of auroral oval. Ap index equal 250 approximately correspond to Kp index 8+. Position of auroral oval for Kp=8 is shown in the Figures 2.8. a 2.9. by blue lines. It is position with geomagnetic latitude 50.1 degrees.

Another strategy for observational points selection could be selection of positions more poleward. On the positions where auroral oval hamper observations for smaller disturbances than those with Kp=8. For example auroral oval position for Kp=6 is 54.2 degrees of geomagnetic latitude. On these positions, observed disturbances could be created by events with  $Kp \leq 5$ . Disturbances with  $Kp=5$  are much more often than disturbances with  $Kp=8$ .

As conclusion of presented result we choose as optimal points for observations those with highest possible geomagnetic latitude, where auroras do not hamper observations. In next part we will present simulations for selected 10 points around auroral oval position for Kp=8 at southern hemisphere and for another 10 points around auroral oval at northern hemisphere. It is reasonable to do simulations also for several points on higher (60 - 70 deg) and lower (20 - 30 deg) geomagnetic latitudes. This will help us understand in more details the response of airglow production to geomagnetic disturbances. On higher geomagnetic position observation will be hampered by auroral light during strong events, but this station could more easily register weaker disturbances. Simulations on lower geomagnetic positions could provide data which offer possibility to check validity of model (result that higher geomagnetic latitudes are suitable for observing geomagnetic disturbances) by comparing with real data.

Base on this conclusion we assume following positions for possible location of detectors: Three points could be located close to 51° of geomagnetic latitude (Slovakia, Utah, North of Poland/South of Sweden). Svalbard (Norway) could cover higher geomagnetic position and Canary Island cover lower geomagnetic position. We have also other candidates for detectors position which could be used alternatively: Zelenchukskaya District (Russia), Aragats (Armenia) and Pierre Auger Observatory (Argentina).

## 2.2 Airglow production and analysis of magnetospheric disturbances

In the analysis done during second part of the Work package 2 we evaluated airglow production at points selected in previous maps analysis (first phase of WP2). Those points include auroral oval position points and some other selected points for stations.

The airglow production at selected points was evaluated for 42 consecutive years (1970-2012) in wavelength range 300-500 nm. Simulations were done with one hour long time step for all days of checked period for moments/periods when Sun was more than 120 degrees under the local horizon. 120 degrees limit is limitation of AURIC model. As example of airglow production at one of selected positions we present in Figure 2.11. the model results for position Lomnický štit. The first one pixel UV detector was located in this position. The seasonal variation is very clearly present and visible in the figure. At the Lomnický štit position (latitude 49,20° N, longitude 20,22° E) airglow production is lower during the summer and higher during the winter. In part of the summer months at Lomnický štit latitude, Sun does not reach positions with zenith angle higher than 120 degrees. Thus model does not produce results in those nights. With stations located more to the south, like one on Canary Islands (Tenerife, latitude 28,76° N, longitude 17,89° W), we are at the position where the Sun always reaches the zenith angle higher than 120 degrees. The solar cycle with 11 years long variation is also visible in the figure. The airglow production is highest during the years of the solar maximum. The solar activity is in AURIC model represented by F10.7 index. The increase of airglow production is apparent in periods with high values of F10.7 index, what corresponds to the solar maxima.

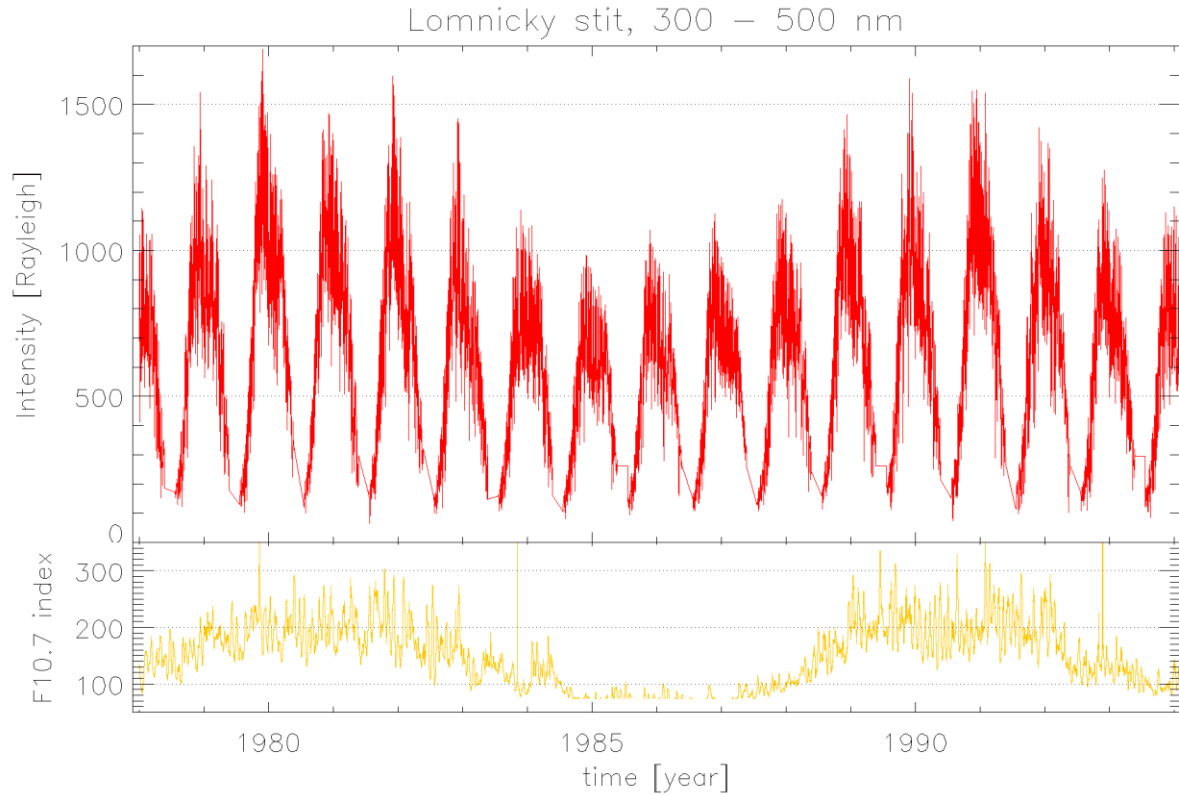


*Figure 2.11: Airglow production at Lomnický štit station in wavelength range 300-500 nm (upper panel). F10.7 index is presented at bottom panel.*

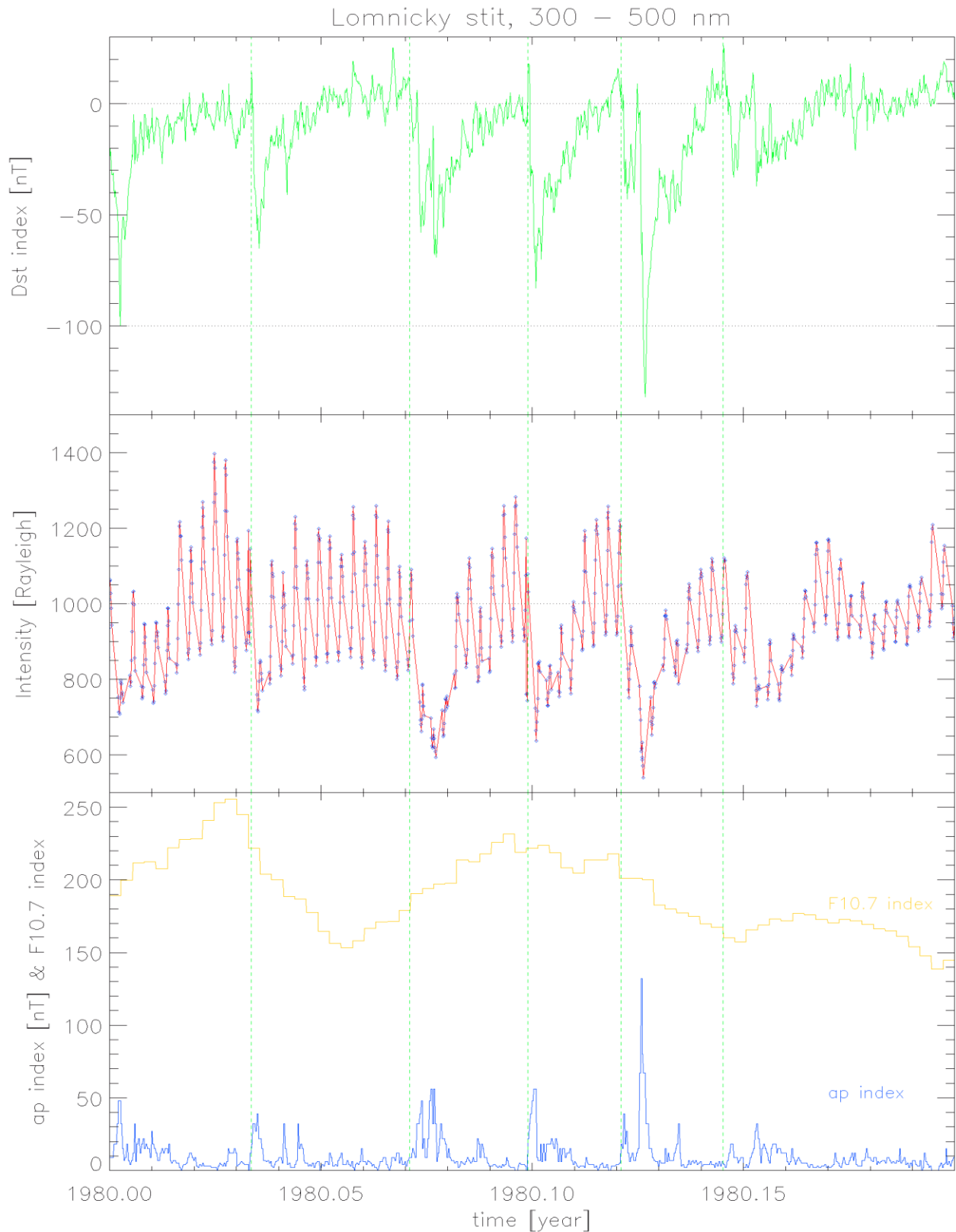


Figure 2.12: Dst index in the upper panel. Airglow production at Lomnický štit is presented in the middle panel. Indexes ap and F10.7 used by AURIC model are shown in the bottom panel.

With closer inspection of the Figure 2.11. the dependency of airglow production on geomagnetic activity could be identified. In the Figure 2.12 we present airglow production during the first 73 days of year 1980 in comparison with geomagnetic Dst index. The sharp decreases in Dst index followed by slow recovery phase in the figure are moderate geomagnetic storms (see top panel of Figure 2.12). The green dashed vertical lines sign start of 5 selected geomagnetic storms in the figure. The parallel decreases in Dst index and airglow production intensities are visible.

We use Dst index in the whole following analysis because Dst index is published with one hour time step. The Dst index is based on low latitude measurements. The Ap index is based on measurements from middle latitude stations. Comparison of analysis results for Ap and Dst index is added after the method description.

The appearance of geomagnetic storms effect in airglow light production is clearly seen in many cases. We used evaluated time series of airglow production to quantify connection between geomagnetic activity and airglow light production. We were looking for statistical method which clearly and effectively shows the effect of geomagnetic disturbances on airglow production. The simple comparison between intensity and geomagnetic indexes will mixes effect of storms with seasonal, daily/night variation and atmospheric disturbances. The seasonal variation, night variation and local atmospheric disturbances must be taken into account. The geomagnetic storm cause decreasing of airglow light intensity. The decreased values during the storm could be similar to intensities in different non-disturbed periods of the year. In other words decreases due to storms starting from different values of airglow intensity in different parts of year. To not compare periods with different airglow production due to seasonal variation, we use parameter which describe change of airglow production in comparison with preceding/previous days values. Length of this preceding/previous periods is tested to find optimal values where method is most sensitive.

Effect of seasonal variation to airglow is slow and smooth during the year, however apparent on longer time scales. This could have an effect on the statistical method used in this study in the case of using wide-long time window. On the other hand short periods (hours length) comparison of intensity with Dst index could lead to mixing of night variation with variation caused by storm. For this reason we focus on comparison of night averaged values with average from previous nights. Local atmospheric disturbances could carry in deviation to relationship between intensity and Dst index. This effect could be excluded by comparison of data from stations separated by long distance.

### 2.2.1. Slope method

In the used statistical method we evaluate changes in airglow night intensity by comparison with averaged intensity from preceding period. In method we compare averaged night intensities and geomagnetic activity index to limit/reduce influence of night variation effect in method. Averaged night values are

$$Dst_{AVG}(NOY) = \frac{1}{n} \sum_{i=1}^n Dst_{i,NOY}, I_{AVG}(NOY) = \frac{1}{n} \sum_{i=1}^n I_{i,NOY} \quad (2.3)$$

where  $Dst_{i,NOY}$  is i-th value of Dst index from selected night of the year (NOY). NOY is number of night in the year. First night in year starts at the evening of 1. january and ends at the morning of 2. january. Short form NOY is analogy to frequently used DOY (day of the year).  $I_{i,NOY}$  is i-th airglow

intensity in NOY. To night average  $I_{AVG}(NOY)$  are included  $n$  hours (hours which satisfy condition of  $SZA > 120$  degrees). Night average  $Dst_{AVG}(NOY)$  is calculated from same hours of night.

Because seasonal variation effect is relatively small during short periods (days or couple of weeks), changes in airglow intensities induced by storm could be compared with periods immediately precede them. For preceding period long  $m$  days we evaluate for every night values

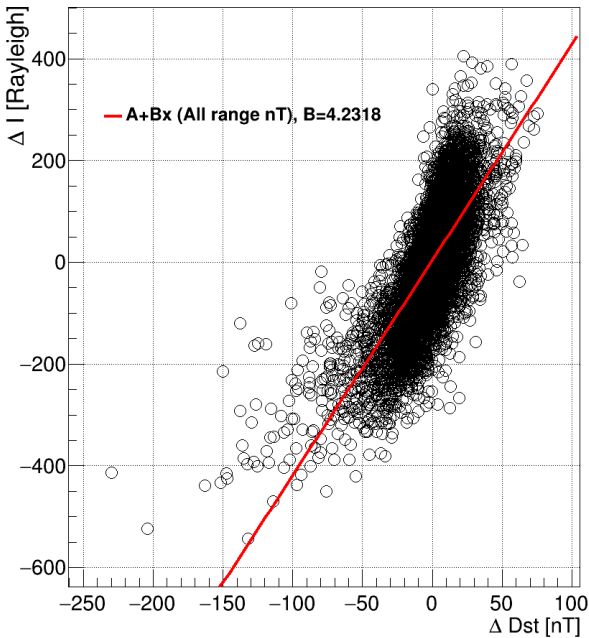
$$Dst_m(NOY) = \frac{1}{m} \sum_{j=NOY-1-m}^{j=NOY-1} \sum_{i=1}^{i=n} Dst_{j,i,NOY}, I_m(NOY) = \frac{1}{m} \sum_{j=NOY-1-m}^{j=NOY-1} \sum_{i=1}^{i=n} I_{j,i,NOY} \quad (2.4)$$

$$\Delta Dst(NOY) = Dst_{AVG}(NOY) - Dst_m(NOY), \Delta I(NOY) = I_{AVG}(NOY) - I_m(NOY) \quad (2.5)$$

where  $j$  is index signing  $m$  days long time window for NOY night,  $\Delta Dst$  (NOY) is absolute daily change of geomagnetic index  $Dst_{AVG}(NOY)$  in comparison with average  $Dst$  values in  $m$  previous nights.  $\Delta I$  (NOY) is absolute change of airglow production  $I_{AVG}(NOY)$  to average airglow production during previous  $m$  nights. Only periods when all nights are present, were taken into analysis. For example, summer gap in airglow production data for some higher latitude stations is not part of any used period.

In the figure 2.13 we show dependency of  $\Delta I$  (DOY) on  $\Delta Dst$  (DOY) for Lomnický štít station. Figure present comparison with  $m=5$  and  $m=10$  for 42 years from 1970 to 2012, where  $\Delta I$  (DOY) was evaluated only for nights longer than 3 hours ( $n>3$ ). Left panel shows  $\Delta I$  (DOY) vs.  $\Delta Dst$  (DOY) for  $m=5$ , right one for  $m=10$ , both show data for every night (4 hours and longer nights) in 42 years. Red line represent a linear fit of data  $\Delta I$  (DOY) =  $A + B \cdot \Delta Dst$ . The slope  $B$  has for  $m$  equal 5 and 10 values 4,23 and 4,17. Thus 1 nT change in  $\Delta Dst$  leads approximately to 4 times bigger change in  $\Delta I$  (DOY) in Rayleighs.  $B$  describe the level of sensitivity to geomagnetic disturbance expressed by geomagnetic index  $Dst$ . Because we use slope  $B$  as parameter which describe sensitivity of position to geomagnetic disturbances, we call used statistical method Slope method.

LS (lat 49.19,lon 20.21),  $m=5$



LS (lat 49.19,lon 20.21),  $m=10$

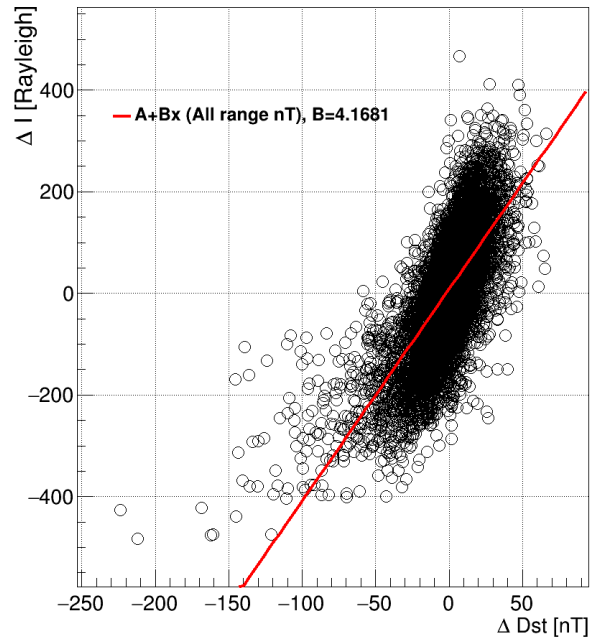


*Figure 2.13: Absolute changes in Dst index  $\Delta\text{Dst}$  in comparison with absolute changes in airglow production  $\Delta I$  for  $m=5$  (left panel) and  $m=10$  (right panel). On both panels are shown points for all days from checked period (see text for details).*

We evaluated B coefficient for m between 3 and 20 to find optimal length of period for detecting changes in airglow production induced by geomagnetic disturbances. Method for Lomnický štit shows similar sensitivity in range from 3 to 20 nights. Most sensitive to geomagnetic disturbances are 5 and 6 days long periods ( $m=5,6$ ). Table 2.1 shows B values evaluated for different m values.

The change of airglow production due to geomagnetic disturbance is approximately linear to change of geomagnetic field represented here by Dst index. According to results in Table 2.1 (2. column) the similar linear dependence could be found for comparisons with preceding periods long from 3 to 20 days. Used method compare airglow production changes by their absolute values. In the slightly modified method we take in account relative changes of airglow intensities. The relative  $\Delta I_R$  (NOY) is

$$\Delta I_R(\text{NOY}) = \frac{I_{\text{AVG}}(\text{NOY}) - I_m(\text{NOY})}{I_m(\text{NOY})} \quad (2.6)$$

The relative changes linear fits are presented in 3. column of Table 2.1. Example of data used for evaluation of slopes B for relative intensity changes are presented in Figure 2.14.

The relative changes in airglow intensity lead to qualitatively similar results as in previously presented results evaluated from absolute changes. The change of Dst index by one nT lead to change of airglow production at Lomnický štit position by ~0,6 %. For the moderate storm with Dst index going from values close to 0 nT to -50 nT it gives us in average 30 % decrease in airglow production. In Figure 2.14. we can see/notice that curve slope is not the same over the whole range of the  $\Delta\text{Dst}$  values. The negative  $\Delta\text{Dst}$  appear during the start phases of magnetospheric disturbances. In negative part of  $\Delta\text{Dst}$  axis we can see two subregions. First subregion with higher slope between smaller  $\Delta\text{Dst}$  values, in interval approximately from  $\Delta\text{Dst} = -50$  nT to  $\Delta\text{Dst} = 0$  nT. This is region of small changes in Dst index. We named region where  $\Delta\text{Dst} = [-50, 0]$  nT 1st interval and sign fit slope there as  $B_1$ . The interval with  $\Delta\text{Dst} > -50$  nT is interval with bigger changes in Dst index. We call this interval 2nd interval where name of fit slope is  $B_2$ . In 1st interval has slope  $B_1$  of fit higher value than  $B_2$  in 2nd interval. This is in fact positive thing for project, because those weaker events are more frequent than stronger events. We note, year 2017 was in declining phase of Solar activity directing toward solar minimum, when disturbances were weaker and less frequent.

*Table 2.1: Lomnický štit position, linear fit parameter B dependence on m parameter (see text for details).*

m [days]	Absolute changes, fit $\Delta I$ (DOY) = $A + B \cdot \Delta\text{Dst}$ $\Delta I$ (DOY) [Rayleigh] $\Delta\text{Dst}$ [nT]	Relative changes, fit $\Delta I_R$ (DOY) = $A_R + B_R \cdot \Delta\text{Dst}$ $\Delta I_R$ (DOY) [%] $\Delta\text{Dst}$ [nT]
	B	$B_R$
3	4.11	0.584
4	4.20	0.595
5	<b>4.23</b>	<b>0.598</b>
6	<b>4.23</b>	<b>0.598</b>
7	4.22	<b>0.598</b>
8	4.21	<b>0.598</b>

9	4.19	0.597
10	4.17	0.596
15	4.16	0.588
20	4.17	0.589

The  $\Delta I$  values with positive  $\Delta Dst$  values are mainly from storms recovery phases (later storm phases), when Dst index raise and consequently airglow production increase, too.

The Ap index is input parameter of AURIC model. However as 3 hours index, Ap index is less convenient to be used in comparison with real data than one hour Dst index. To show that both ap and Dst index give similar results in Slope method, we apply slope method to Ap index.  $\Delta Ap$  was evaluated in the same way as  $\Delta Dst$  used in the analysis. The result is presented in the Figure 2.15. We can see here very similar picture as we saw in analysis with  $\Delta Dst$ . In the Figure 2.15, analysis for Lomnický stit for 5 days long preceding time window is shown. Slope has reversal sign because Ap index raise during magnetospheric disturbances, what is opposite behaviour to Dst index which decrease to negative values during the storms. Consequently  $\Delta Ap$  is positive during the storms when  $\Delta I$  decrease and linear fits slope is negative. The slope B shows 0,7 percent change in airglow production for 1nT change in Ap index. Results are similar to analysis with Dst index. In the following analysis we use Dst index.

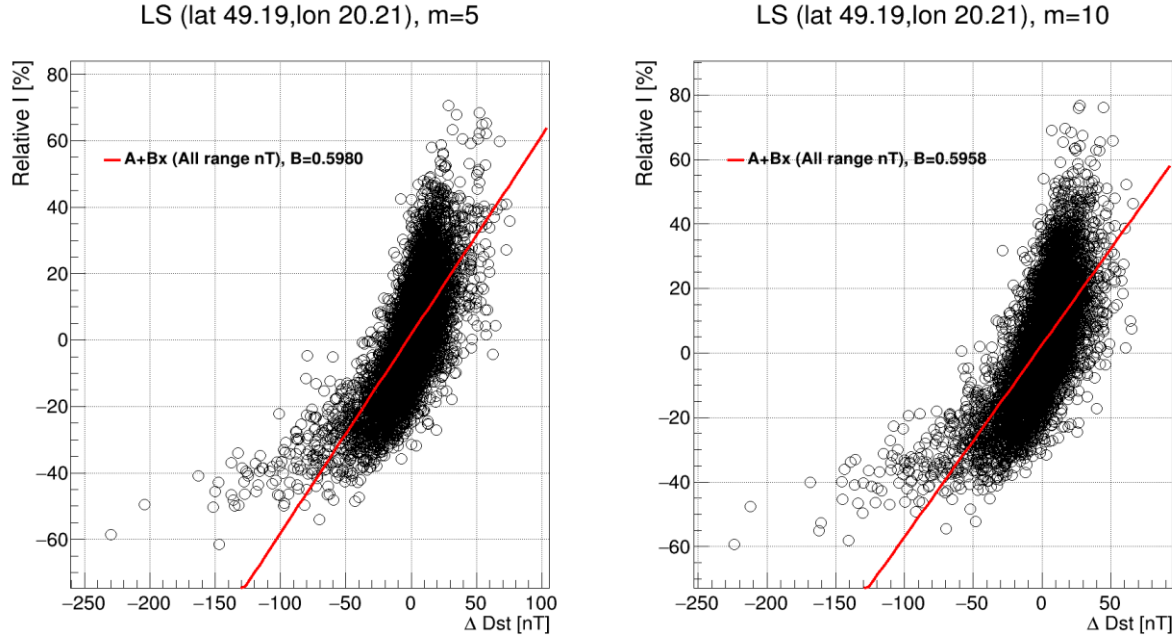
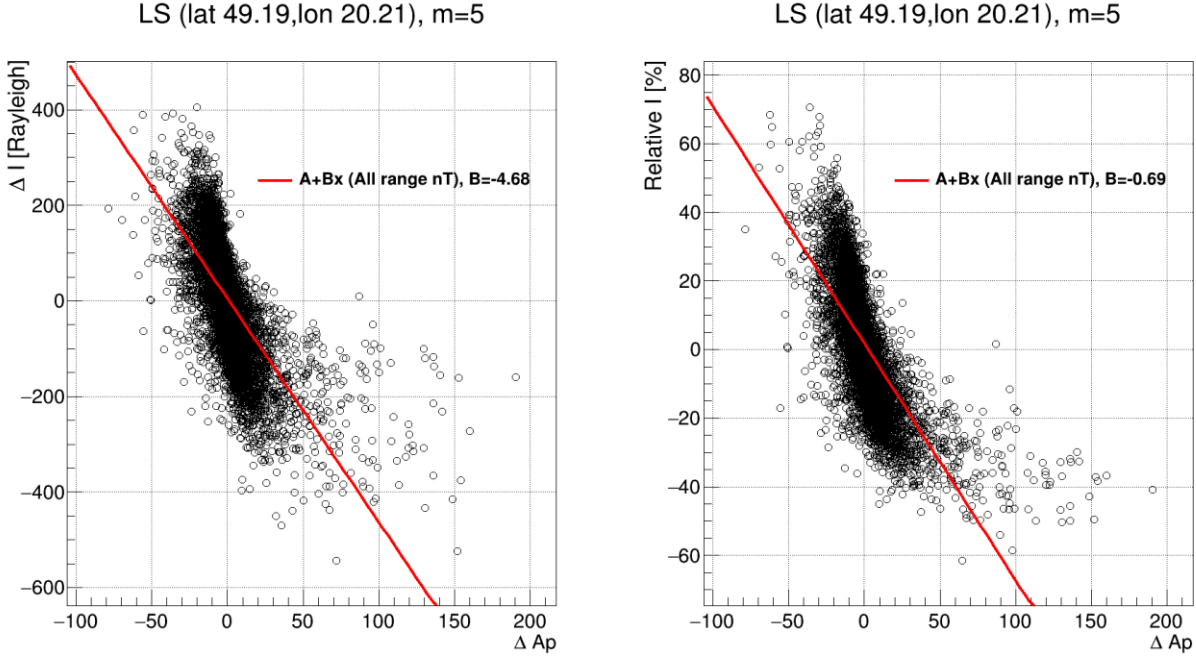


Figure 2.14: Absolute changes in Dst index  $\Delta Dst$  in comparison with relative changes in airglow production  $\Delta I$  for  $m=5$  (left panel) and  $m=10$  (right panel). Data on the panels shown points for all days from checked period.



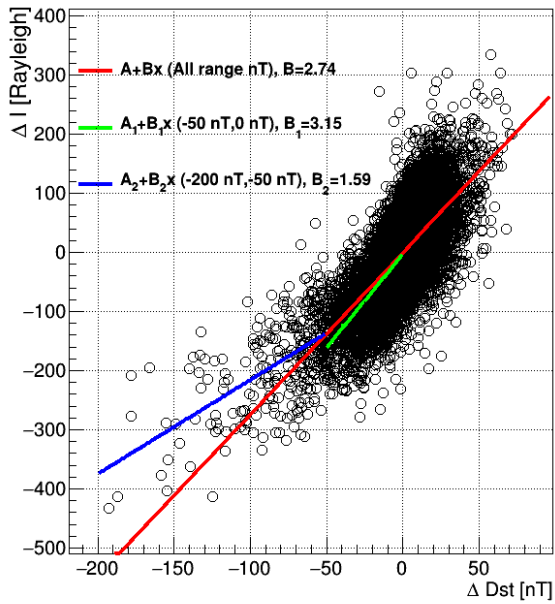
*Figure 2.15. Absolute changes in Ap index  $\Delta Ap$  in comparison with absolute (left panel) and relative changes (right panel) in airglow production for  $m=5$ . Data on the panels shown points for all days from checked period.*

In the Figure 2.16. we present four examples of Slope method results. Two for the auroral oval positions and two for selected positions Tenerife and Lomnický štít (LS hereafter). All four examples at figure are shown for 5 days long ( $m=5$ ) preceding time window. For Tenerife we found slope  $B_1$  in 1st interval with value 0.40, i.e. 0.4 percent change in airglow intensity for 1 nT change in  $\Delta Dst$ . Linear fit in 1st interval is denoted in green color. In the 2nd interval  $B_2$  slope has value 0,14 (blue color fit). Fit for whole interval of  $\Delta Dst$  values has  $B=0,34$  (red line in figure). At Lomnický štít we are more sensitive to  $\Delta Dst$  changes than in Tenerife. As it is shown in the second row of figure 2.16., in the 1st interval  $B_1=0,68$  and in 2nd interval  $B_2=0,20$ . All  $\Delta Dst$  values fit has slope  $B=0,60$ .

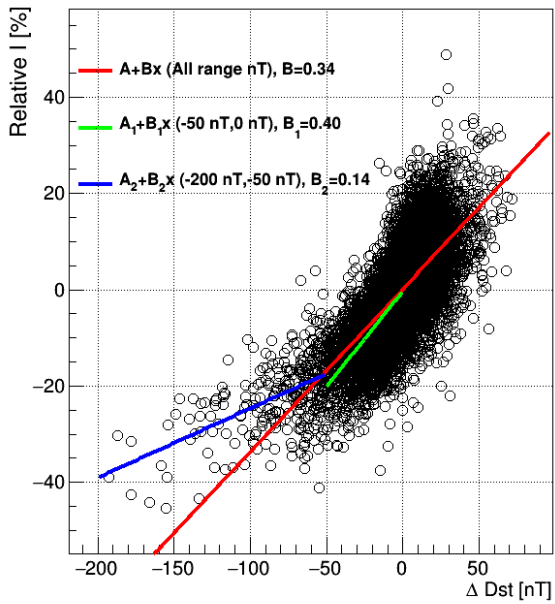
At third and fourth row of figure 2.16., we present Slope method results examples for two selected points at auroral oval (position of auroral oval for very disturbed situation with  $Kp=8$ ). The position selected at the north hemisphere with geographical latitude  $54^\circ$  at Prime meridian is more sensitive than LS position. Slope  $B_1$  in 1st interval has value 0,86. Position at auroral oval at southern hemisphere with same meridian with geographical latitude  $-52^\circ$  is less sensitive than LS.  $B_1$  slope here in 1st interval has value 0,65.

The B value, especially  $B_1$  in 1st interval we take as parameter describing sensitivity of airglow production at place to magnetospheric disturbances.

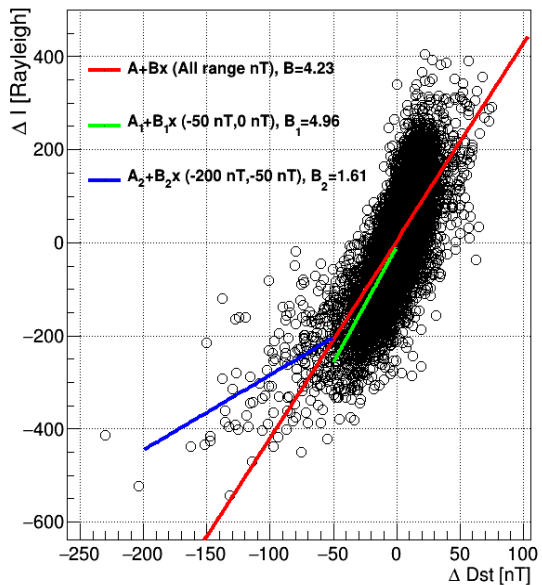
TENERIFE (lat 28.76,lon -17.89), m=5



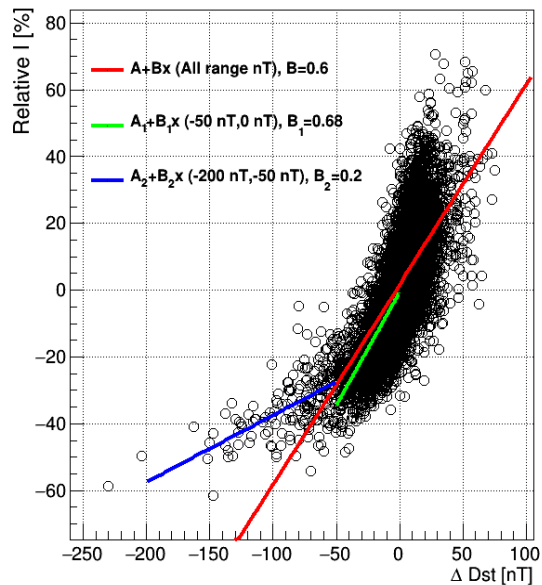
TENERIFE (lat 28.76,lon -17.89), m=5



LS (lat 49.19,lon 20.21), m=5



LS (lat 49.19,lon 20.21), m=5



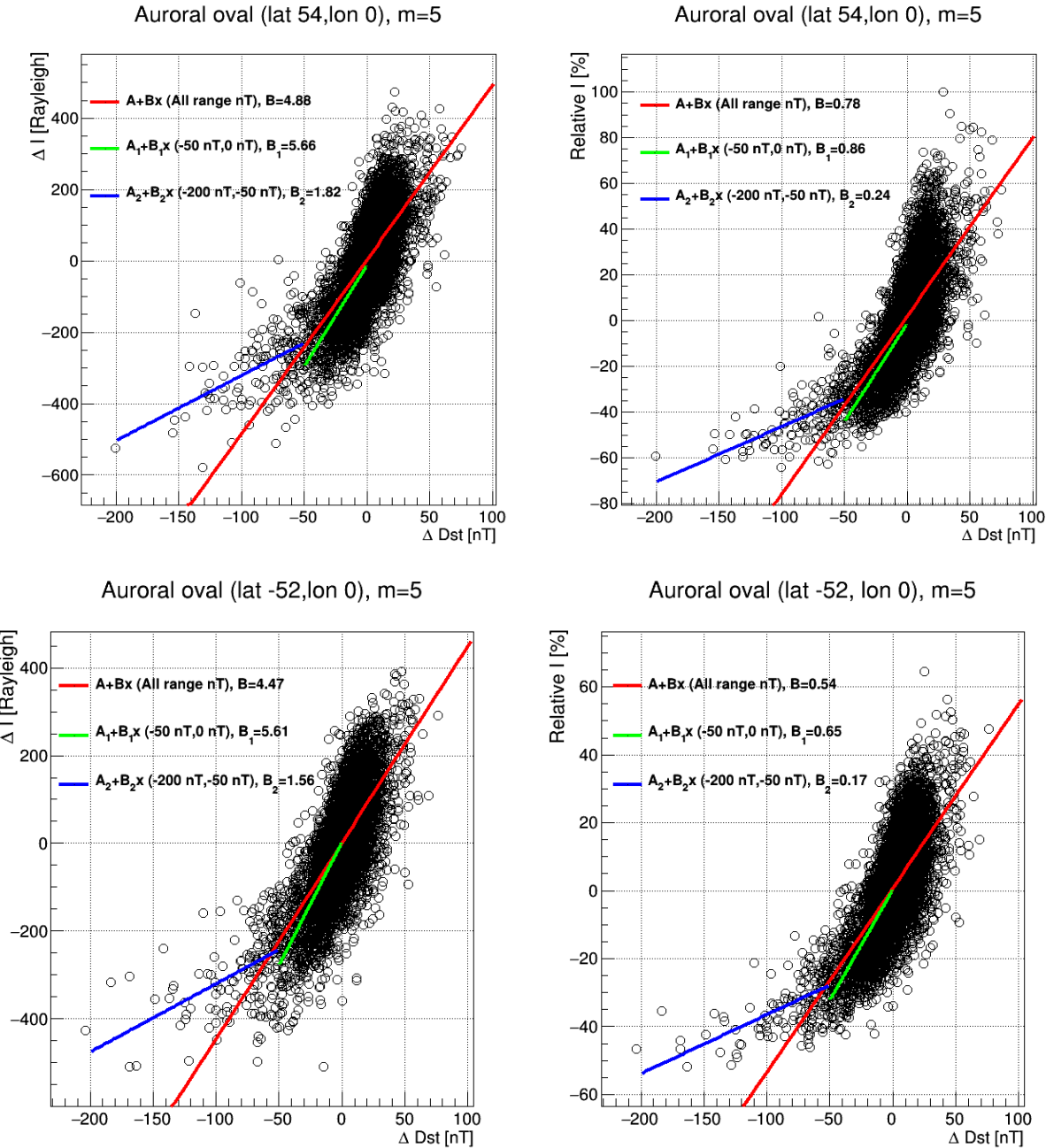


*Figure 2.16: Absolute changes in Dst index  $\Delta Dst$  in comparison with absolute (left panels) and relative changes (right panels) in airglow production  $\Delta I$ . Data on the panels are points for all days from checked period. In first two rows are presented model results for Tenerife and Lomnický stit position. Third and fourth row show positions on auroral oval (see text for the details).*

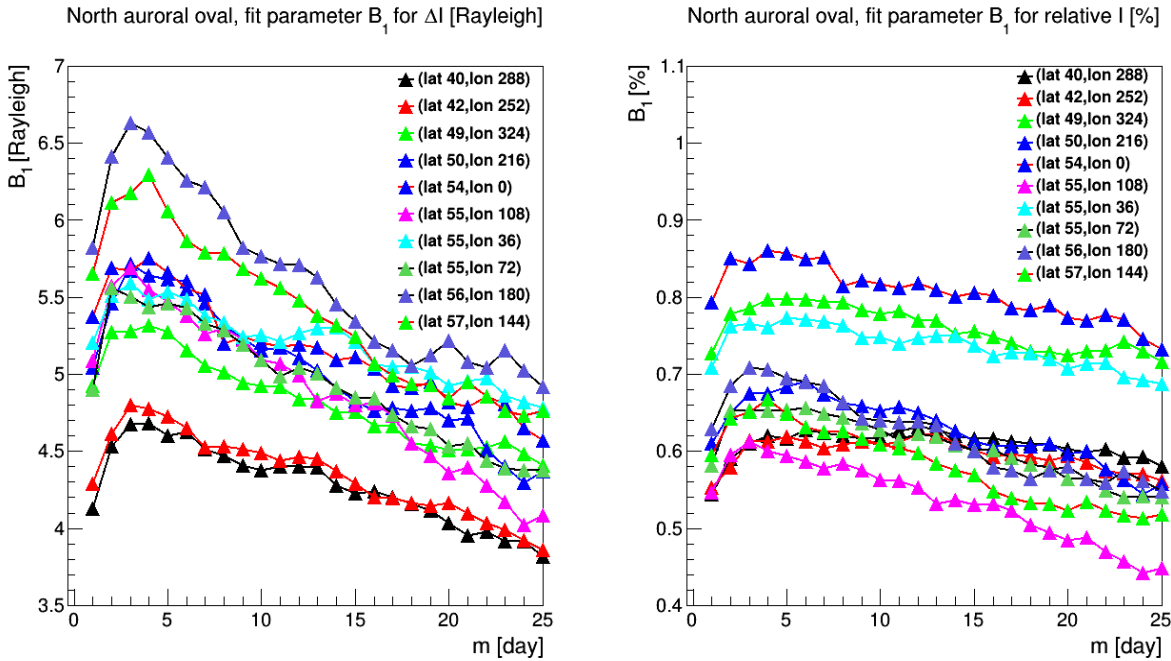
## 2.2.2. Preceding time window in Slope method analysis

The results from Slope method depend on preceding window length  $m$ . We evaluated the dependency of  $B_1$  slope in 1st interval at preceding period length  $m$  for six selected stations and ten points on north auroral oval and ten points on south auroral oval.  $B_1(m)$  value reach maximum for time window with length between 3 and 8 days, depending on position. After reaching maximum,  $B_1(m)$  slowly

decrease to values 10-20% smaller for 25 days long time window. The results are presented in figure 2.17.

On the first two rows of figure 2.17 we focus on the twenty auroral oval positions. Let us remind that those are positions with geomagnetic latitude  $50,1^\circ$ , what is auroral oval position for strong disturbed magnetosphere when Kp index reached value 8. The slope  $B_1$  of all positions for relative intensities (right panels) for  $m$  between 1 and 25 days has values between 0,45 and 0,85. This is change between 0,45 - 0,85 % in airglow intensity for 1nT change of  $\Delta Dst$  for 1 - 25 days long ( $m = 1 - 25$ ) time window. Sensitivity expressed by slope  $B_1$  is different for different positions. Differences in  $B_1$  slopes between positions on auroral oval are in 50 % range (maximum B value of all positions is 100%), when we look to most sensitive position and most unsensitive position. In position with highest values of  $B_1$  it is in range 0,75-0,85 for  $m = 1 - 25$  nights. In position with minimal values of  $B_1$  it is between 0,45-0,6.

On the third row of figure 2.17 are  $B_1(m)$  dependencies for 7 checked positions i.e. Aragat, Lomnický štit, Pierre Auger Observatory position, Svalbard, Tenerife, Utah, Zelenchukskaya. Taking as parameter of sensitivity  $B_1(m)$  most sensitive from selected periods is Svalbard position with geographical latitude  $78,90^\circ$ . (corrected geomagnetic coordinate in the year 2017 [VITMO model: [http://omniweb.gsfc.nasa.gov/vitmo/cgm\\_vitmo.html](http://omniweb.gsfc.nasa.gov/vitmo/cgm_vitmo.html)]). We tested Svalbard as one very north position, to have one position very sensitive to geomagnetic disturbances. But because Svalbard has geomagnetic latitude  $76,57^\circ$ , measurements here would be very often hampered by auroral lights. Second most sensitive position is Lomnický štit followed by position in Utah and Zelenchukskaya position. Those stations will observe auroral light only during extremely disturbed magnetosphere (with Kp=9). All seven stations show statistically clear situation, even if some are less sensitive than others.  $B_1$  slope has smallest values for Pierre Auger Observatory position.  $B_1$  slope for Auger position has values reaching 0,25. The relatively low sensitivity of Auger station is due to low geomagnetic latitude  $-21,57^\circ$ .



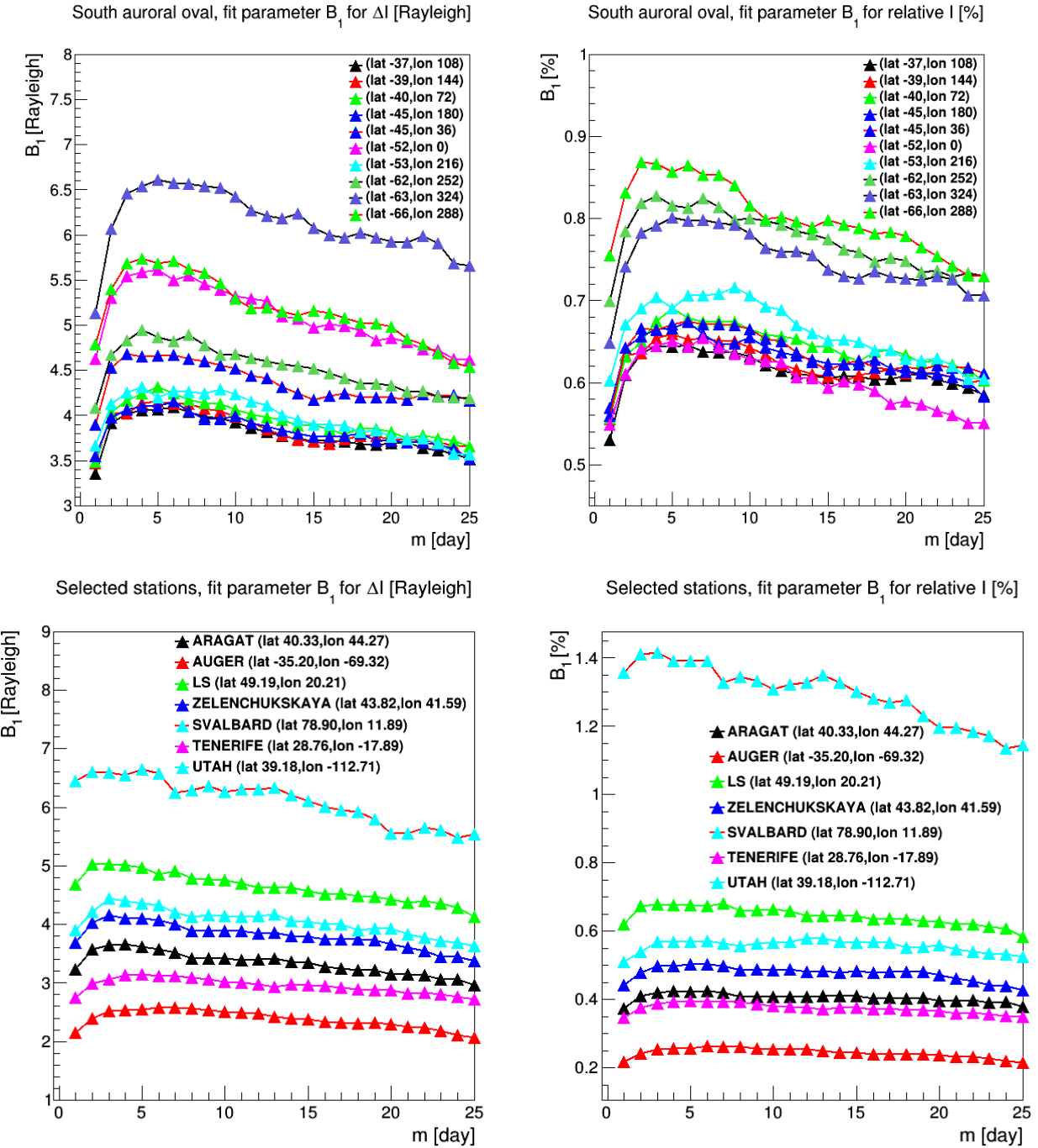


Figure 2.17: The fit slope  $B$  as function of preceding period length  $m$ . In the two upper panels for 10 positions at north at south auroral oval (positions for  $K_p=8$ ). At the bottom panel  $B(m)$  for seven selected geographical positions.

### 2.2.3. Slope method dependency on Solar cycle

We analyzed if lower statistic of measurements could influence sensitivity and how sensitivity in Slope method could change during the solar cycles. We checked  $B_1$  variation during period of more than three solar cycles between years 1970 - 2012. We evaluated slope  $B_1$  in 1st interval for 5 days long time window i.e.  $B_1(m=5)$  for each year from 42 years in tested period. The time evolution of  $B_1$  parameter was evaluated for Lomnicky stit and Tenerife positions. Results are shown in figure 2.18. together with the sunspot number (SSN, black circles) divided by one thousand, to be in scale with  $B_1$  values. As we can see in the figure for LS position slope  $B_1$  change between 0,4 and 1,2 (red line in figure). For Tenerife is  $B_1$  in range from 0,3 till 0,6 (green line). Clear pattern could be seen in  $B_1$  evolution at both stations. During the solar minima we see higher values of  $B_1$ . Vice versa during the solar maxima, smaller values of slope  $B_1$  are present. The Slope method (in context of  $B_1$  parameter) is more sensitive during less disturbed periods of solar cycle.

The reason to have Slope method more sensitive during the solar minima i.e. during less disturbed years is clarified by the next figure. In the figure 2.19 we show the  $B_1$  slope for Lomnicky stit position in 1st interval for years 1990 (year close to solar maximum) and 1995 (year close to solar minimum). We could notice that in the year 1995 we have less points in the 2nd interval. The points in year 1995 have much less double slope character. There are almost not visible two slopes, one in 1st interval, second in 2nd interval. The reason why during more active periods appear second slope region is overlap of geomagnetic storms and saturation of airglow production for high values of  $\Delta Dst$ . During years close to solar maximum, more often second storm appear sooner than previous storm recover to non disturbed magnetosphere. Thus, new storm start during not yet finished previous storm.  $\Delta Dst$  and  $\Delta I$  are then evaluated from averages in  $m$  night long time window which include lowered airglow production of the previous storm.

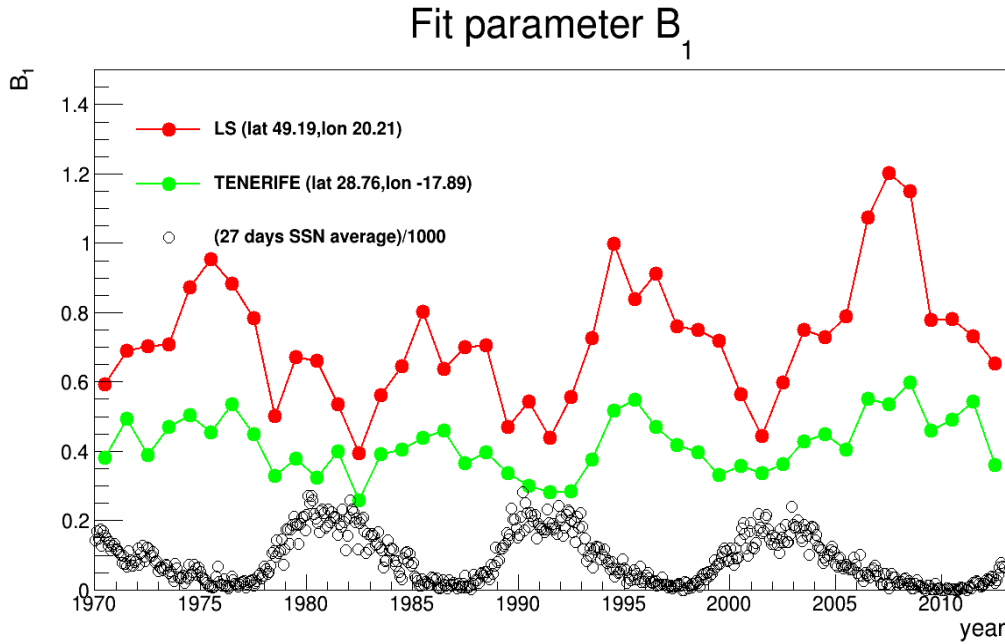


Figure 2.18:  $B_1(m=5)$  evolution during period of more than three solar cycles between years 1970 - 2012 for position Lomnicky stit (red) and Tenerife (green). Solar sunspot numbers (black circles) are presented in 27 days averages divided by one thousand.

LS (lat 49.19, lon 20.21), m=5

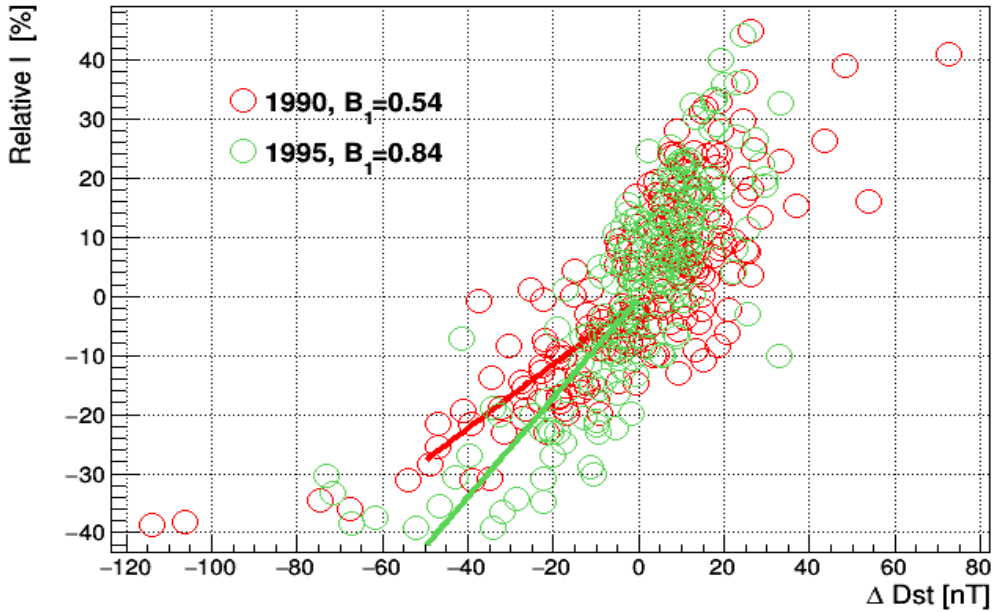


Figure 2.19:  $B_1$  slope for Lomnický štit position for years 1990 (red circles) and 1995 (green circles).

To learn how pattern of airglow production look during magnetic storms we find out some examples from produced AURIC simulations. In the figure 2.20 are couple of magnetic storms and following responses of ionosphere in airglow light production. First example for Utah position shows geomagnetic storms from November 1975. Moderate geomagnetic storm reaching  $Dst = -60$  nT lead to decrease of airglow production from  $\sim 850$  Rayleigh to slightly less than  $600$  Rayleigh i.e. decrease almost 30%. Another example from Zelenchukskaya position shows strong storm from December 1980 reaching  $Dst = -240$  nT with 30% decrease in airglow production. Example for Lomnický štit shows serie of small storm from January 1984 whose decrease airglow production about  $\sim 35\%$ .

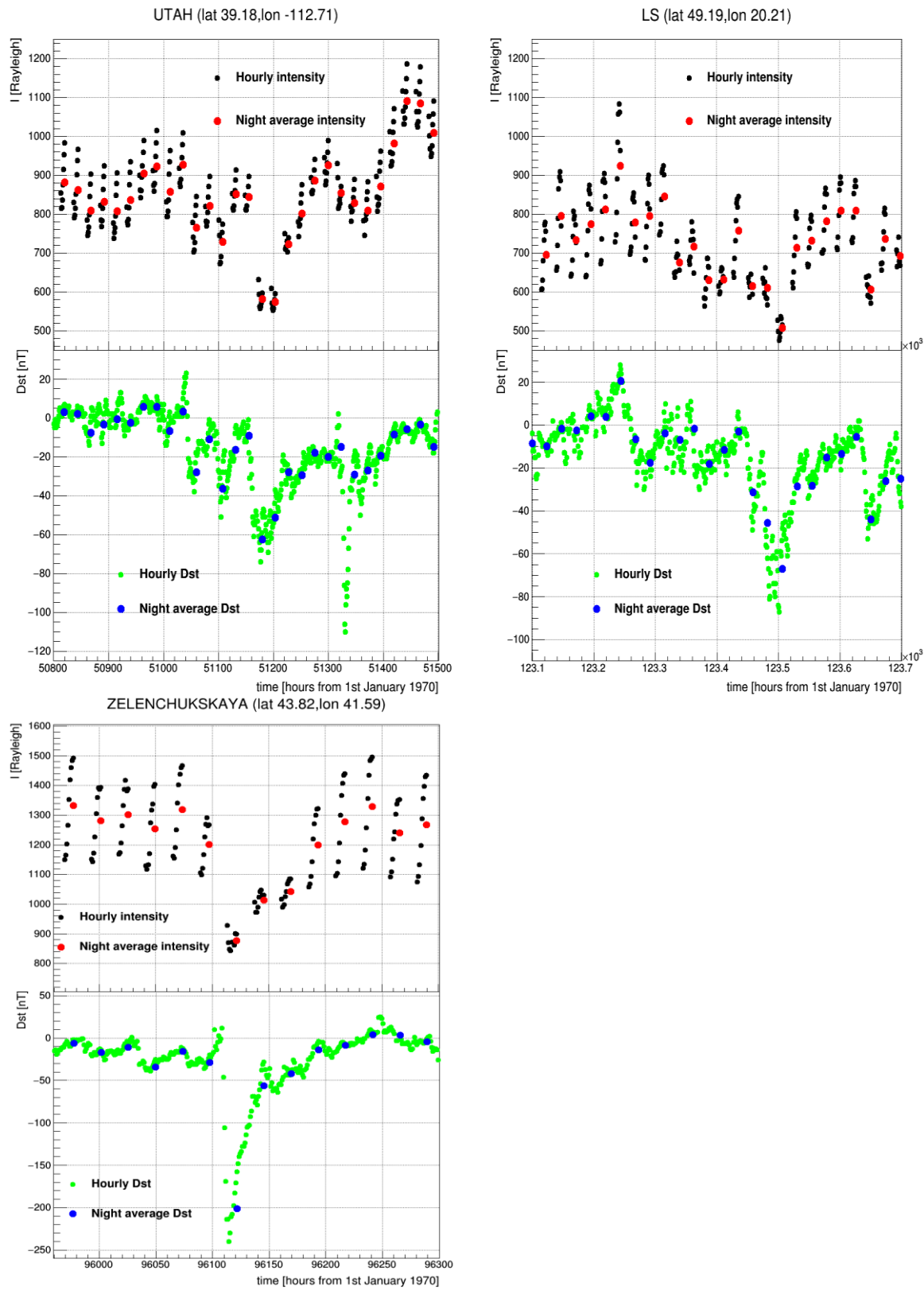


Figure 2.20: Airglow production evolution during selected geomagnetic storms at Utah, Lomnický Štit and Zelenchukskaya position.

### 3. Study of radiative transfer in Earth's atmosphere (WP3)

#### 3.1.1 Selection of radiative transfer tool

The fundamental equation, that describes the modification of radiation intensity during its traversal of a medium by counting up the gains and losses in this medium, is called the radiative transfer equation (RTE). It was introduced by Chandrasekhar (1960) in a basic form as

$$\frac{dI_\nu}{ds} = -\kappa_\nu \rho I_\nu + j_\nu \rho, \quad (3.1)$$

where the radiation intensity ( $I_\nu$ ) is defined as the amount of the radiant energy ( $dE_\nu$ ) in a specified frequency interval ( $\nu, \nu+dv$ ) transported across the element of an area ( $d\sigma$ ) in directions confined to an element of a solid angle ( $d\omega$ ) at an angle ( $\theta$ ) during the time ( $dt$ )

$$I_\nu = \frac{dE_\nu}{\cos\theta dv d\sigma d\omega dt}. \quad (3.2)$$

The  $I_\nu$  is weakened by an interaction of radiation with matter and after traversing a thickness ( $ds$ ) it becomes weaker by factor of  $dI_\nu = -\kappa_\nu \rho I_\nu$ , where  $\rho$  is the density of material and  $\kappa_\nu$  is a mass absorption coefficient for radiation of frequency  $\nu$ . On the other hand, the  $I_\nu$  is more intensive by contribution of a mass element that emits in the direction of radiation propagation and is characterized by a emission coefficient  $j_\nu$ .

In the calculation of radiative transfer from the top of the atmosphere (ToA) of the Earth to the ground surface, the emission term needs to be taken into account only for thermal wavelength region ( $\sim 3 - 100 \mu\text{m}$ ). The absorption term represents the true absorption, when the radiation is transformed into other form of energy, and the scattering, when the radiation is absorbed and re-emitted to other direction that was the original direction of the radiation propagation. By considering the absorption term only and scattering phase function ( $p(\Omega', \Omega)$ ) which quantifies the probability that radiation is scattered from direction  $\Omega' = (\Theta', \Phi')$  into direction of propagation  $\Omega = (\Theta, \Phi)$  (where  $\Theta$  and  $\Phi$  are polar and azimuth angle, respectively), the RTE can be expressed as:

$$\frac{dI_\nu}{ds} = -\kappa_\nu \rho I_\nu + \frac{1}{4\pi} \int_0^{4\pi} p(\Omega', \Omega) I_\nu(\Omega') d\Omega'. \quad (3.3)$$

Then the aim of RTE is calculation of radiance as a function of location and direction. For calculation of radiance anywhere in the atmosphere, the boundary conditions are needed. They are defined by the radiation entering the atmosphere from above and by the reflecting properties of the surface. The Eq. 3.3 is an integro-differential equation and it can't be solved analytically without simplifications. Therefore the numerical methods, such as discrete ordinate method or Monte Carlo method, are commonly used. The fastest solutions can be obtained for 1D plane-parallel models. They assumed that optical properties vary with height only and not in the horizontal directions.

The radiative transfer codes for solution of RTE in Earth's Atmosphere have been developed since the 1950s. The comprehensive overview of the most relevant models was elaborate within "Task 1" of ESTEC Contract No AO/1-5433/07/NL/HE - Towards a Generic Radiative Transfer Model for the Earth's Surface-Atmosphere System: ESAS-Light (<http://esaslight.libradtran.org/internal/Wiki>). These authors provided detailed analysis of the topic and developed a powerful, well applicable and well documented tool - libRadtran.

The libRadtran (<http://www.libradtran.org/>) is an open source software covered by the GNU General Public License. It has been developed by the team of Prof. Bernhard Mayer (Meteorological Institute Munich (MIM); Deutsches Zentrum für Luft- und Raumfahrt (DLR), Germany) and it was introduced by Mayer et al. (1997) and Mayer and Kylling (2005). The libRadtran was numerously verified by measurements (e.g. Hofzumahaus et al., 2007; Garcia et al., 2014) and also by comparison with other models (e.g. Cahalan et al., 2005). The libRadtran (or its predecessor uvspec) has been used in more than 350 peer-reviewed publications (<http://www.libradtran.org/doku.php?id=publications>). One of the unique feature is that libRadtran contains several different RTE solvers, including DISORT code (Stamnes et al., 1988) that is widely used also by other common tools (e.g. MODTRAN (Berk et al., 2005); SBDART (Ricchiazzi et al., 1998)). Even more libRadtran involve MYSTIC - Monte Carlo code (Mayer, 2009) that is able to operate in spherical geometry. MYSTIC is one of a few codes which were compared within I3RC (Intercomparison of 3D Radiative Codes) initiative and generally agreed within  $< 1\%$  with other fine selected models suitable for benchmarking (<https://i3rc.gsfc.nasa.gov>). The libRadtran utilizes input parameters from different credible databases. The molecular absorption data is based on HHigh-resolution TRANsmision molecular absorption database - HITRAN (<https://www.cfa.harvard.edu/HITRAN/>). The profiles of arbitrary aerosol types can be defined according OPAC database (Hess et al., 1998). The surface albedo data can be specified according ASTER (Advanced Spaceborne Thermal Emission Reflection Radiometer) Spectral Library (<http://speclib.jpl.nasa.gov/>). And finally libRadtran allow calculations in UV spectral band, which is not common for all other tools

([http://www.worldlibrary.org/articles/list\\_of\\_atmospheric\\_radiative\\_transfer\\_codes](http://www.worldlibrary.org/articles/list_of_atmospheric_radiative_transfer_codes)). All of mentioned properties make libRadtran a suitable tool for the calculation of radiative transfer of UV light from top of atmosphere (ToA) to the ground. This is a necessary task for feasibility study of ionospheric disturbances observation by one pixel detector.

For the purposes of overview, here is a brief discussion of some other available tools for calculation of radiative transfer in UV band. The coupled Ocean Atmosphere Radiative Transfer (COART) was introduced by Jin et al. (2006). It is accessible as online radiative transfer model for the coupled atmosphere-ocean system developed at NASA Langley Center

(<https://cloudsgate2.larc.nasa.gov/jin/coart.html>). It uses a modification of DISORT code and its outputs are in very good agreement with libRadtran tool. Other tools like Planetary Spectrum Generator (PSG, <http://ssed.gsfc.nasa.gov/psg>) or Spectral Calculator ([www.spectralcalc.com](http://www.spectralcalc.com), based on LinePAK algorithms (Gordley et al., 1994)) are also accessible through web interface. The main disadvantage of the online tools is that they can't be executed in the loop and so they are not so effective as off-line computer tools like libRadtran (see e.g. Fig. 3.14). The other tools that provide calculations in UV spectral band like XRTM (X Radiative Transfer Model, <http://reef.atmos.colostate.edu/~gregm/xrtm/>) or MOSART (Moderate Spectral Atmospheric Radiance and Transmittance, <http://www.cpi.com/projects/mosart.html>) have been not updated since 2012 so they are not so suitable as continuously updated tools like libRadtran. The line-by-line tool LBLRTM (Line-By-Line Radiative Transfer Model, <http://rtweb.aer.com/lblrmt.html>) is an accurate and well known model dedicated mainly for calculations with high spectral resolution. However a such resolution is not needed for our purposes. Finally, the characteristics of the SCIATRAN model (<http://www.iup.uni-bremen.de/sciatran/>) are very similar to these of libRadtran. Rozanov et al. (2005) presented that results of both models are typically in agreement within 0.2%.

### 3.1.2 Effect of atmospheric properties to the radiative transfer

To generate the following results, we have used the libRadtran tool according detailed User's Guide (<http://www.libradtran.org/doc/libRadtran.pdf>). The result of the calculations strongly depends on the used parameters. If it is not directly specified, the default values listed in Table 3.1 were used.

*Table 3.1: The default input parameters for libRadtran calculations.*

Parameter	Value	Description
<i>Input spectrum</i>		
source	solar kurudz_1.0nm.dat	The data file with 2 columns. 1: Wavelengths from 250 - 10 000 nm with step 1nm. 2: Solar irradiance for each wavelength at ToA in [mW / (m <sup>2</sup> nm)]. The original data Kurudz (1992). (See Fig. 3.1 and 3.2 for more details.)
	isotropic_source_toa	Specifies that isotropic illumination is used at top-boundary instead of beam source.
wavelength	250 - 500	The wavelength interval in [nm].
<i>Atmosphere properties</i>		
atmosphere_file	afglms.dat	Standard Midlatitude Summer atmosphere. The data file with 9 columns. 1: Altitude [km], 2: Pressure [hPa], 3: Temperature [K], 4: Air density [cm <sup>-3</sup> ], 5: O <sub>3</sub> density [cm <sup>-3</sup> ], 6: O <sub>2</sub> density [cm <sup>-3</sup> ], 7: Water vapour density [cm <sup>-3</sup> ], 8: CO <sub>2</sub> density [cm <sup>-3</sup> ], 9: NO <sub>2</sub> density [cm <sup>-3</sup> ]. (See Fig. 3.4, and 5 for more details.)
pressure	1013	The surface pressure in [hPa].
aerosol_default		Default aerosol according to Shettle (1989). (See Fig. 3.11 for more details.)
		The absorption and scattering (molecular (Rayleigh) and aerosol (Mie)) are activated by default. The clear sky without clouds is assumed by default.
<i>Surface</i>		
zout	0	Altitude of the ground above sea level in [km].
albedo	0.1	The Lambertian surface albedo defined by number between 0.0 and 1.0.
<i>Geometry and RTE solver</i>		
sza	0	The zenith angle of the source.
umu	-1	The cosine of the viewing zenith angle, starting with negative values (downwelling radiance, sensor looks upward).
phi = phi0	0	Sensor azimuth equals to source azimuth. The sensor looks into the direction of the source.
rte_solver	disort	The numerical discrete ordinate method for solving of RTE in scattering media (Stamnes et al., 1988).
<i>Output spectrum</i>		

lambda uu		The intensity (radiance) at user specified angles (umu, phi) for corresponding wavelength. The units are $\text{W m}^{-2} \text{sr}^{-1} \text{nm}^{-1}$ .
-----------	--	--

The example of output of libRadtran tool by using parameters listed in Tab 3.1. is presented in Fig. 3.1 and Fig. 3.2. The integral of output spectral intensity at altitude of 80 km, where influence of atmosphere is negligible to the radiative transfer is  $=1360 \text{ Wm}^{-2} \text{sr}^{-1}$  (for wavelength interval 250 - 5000 nm). The outcome spectrum calculated at the sea level after propagation of solar light through default atmosphere is featured by well known absorption lines (e.g. O<sub>3</sub> in UV band, H<sub>2</sub>O in IR band).

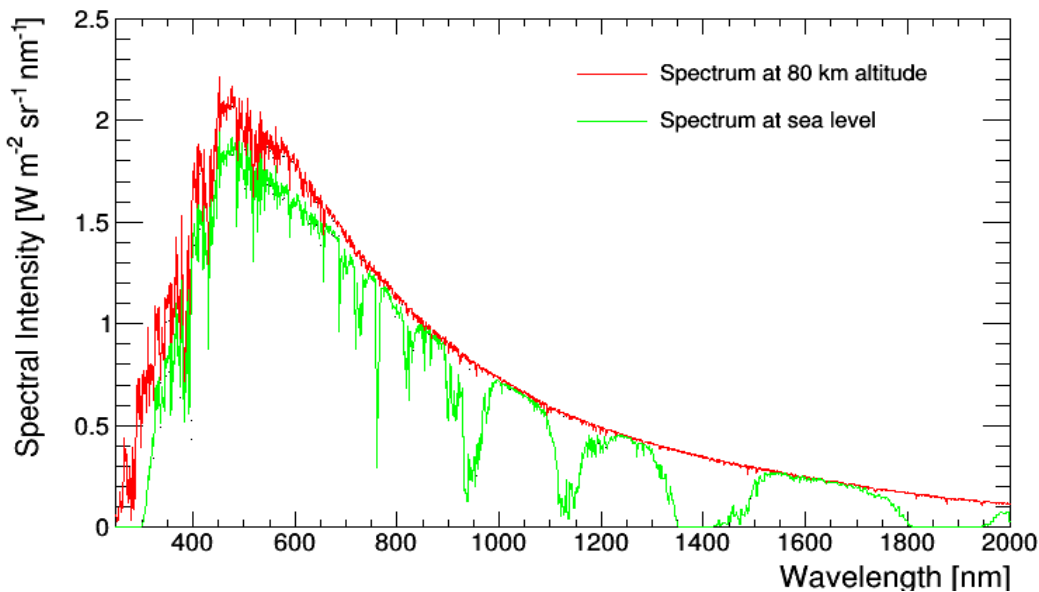


Figure 3.1: The spectral intensity at the altitude 80 km a.s.l. (red line) and on the ground at sea level (green line) for wavelength interval 250 - 2000 nm. The atmosphere parameters are specified in Tab. 3.1.

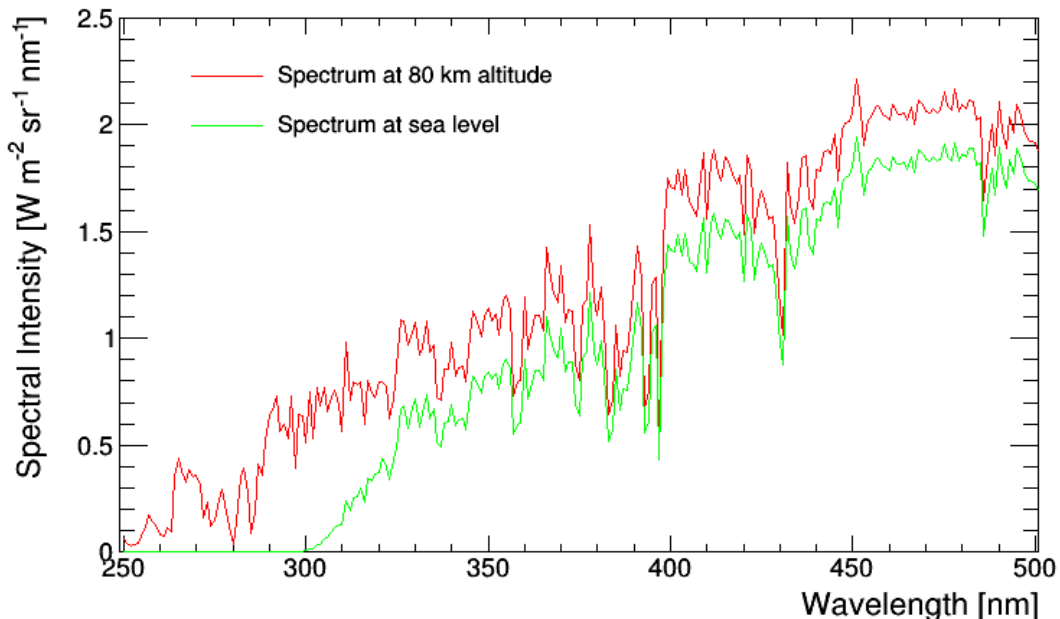


Figure 3.2: The same as Fig. 3.1 but for wavelength interval 250 - 500 nm. The integral of spectral intensity over this wavelength band is  $I_{@80} = 299.7 \text{ Wm}^{-2}\text{sr}^{-1}$  at altitude 80 km and

$$I_{@sl} = 229.5 \text{ Wm}^{-2}\text{sr}^{-1} \text{ on ground at sea level.}$$

The Earth's atmosphere used in the calculations is specified by the particular atmospheric parameters. Their values for Standard Midlatitude Summer atmosphere are displayed in Fig. 3.3 – 3.5.

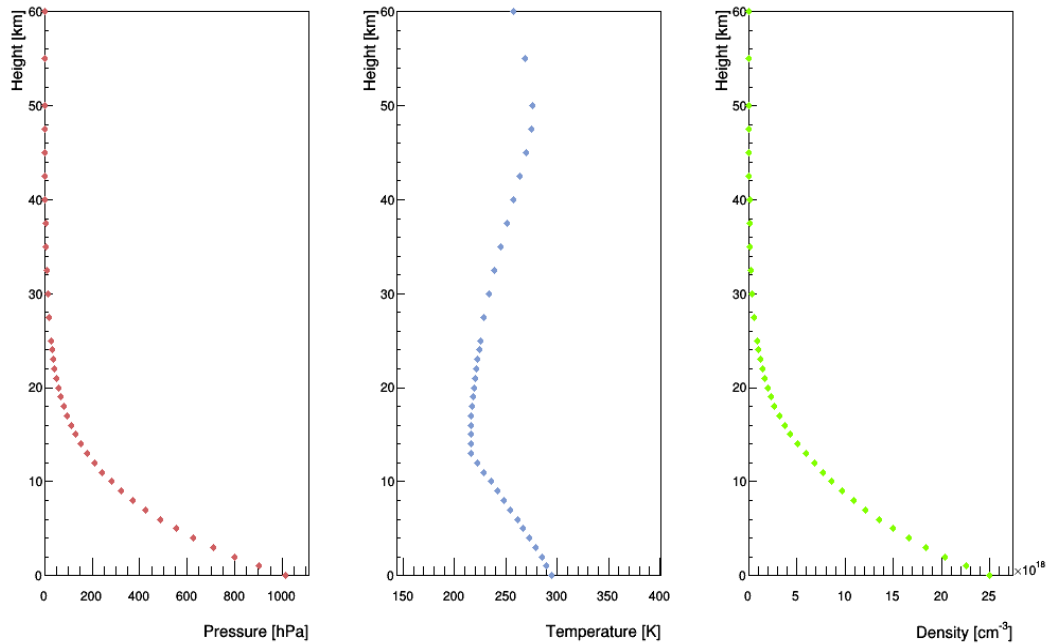


Figure 3.3: The atmospheric profiles of Pressure [hPa], Temperature [K] and Density [cm<sup>-3</sup>] as a functions of Altitude [km] for Standard Midlatitude Summer atmosphere.

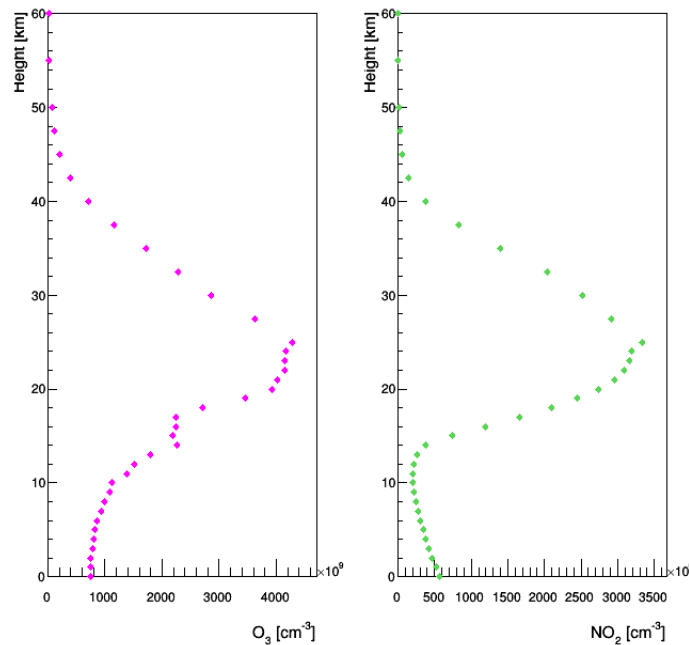
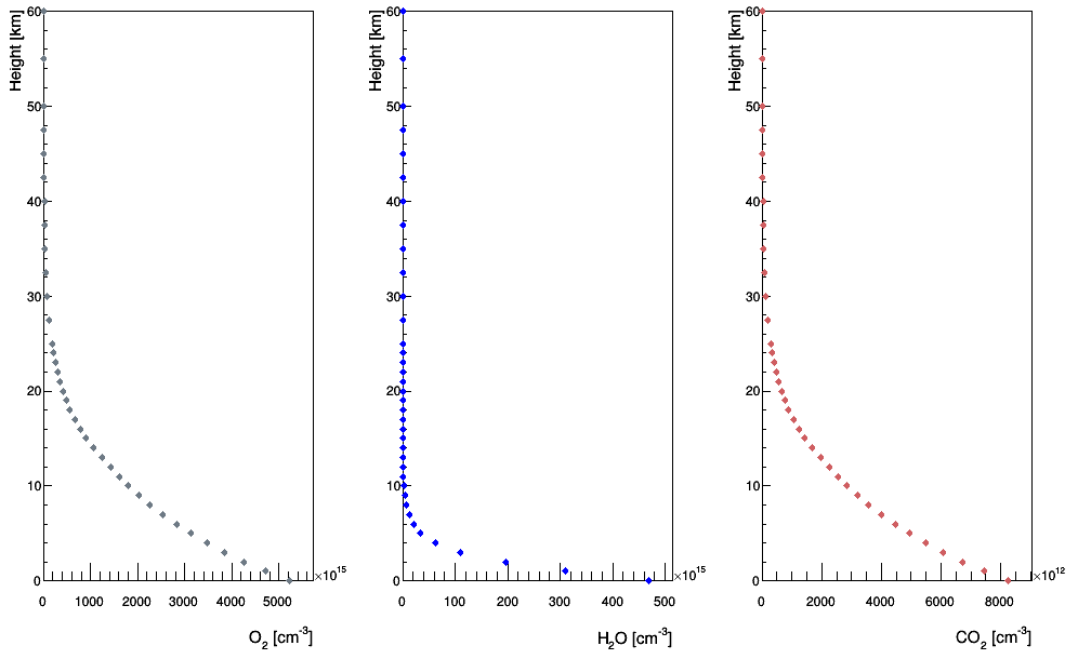


Figure 3.4: The atmospheric profiles of Ozone (O<sub>3</sub>) [cm<sup>-3</sup>] and NO<sub>2</sub> [cm<sup>-3</sup>] density as a functions of Altitude [km] for Standard Midlatitude Summer atmosphere.



*Figure 3.5: The atmospheric profiles of  $O_2$  [ $\text{cm}^{-3}$ ],  $H_2O$  [ $\text{cm}^{-3}$ ], and  $CO_2$  [ $\text{cm}^{-3}$ ] density as a functions of Altitude [km] for Standard Midlatitude Summer atmosphere.*

The main task of the presented part of WP3 is to analyze if the variations of atmospheric conditions might preclude the detection of ionospheric disturbances by observation of airglow intensity with one pixel UV detector. To explore the possible influence of different atmospheric conditions to outcome spectra we went through these parameters one by one. We varied these parameters in their possible ranges and created the “variation plots” presented in Fig. 3.6 – 3.18. At this point the shape of an input spectrum doesn’t play the role because we are now interested in the relative change of the intensity (radiance), only.

At first, we investigated a boundary case when the atmospheric absorption and scattering were not assumed. The calculated values are displayed in Fig. 3.6. The total intensity is an integral of a calculated spectrum over a range 250 - 500 nm and according values in Tab. 3.1. It is expressed in the relative units [ru] while the value for the first parameter is assumed as a reference. The total intensity on the ground by assuming no absorption and no scattering is  $\sim 30\%$  higher than the total intensity in a clear sky (cloudless) conditions with atmospheric absorption and scattering, according conditions listed in Tab. 3.1. Comparison of cases with and without scattering and absorption give us estimation of these effects on radiative transfer caused by standard atmosphere.

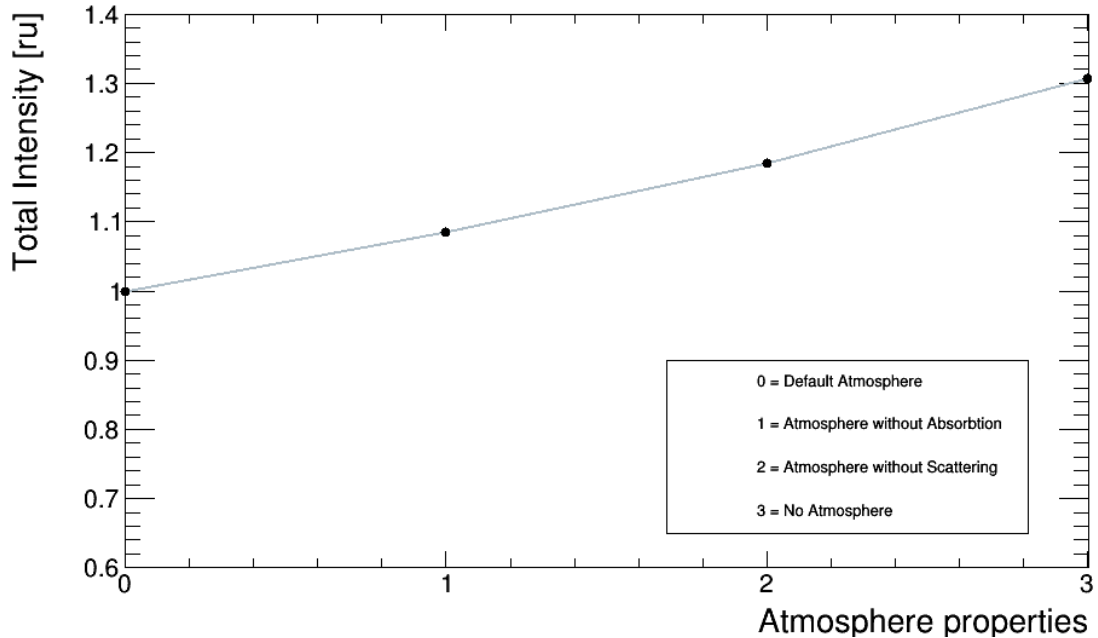


Figure 3.6: Variation plot - The total intensity in relative units [ru] calculated by radiative transfer through different atmosphere properties. The input parameters are as they are specified in Tab. 3.1.

The influence of modification of overall atmospheric properties (presented in Fig. 3.3 – 3.5) outlined in the standard atmospheres is presented in Fig. 3.7. The standard atmospheres are defined in Anderson et al. (1986). The influence of assumption of different standard atmosphere is less than 0.5%. This fluctuation seems to be negligible for the case of observation ionospheric disturbances by one pixel UV detector. The dependency of particular parameters from the standard atmosphere are presented in Fig. 3.13 – 3.17.

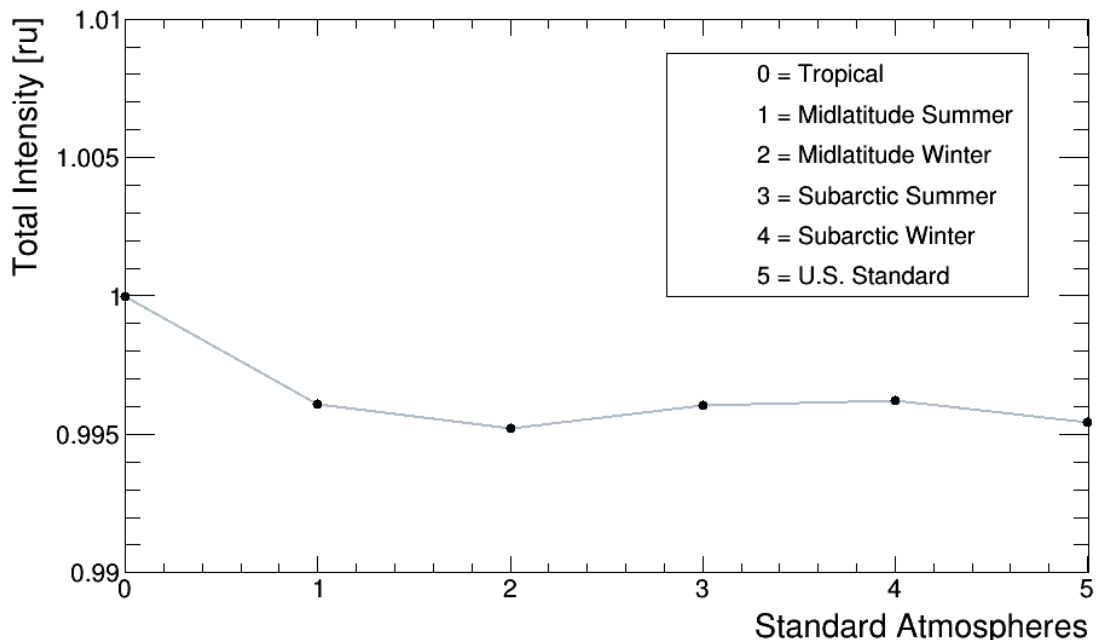


Figure 3.7: Variation plot for different standard atmospheres.

The eventual amount of radiation on the ground is increasing with the altitude above sea level. It is due to the atmosphere becomes thinner and atmospheric extinction, described by Beer-Lambert law, is lower. According calculations presented in Fig. 3.8 , the total intensity in altitude 10 km is higher by  $\sim 16\%$  than the total intensity at a sea level. This changing is quite significant and altitude need to be taken into account when the absolute values from two detectors on different places will be compared. However the altitude doesn't need to be considered for the measurements of relative changes of radiation by single detector.

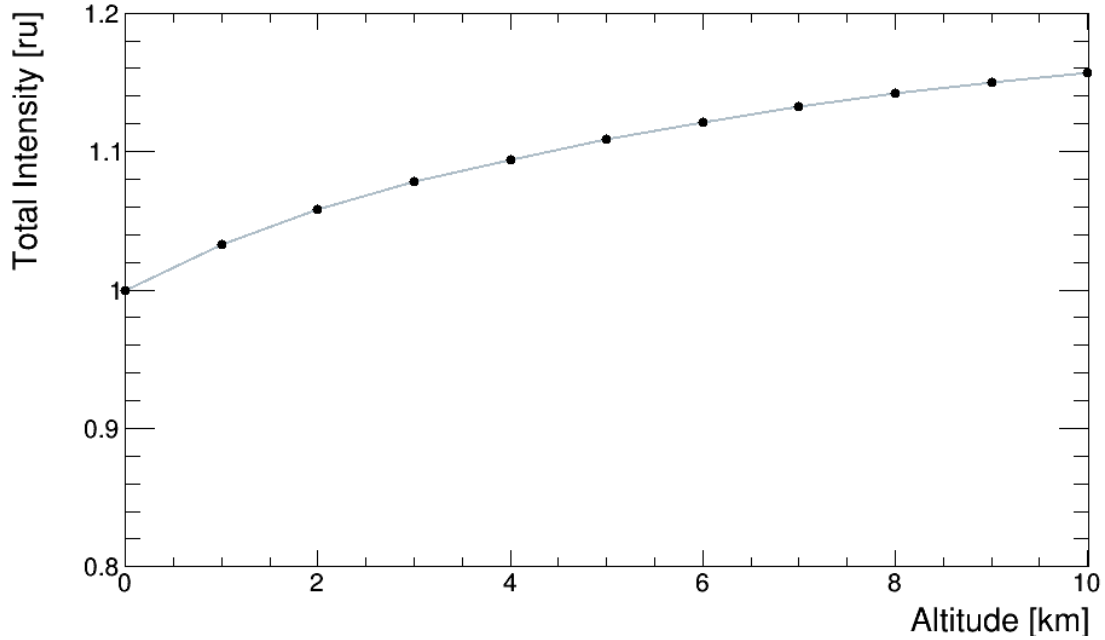


Figure 3.8: Variation plot for different surface altitudes [km].

The thickness of the atmosphere plays the role also in comparison of detected radiation by different orientation of the detector. The variation plot for different detector orientations is displayed in the Fig. 3.9. The orientation is defined by angle  $\theta$  while in case of  $\theta = 0^\circ$  detector is looking upward to the zenith. Note that this result is for plane-parallel geometry approximation. This approximation provides reasonable results until  $\theta \sim 60^\circ$  in comparison with spherical geometry for wavelengths from UV band. The orientation of the detector during particular measurements will be not changed. This effect need to be considered for comparison of absolute values from different detectors (if they looking to different directions).

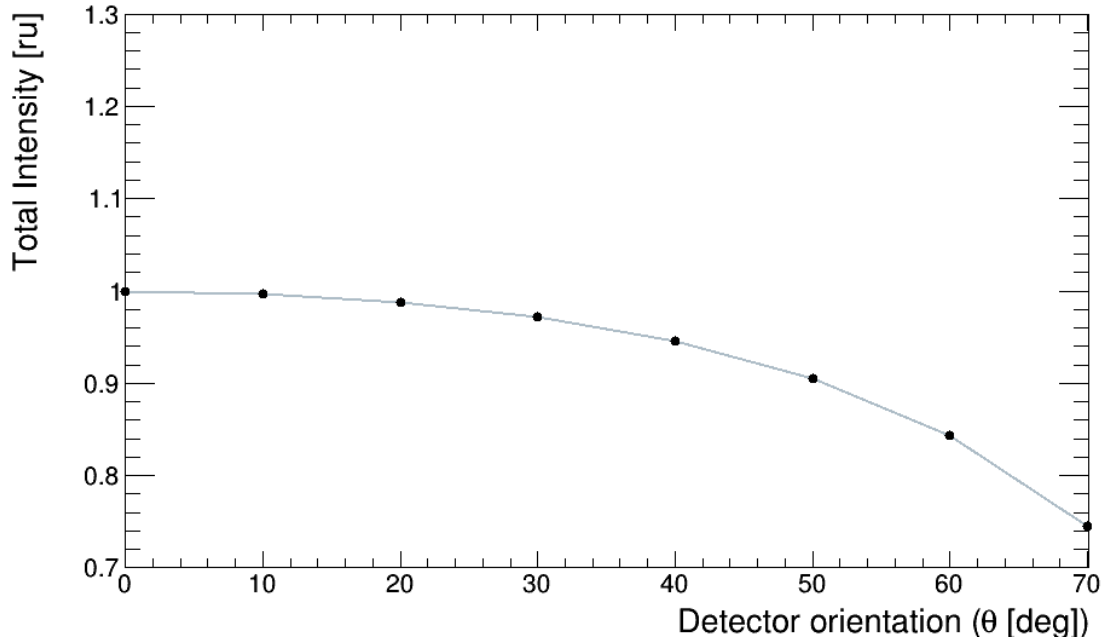


Figure 3.9: Variation plot for different angles  $\theta$  [deg] of detector orientation.

In this study, the isotropic layer source is considered. Therefore the zenith angles of the source have no influence on the measured radiance. The variation plot for different source zenith angles is displayed in Fig. 3.10. This fact demonstrates that libRadtran is a suitable tool for our analysis. We can use any input spectrum (solar spectrum in this case) and we can simulate the layer source as the airglow is. (In the Section 3.2.1 of the report, the particular airglow spectrum for the input is used).

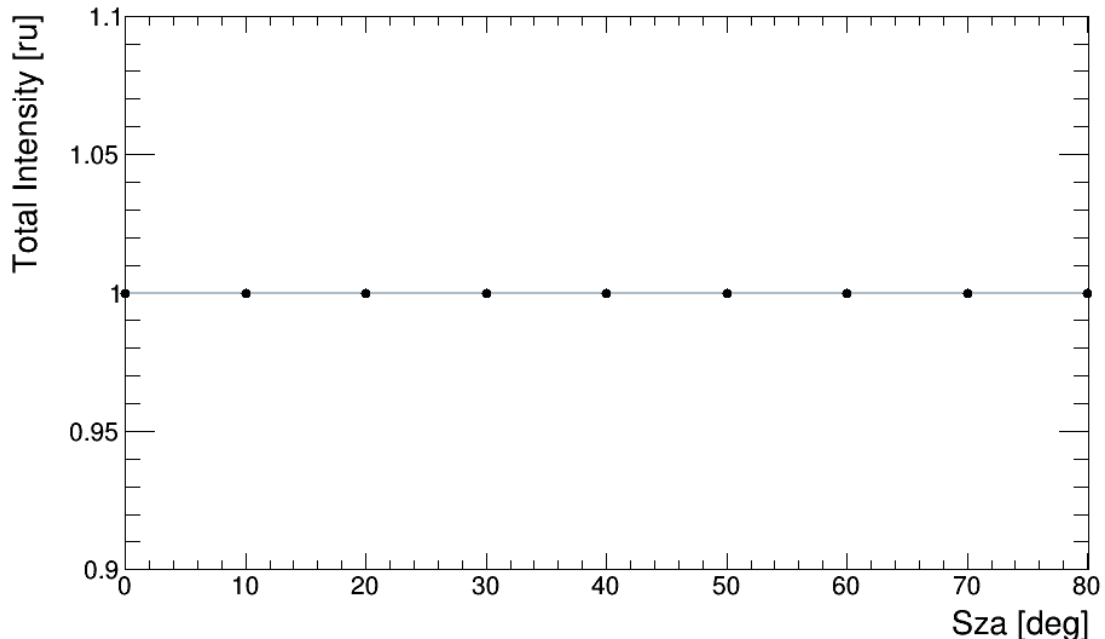


Figure 3.10: Variation plot for different input source zenith angles [deg].

The influence of Lambertian surface albedo is presented in Fig. 3.11. For the surfaces with the highest albedo such as snow (albedo  $\sim 80\%$ ) the total radiance should be up to 12% higher than the radiance measured on the surface with low albedo such as dark wet soil (albedo  $\sim 10\%$ ). In general the surface albedo for particular observation place should be constant. However the places with possible snow precipitation will need to be monitored due to possible change of the surface albedo. Also the spectral characteristic of the albedo will be taken into account for estimation of absolute values of UV radiation.

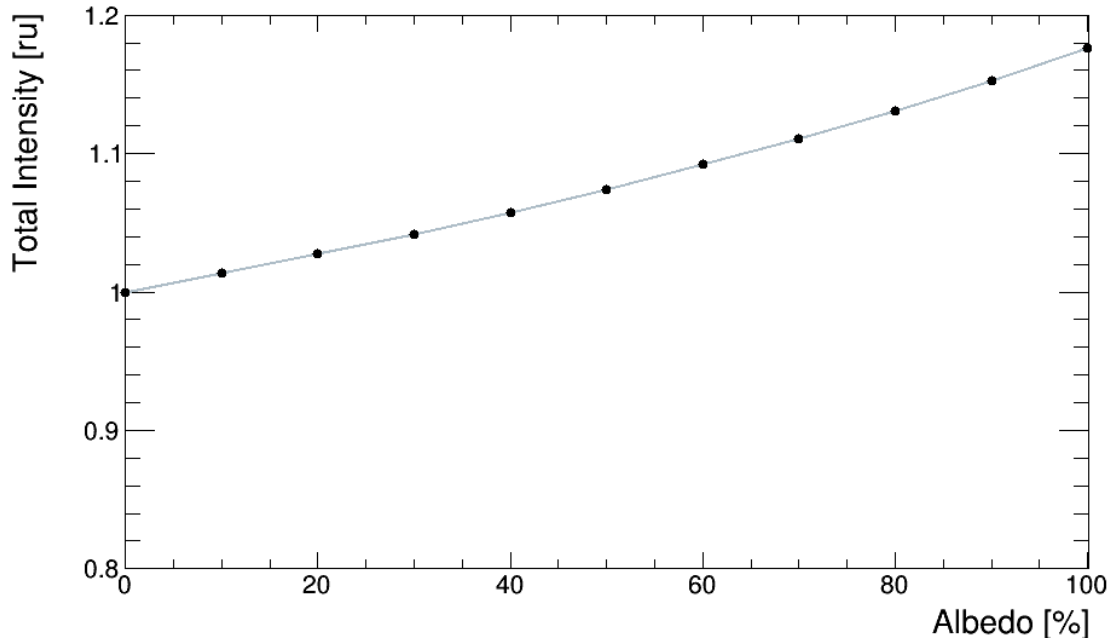


Figure 3.11: Variation plot for different Lambertian surface albedo.

The influence of aerosols - solid particles or liquid droplets in the air, is displayed in Fig. 3.12. We have calculated the total intensity for libRadtran preselected aerosol conditions. The default properties are a rural type aerosols in the spring-summer season and a visibility of 50 km (Shettle, 1989). The selected mixtures of aerosols are according definitions in Hess et al. (1998). The highest difference, up to 21% in comparison with default value, is by urban aerosol condition. But such significant change of aerosol conditions is not expected. The variation of aerosols is controlled by well distinguished regional rather than local sources of pollution (Gerasopoulos et al., 2011). Therefore they perform seasonal variations which can't preclude detection of ionospheric disturbances with duration several days. But in general to diagnose the presence of aerosols is not straightforward task and specialised equipment like LIDAR (Light Detection And Ranging) is required. Therefore aerosols could introduce not negligible uncertainty to the estimation of absolute intensity. One possibility how to overcome this difficulty is to locate our detector near to the detector for measurements of aerosols profile and to explore the aerosols influence to our measurements.

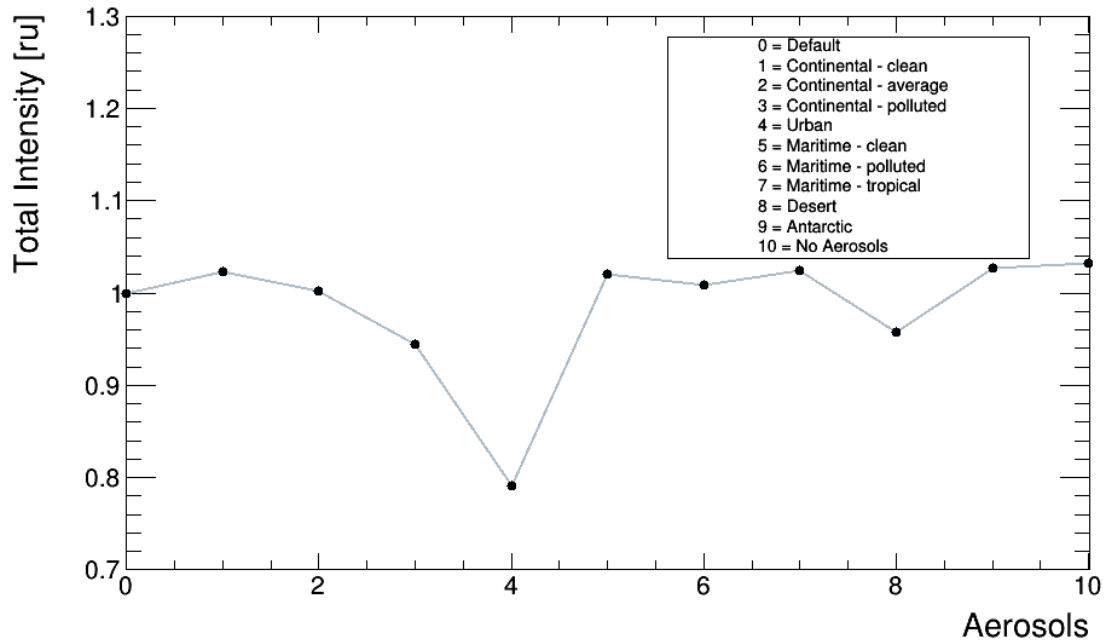


Figure 3.12: Variation plot for different aerosols conditions.

The variation of single parameters comprised in standard atmospheres (see Fig. 3.7) and their influence on the total intensity is presented in Fig. 3.13 – 3.17. The particular parameters with their units are specified in the caption of each figure. Each parameter is in its possible ranges detectable in the Earth’s atmosphere.

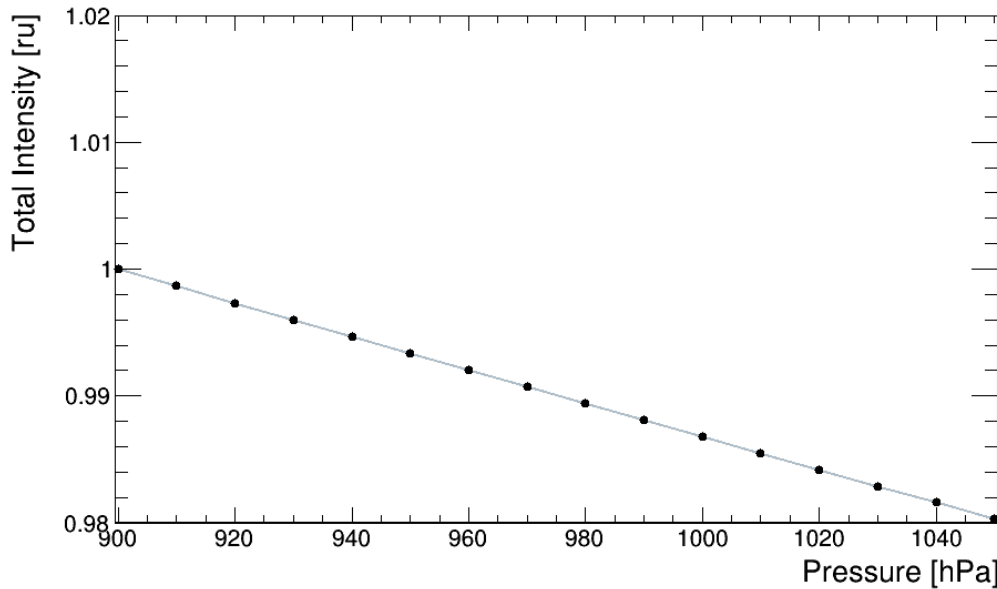


Figure 3.13: Variation plot for different atmospheric pressure [hPa] at surface . The pressure profile as well as air,  $O_2$  and  $CO_2$  profiles are scaled accordingly.

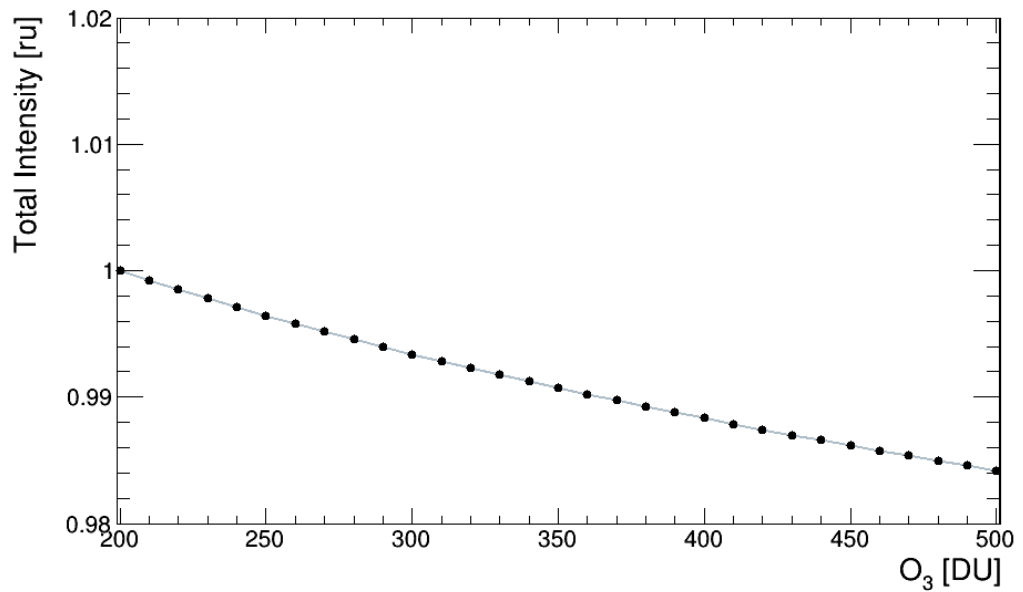


Figure 3.14: Variation plot for different ozone (O<sub>3</sub>) amounts in dobson units [DU].

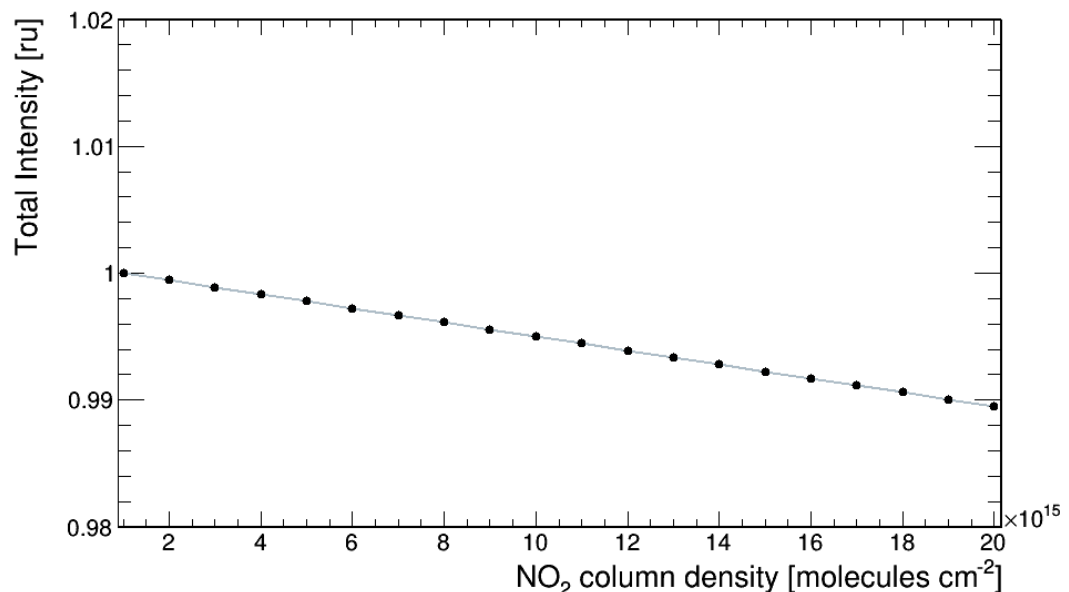


Figure 3.15: Variation plot for different nitrogen dioxide (NO<sub>2</sub>) column densities in molecules per square cm.

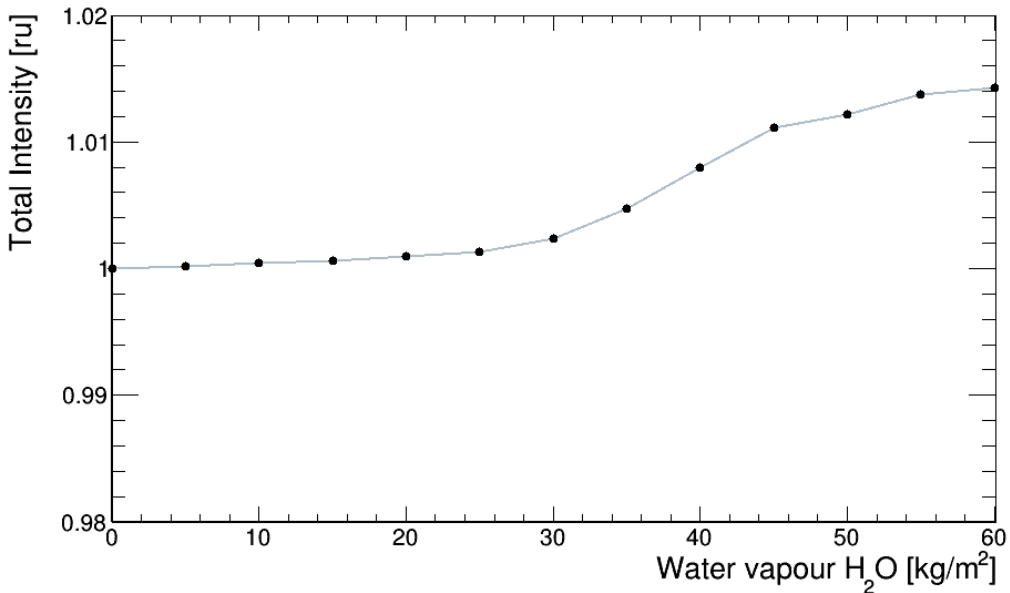


Figure 3.16: Variation plot for different water vapour ( $H_2O$ ) column densities in  $\text{kg}/\text{m}^2$ .

Variation of other gases (like  $O_2$ ,  $CO_2$ ,  $CO$ ,  $BrO$ ) have no influence to the total intensity in the investigated wavelength range 250 - 500 nm. For example see Fig. 3.17.

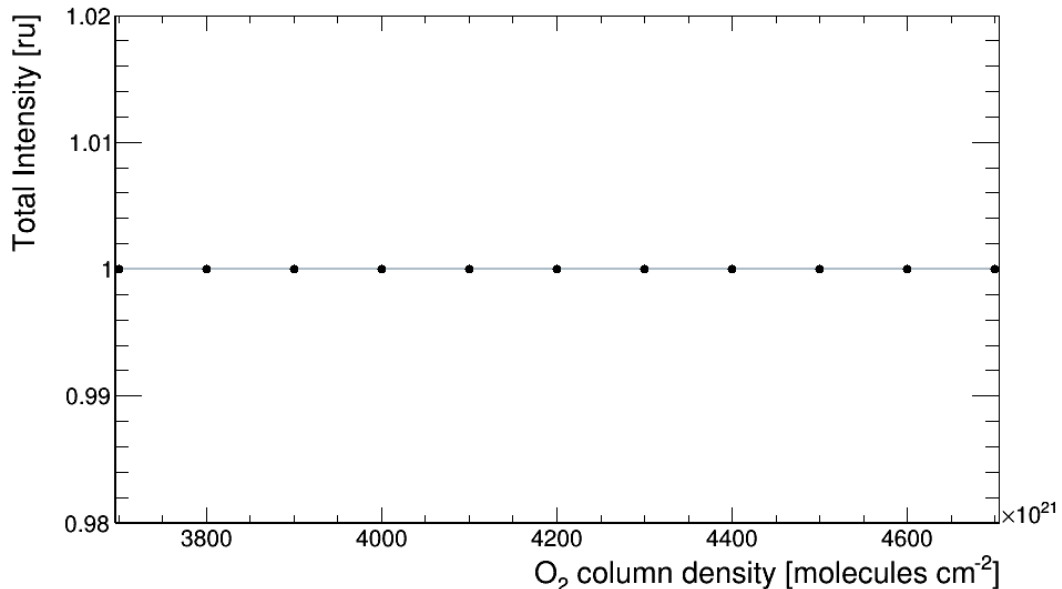


Figure 3.17: Variation plot for different molecular oxygen ( $O_2$ ) column densities in molecules per square cm.

Each changing of intensity caused by particular atmospheric variation acts as an uncertainty in estimation of absolute total intensity. It is a matter of difficulty to monitor the accurate value of each atmospheric parameter for each measurement. The total uncertainty ( $\delta I$ ) of the intensity measured during conditions listed in Tab. 3.1 is expressed as quadrature (square root of the sum of squares) of the particular maximal uncertainties ( $\delta I_1$ ,  $\delta I_2$ , ...  $\delta I_n$ ) that reflect variation of atmospheric properties presented in figures 3.13 - 3.17.

$$\delta I = \sqrt{\sum_{a=1}^n (\delta I_a)^2} = 2.2\%. \quad (3.4)$$

All of parameters mentioned above should not preclude the observation of ionospheric disturbances by UV detector. But this is not a case of a clouds influence. They are able to block up to 100% of UV radiation downwelling to the ground. The influence of different cloud types is displayed in the Fig. 3.18. The general cloud type characteristics (Hess et al., 1998, Rosenfeld and Lensky, 1998) used for calculations are listed in the Table 3.2.

*Table 3.2: The cloud types defined by liquid water content, effective droplet radius and altitude.  
Note (\*): In the case of cirrus, ice crystals are assumed.*

Cloud Type	Liquid Water Content: L [g/m <sup>3</sup> ]	Effective droplet radius: r <sub>eff</sub> [ $\mu\text{m}$ ]	Altitude: h [km]
Cirrus *	0.002	57	8 - 12
Fog	0.06	11	0 - 1
Stratus	0.28	7	1
Cumulus	0.3	4	1 - 2
Cumulonimbus	1 - 3	7-10	1 - 8

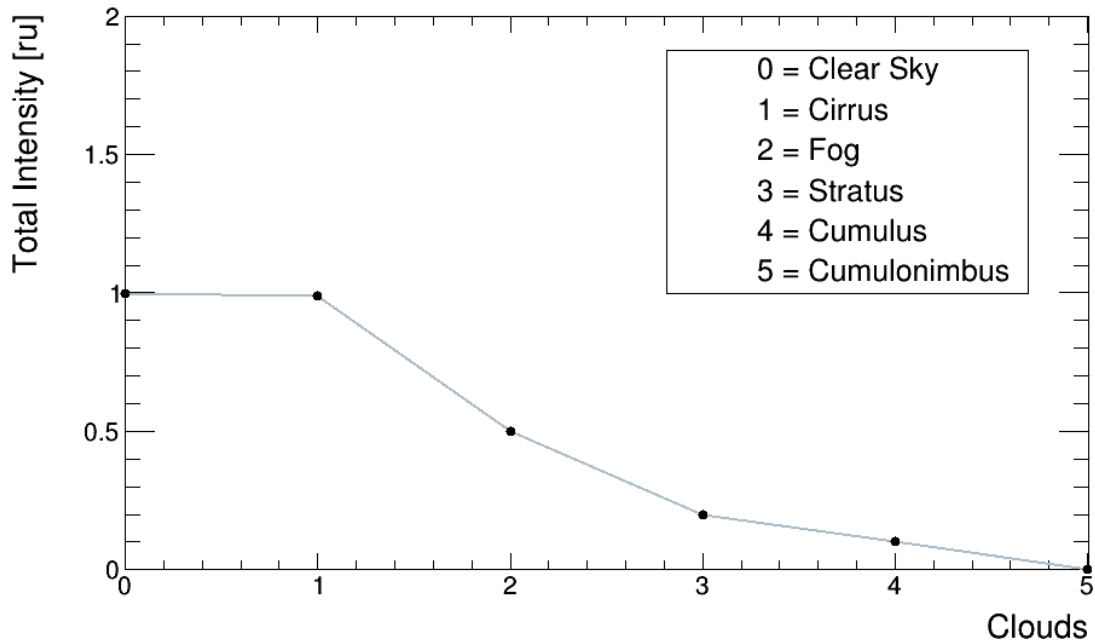


*Figure 3.18: Variation plot for different types of clouds.*

As it is seen in Fig. 3.18, the detection of the clouds is a mandatory task for measurements of one pixel UV detector. The measurements of ionospheric disturbances should be feasible only during cloudless conditions.

### 3.1.3 Estimation of clear sky probability

The clear sky probability of a particular observation site is an essential parameter for estimation of one pixel UV detector duty cycle. It is limited by cloud cover that block the downgoing airglow light and so preclude airglow measurements from the ground. For estimation of clear sky probability we have used statistical outputs from data of meteorological satellites.

The results are gained from the study of Wilson and Jetz (2016) that deal with 15-year MODIS (MODerate-resolution Imaging Spectroradiometer) archive of twice-daily observations from Terra and Aqua satellite during years 2000–2014. These observations were validated by cloud observations of a global network which consists of 5388 weather stations and is in operation since 1971. The used cloud detection algorithm provide a binary daily response (cloudy/ clear sky) with spatial resolution 1 km on the ground. The proportion of the cloudy days is expressed as mean annual value (%) over 15 years. The precision is described by spatial variability which represents the standard deviation (SD) of mean annual cloud frequency within a one geographical degree ( $\sim 110$  km) by circular moving window. This gives us an indication for conservative estimation of portion of clear sky probability per one year.

The potential observational sites of one pixel UV detector with indicated clear sky probability are listed in the Table 3.3 below. The observational sites are listed in order from the lowest mean annual cloud cover. The clear sky probability is expressed as the most conservative estimation by considering mean annual cloud cover and spatial variability. The clear sky probability means that at least this portion of days during one year should have clear sky conditions.

In the reality and for our purposes, the probability of clear sky conditions should be higher when we take into account the fact that for our valid measurements only few hours off cloudless night sky are satisfactory. The disturbances caused by geomagnetic storms take usually several days.

*Table 3.3: The potential observational sites of one pixel UV detector with clear sky probability.*

Observational site	State	Latitude [deg]	Longitude [deg]	Mean Annual cloud cover [%]	Spatial variability [%]	Clear sky probability [%]
Tenerife	Spain	28.76	-17.89	35.1	10	55
Telescope Array (BRM)	USA	39.19	-112.71	36.5	2	61
Pierre Auger Observatory	Argentina	-35.20	-69.32	36.7	2	61
Byurakan Observatory	Armenia	40.33	44.27	44.2	15	41
Zeppelin Observatory	Svalbard	78.91	11.89	44	4	52
Ratan (Zelenchukskaya)	Russia	43.82	41.59	60	8	32
Kolonica Observatory	Slovakia	48.93	22.27	67.6	5	28
Lomnický štít Observatory	Slovakia	49.19	20.21	85.5	4	10

The information of cloud coverage is required for each measurement of one pixel UV detector. For this purpose we plan to employ data from two sources. The first source is the weather simulated data of cloud coverage from

forecast model initially developed at the University of Basel, Switzerland (<https://www.meteoblue.com>) that are available for scientific usage (<https://content.meteoblue.com/en/content/view/full/4109>). They provide percentage of low, middle and high cloud coverage for any location on Earth with sufficient precision. The second source is the parallel measurements of the cloud coverage by simple infra-red detector of clouds. Both sources are explored and described in more details in the Section 4.

### 3.1.4 Influence of starlight and zodiacal light

The astronomical objects could affect the airglow measurements of one pixel UV detector. The starlight and zodiacal light are investigated in this section. The direct light of bright stars and other astronomical objects like planets could be easily recognized in the continuous observations during several nights. The bright star creates sudden peak in measurements while the star passing through the detector Field-of-View (FoV). Such peaks could be corrected by known position of bright stars. The correction of Milky Way presence in the FoV is not so straightforward but can be performed by enough number of measurements. Moreover the observational setup of detector orientation, pointed to the Celestial Pole, could eliminate the impact of astronomical background. In this polar setup, the detector stares to the constant astronomical background during the whole year.

Another task is to estimate the integrated starlight of faint stars and Milky Way that is scattered in Earth's atmosphere. The comprehensive study of integrated starlight was prepared by Leinert et al. (1998). These authors estimated the integrated starlight contribution to the sky brightness by using data of Pioneer 10 and 11 space-borne photometry. They also concluded that the integrated starlight is constant to the diffuse night sky brightness over large time scales. Bernstein et al. (2002) also presented that the shape of integrated starlight is very stable and strength of spectral features changes throughout the night by less than 1%.

The zodiacal light is a product of sunlight scattered on interplanetary dust in the ecliptic plane (zodiac). Its influence to the astronomical observations is described in previously mentioned works (Leinert et al., 1998; Bernstein et al., 2002; Noll et al., 2012). The intensity of zodiacal light underlie seasonal variation due to Earth's orbital movement around the Sun and different solar activity. This intensity variation is in the level of ~ 10% over a period of one year. Considering the duration of ionospheric disturbance (several days), the radiation of zodiacal light can be considered as constant contribution with respect to seasonal variation. It needs to be take into account for estimation of absolute values. Note that intensity of the zodiacal light decrease rapidly towards the opposite point of the Sun on the night Sky and to the ecliptic poles.

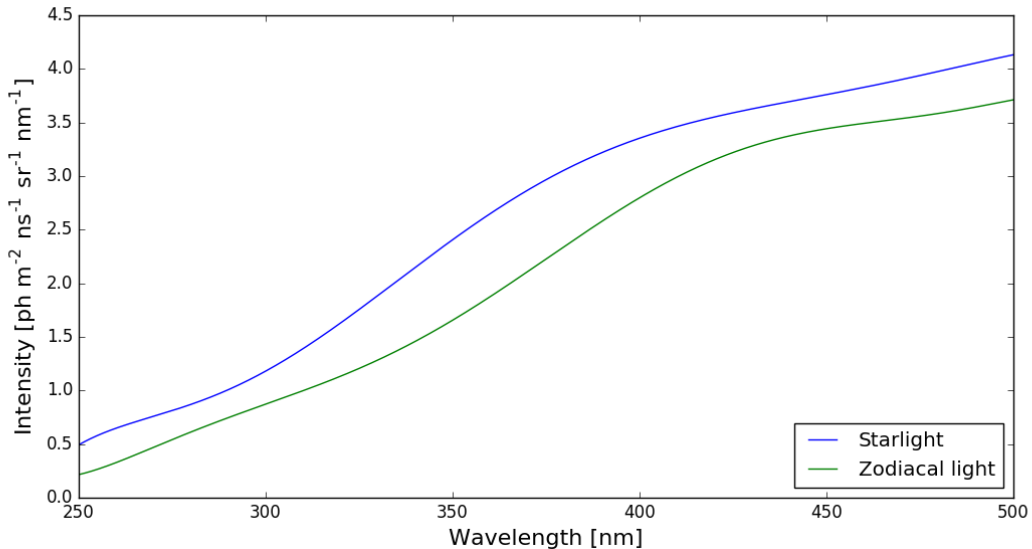


Figure 3.19: The starlight (blue) and zodiacal light (green) spectrum at the Top of Atmosphere.

The presence of starlight and zodiacal light need to be taken into account as contamination to the absolute value of airglow intensity. But they can be considered as constant for our purposes if looking to the celestial pole and can not preclude the observation of airglow variations caused by ionospheric disturbances. The spectra of starlight and zodiacal light that will be used in the following analysis (Sec. 3.2.1) have been obtained from Leinert et al. (1998) and they are displayed in Fig. 3.19.

Note that the light sources mentioned above (starlight and zodiacal light) are permanent and the airglow measurements can't be kept away from their influence. On the other hand, there are temporary light sources like sunlight, moonlight and man-made lights that can be excluded. Even more exclusion of temporary light sources is a mandatory task. The measurements are reasonable only during the dark night periods i.e. solar zenith angle  $S_{ZA} > 108^\circ$ , moon zenith angle  $M_{ZA} > 90^\circ$ , and the light pollution shall be inappreciable (within class 1 - 3 according Bortle Dark-Sky Scale). In our study we follow the rule that temporary light sources are completely excluded and the influence of permanent sources is implied.

### 3.1.5 Overview of successful detections of space weather impacts in airglow measurements by other authors

We have performed a study of the available scientific papers that were focused on the detection of space weather impacts by airglow measurements. This should indicate if our approach is useful also for the scientific community.

The connections between solar activity and intensity of airglow was first time reported by Rayleigh and Jones (1935) where the strong correlation between the airglow emission of green line at 557.7 nm with sunspot area was presented. Deutsch and Hernandez (2003) performed an extensive review of the airglow green line measurements. They put together measurements over 80 years from different observational sites and detectors. Besides different long-term and short-term variations of green line intensity related to the changes and circulations in the Earth's atmosphere they deduced that emission of green line seems to follow changes in solar activity expressed by solar flux  $F_{10.7}$  ( $f = 2800$  Mhz). The clear evidence of the green line intensity dependence on the solar cycle was provided by 15 years measurements (1995-2010)

reported by Reid (2014). If there are intensity variations of OI green line (557.7 nm), the variations in airglow UV band, that consists of O<sub>2</sub> emission lines (300-500 nm), are expected. This is based on co-variations of these spectral lines reported by e.g. Ogawa et al. (1987), Melo et al. (1996), and Slanger et al. (2004). Even more, Patat (2008) analyzed photometric data from ESO (European Southern Observatory) astronomical telescopes at Cerro Paranal obtained in the UBVRI passbands. He summarized that UBVRI night-sky brightness is well-correlated with the solar activity. The correlation is maximal in U passband (300 - 420 nm).

The occurrence of geomagnetic storms is a well known consequence of the solar activity (e.g. Gonzales et al., 1994). The influence of geomagnetic storms have been also observed in the airglow intensity measurements since the mid-twentieth century (Silverman et al., 1962, 1970). During the geomagnetic storm the density distribution of the charged and neutral species vary dramatically. A such variations have a clear signature in the volume emission rate and so the airglow emission would be a source of information about composition, dynamics and chemical state of the lower ionosphere (e.g. Bag et al., 2017). Several authors reported the direct measurements of such variations in airglow intensities during the geomagnetic storms. Leonovich et al. (2011) analyzed variation of well known atomic oxygen 557.7 nm and 630 nm lines by photometers. They detected the simultaneous variations in both wavelengths during the geomagnetic storm in midlatitudes. These authors also presented (Leonovich et al., 2012) correlation of airglow variations with the total electron content (TEC) disturbances. Similar results were presented by other group, Kelley et al. (2000) compared all-sky images of the 630 nm airglow emission and simultaneous observations using GPS satellite transmissions from a one night. They found that the dark portion of the image are regions of low TEC while bright regions have large values of TEC. Makela et al. (2014) reported an observation of geomagnetic storm by measurement of airglow emission in 630 nm with Fabry-Perot Interferometers.

Although all of previous mentioned works indicate that the detection of geomagnetic storms by airglow measurements should be possible it is still not well understand phenomena. Therefore the complex model (Sec. 3.2.1) of these processes followed by the appropriate measurements is crucial and useful also for the scientific community.

### 3.2.1 The airglow spectra time series for proposed observational sites

To simulate the intensities that are expected to be observed by one pixel UV detector, we have prepared the airglow spectra time series. We have used the airglow spectra calculated in Sec. 2 (from 1970 to 2012 with one hour time step) and the radiative transfer described in Sec. 3.1.1 and 3.1.2. All simulations were calculated for particular observational sites to take into account the airglow production location specifications, the constant starlight and zodiacal light spectrum (Sec. 3.1.4) and the atmosphere characterization for radiative transfer.

The atmosphere characteristics for particular observational site are listed in Table 3.4. The types of spectral albedo are used according definitions in Feister and Grewe (1995).

Table 3.4: The list of atmospheric characteristics for particular observational sites.

Observational site	State	Lat. [deg]	Long. [deg]	Alt. [m] asl	Type of atmosphere	Aerosols	Spectral Albedo
Byurakan Obs.	Armenia	40.33	44.27	1406	Midlatitude summer	Continental average	Loam
					Midlatitude winter	Continental average	Snow
Pierre Auger Obs.	Argentina	-35.20	-69.32	1413	Midlatitude summer	Desert	Sand
Lomnický štít Obs.	Slovakia	49.19	20.21	2634	Midlatitude summer	Continental average	Rock
					Midlatitude winter	Continental average	Snow
Ratan (Zelenchukskaya)	Russia	43.82	41.59	975	Midlatitude summer	Continental average	Grass
					Midlatitude winter	Continental average	Snow
Zeppelin Obs.	Svalbard	78.91	11.89	419	Subarctic winter	Antarctic	Snow
Tenerife	Spain	28.76	-17.89	2185	Tropical	Maritime tropical	Loam
Telescope Array (BRM)	USA	39.19	-112.71	1411	U.S. standard	Desert	Sand

The application of the atmospheric characteristics can be expressed by transmission function. To demonstrate its shape we assumed constant spectrum that is transmitting through the atmosphere (Fig. 3.20).

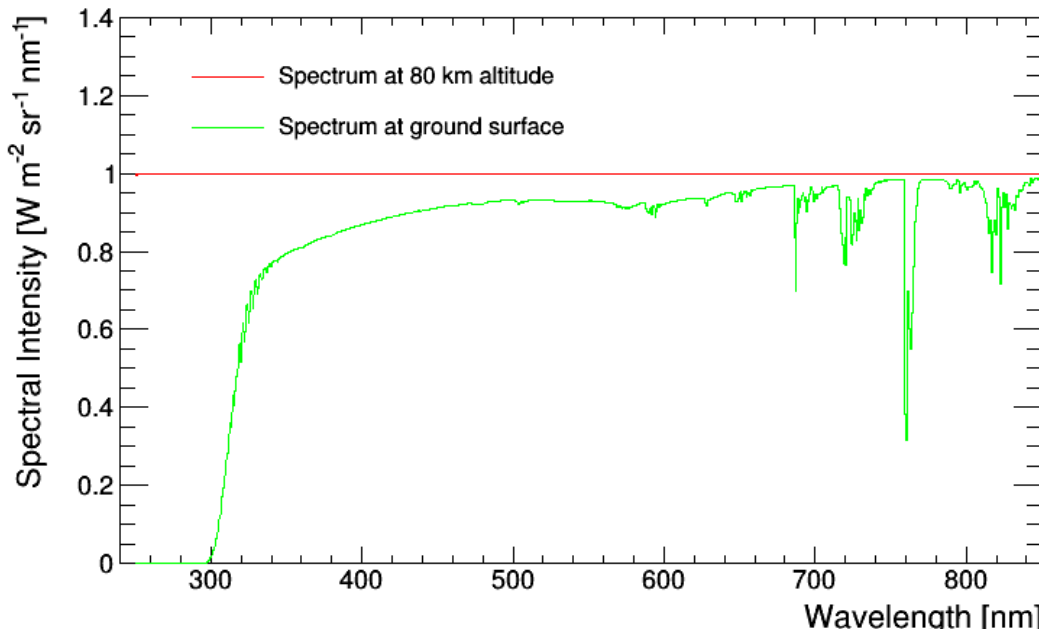


Figure 3.20: The example of the constant spectrum (240 - 850 nm) at altitude 80 km (red line) and on the ground surface (green line) - transmitting through the atmosphere characterized by the conditions specified in the Tab. 3.4, for Lomnický štít Observatory in the summer.

In the following, dependence of the light intensity (airglow light + star light + zodiacal light) time series on geomagnetic activity is described. The examples for Lomnický štit, Zelenchukskaya and Utah positions are presented in the Figure 3.21 - 3.23. These figures are based on the results presented in the Fig. 2.20 and on the results from Sections 3.1.1 – 3.1.4. It is clearly observable that radiative transfer through the Earth's atmosphere and presence of star and zodiacal light spectra don't hamper the observation of magnetospheric disturbances in these specific cases.

LS (lat 49.19, lon 20.21)

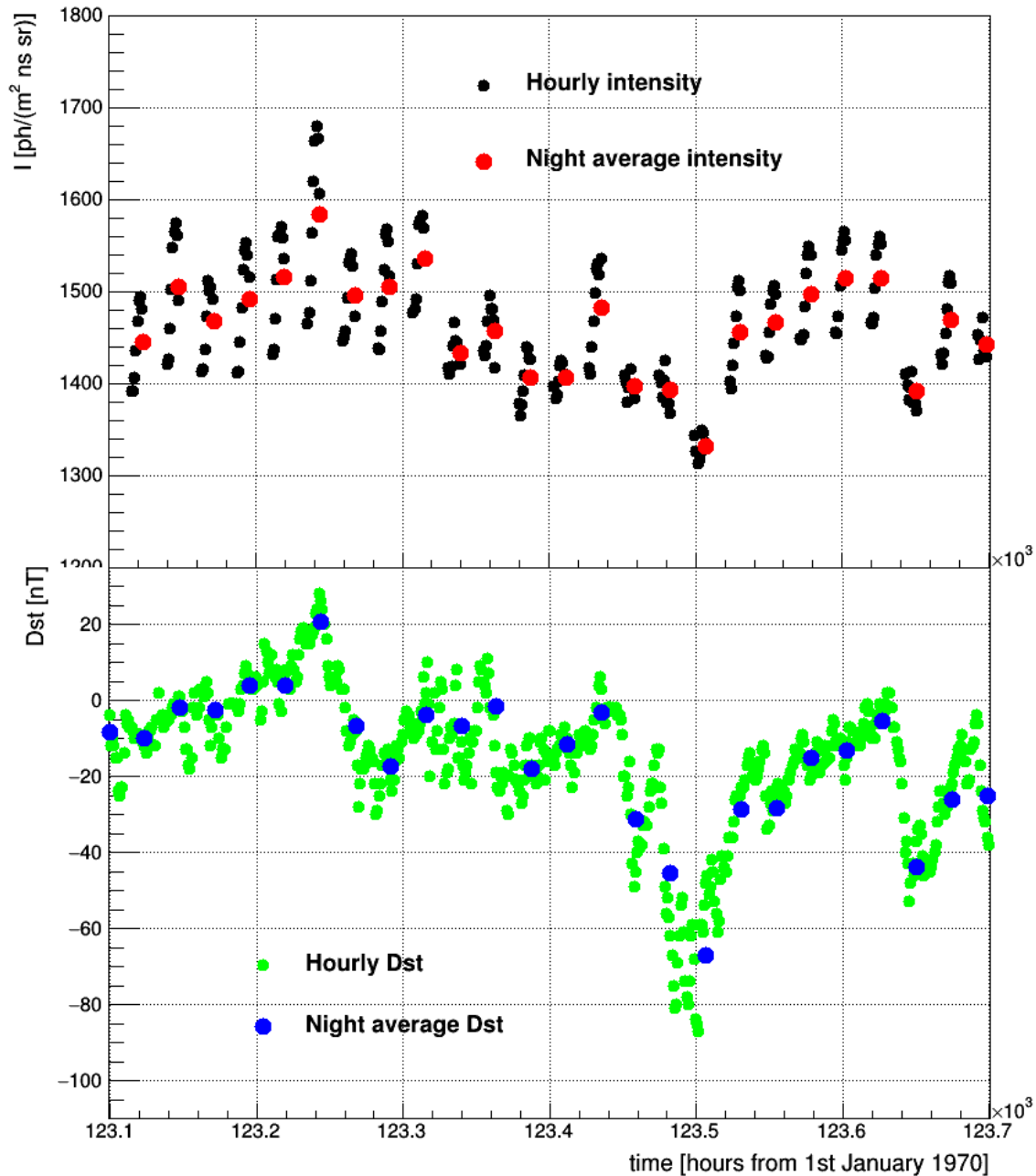


Figure 3.21: Time series of airglow production (top) and Dst index time evolution (bottom) for Lomnický štit position.

### ZELENCHUKSKAYA (lat 43.82,lon 41.59)

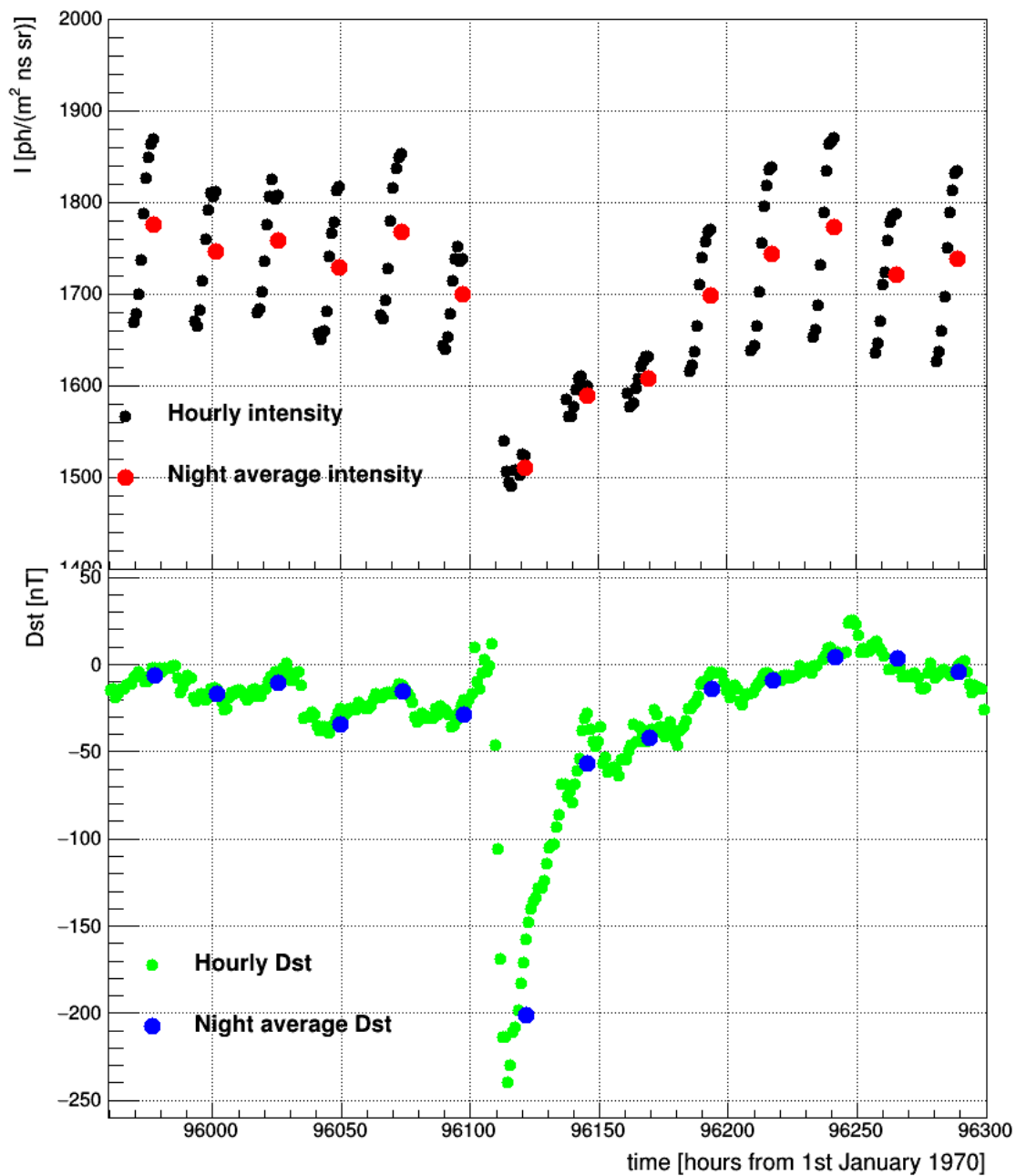


Figure 3.22: Time series of airglow production (top) and Dst index time evolution (bottom) for Zelenchukskaya position.

### UTAH (lat 39.18,lon -112.71)

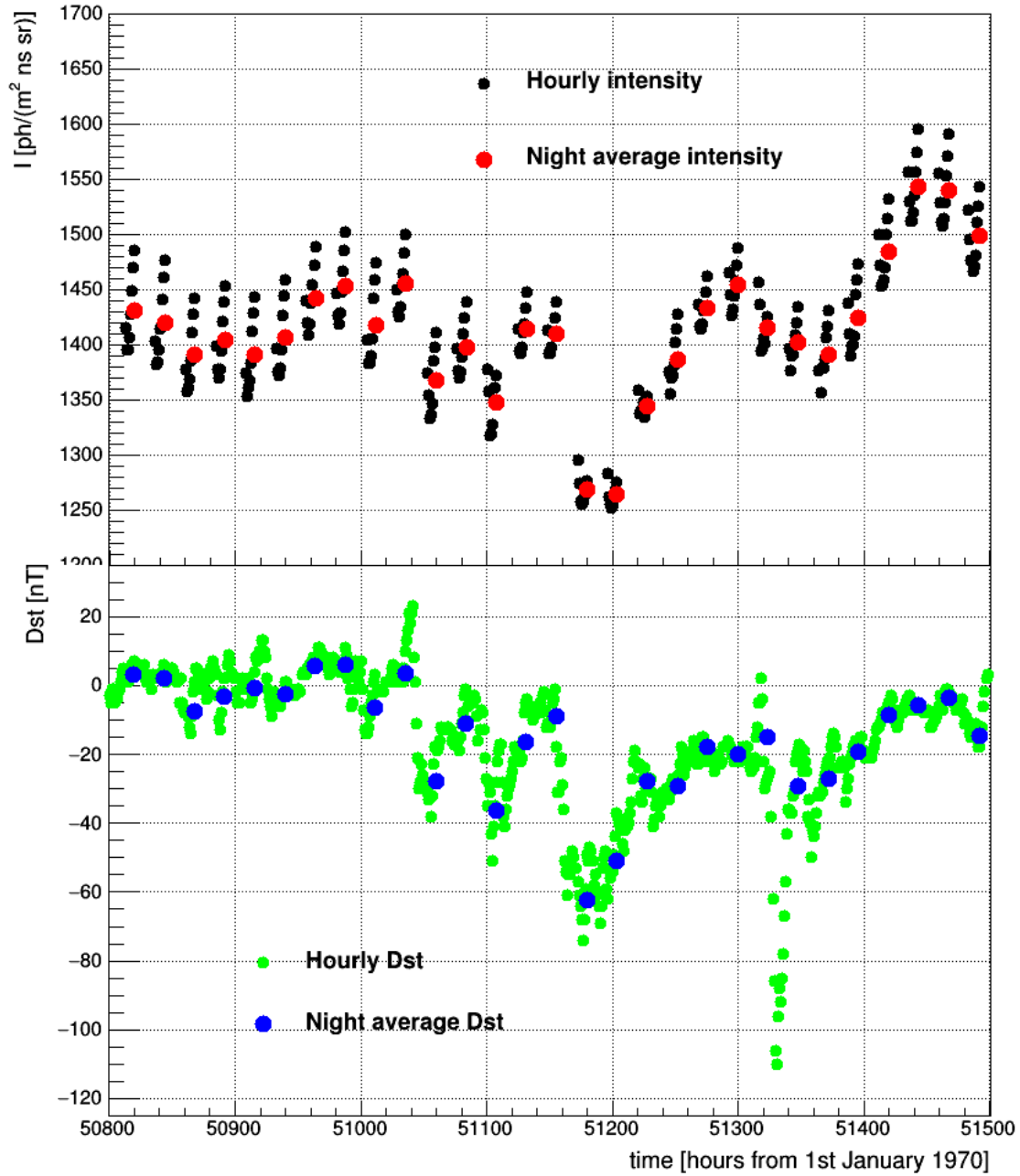


Figure 3.23: Time series of airglow production (top) and Dst index time evolution (bottom) for Utah position.

For more detailed statistical study of long time series of spectra we applied slope method for calculated radiations. Slope method was described in detail in the Section 2.2.1. Examples of correlations plot between absolute (left figure panel) and relative change (right figure panel) in overall intensity and absolute change in Dst index for Lomnický stit and Tenerife position are in figures 3.24 and 3.25. Preceding period length was five days in both cases. In both cases we can observe two areas ( $0, -50 \text{ nT}$ ) and ( $-50, -200 \text{ nT}$ ) with different slopes. Areas were fitted separately. We mainly focused on the area  $0, -50 \text{ nT}$  like it was explained in the Section 2.2.1. At Lomnický stit position we can expect 0.2% change in overall radiation for unit change in Dst index ( $B_1$  region). In case of Tenerife relative change is approximately two times lower 0.12% per nT.

We calculated dependence of  $B_1$  parameter on preceding period length for all selected positions. Results are in the Figure 3.26. For each position we can observe maximum in interval of preceding period length from 2 to 5 days. For longer periods intensity change have slightly decreasing tendency. Most sensitive station is Svalbard with  $\sim 0.3\%/\text{nT}$  intensity change for 5 days preceding length period. Than follow Lomnický stit  $\sim 0.2\%/\text{nT}$ , Utah  $\sim 0.17\%/\text{nT}$ , Zelenchukskaya  $\sim 0.16\%/\text{nT}$ , Aragat  $\sim 0.14\%/\text{nT}$ , Tenerife  $\sim 0.13\%/\text{nT}$ , and Auger  $\sim 0.09\%/\text{nT}$ .

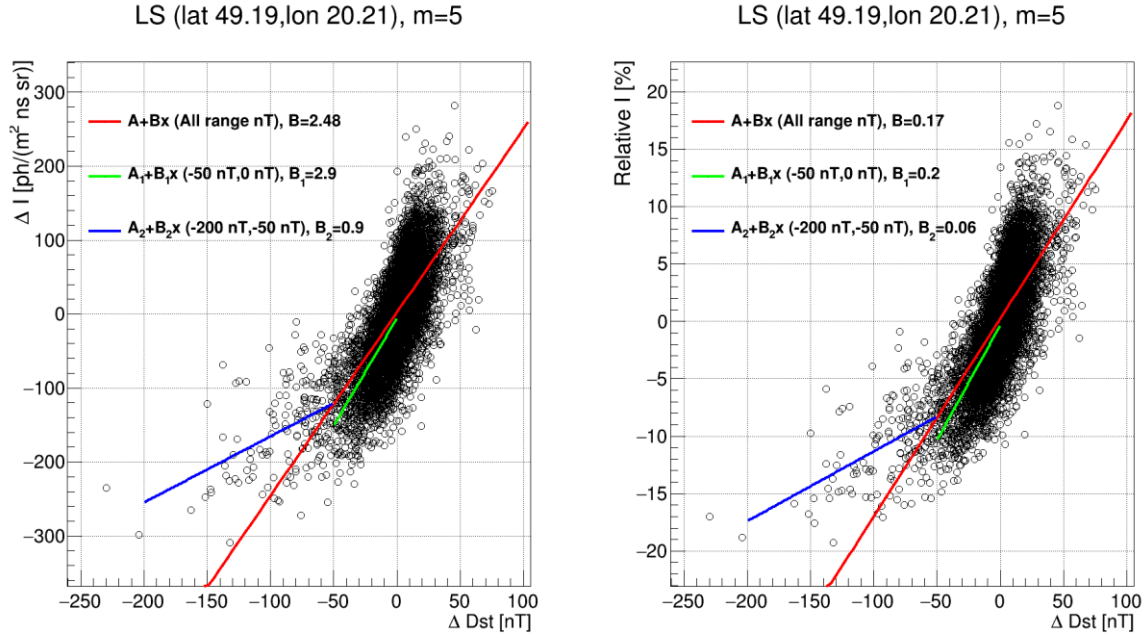


Figure 3.24: Absolute (left) and relative (right) intensity change in comparison with absolute change in  $Dst$  for Lomnický stit position.

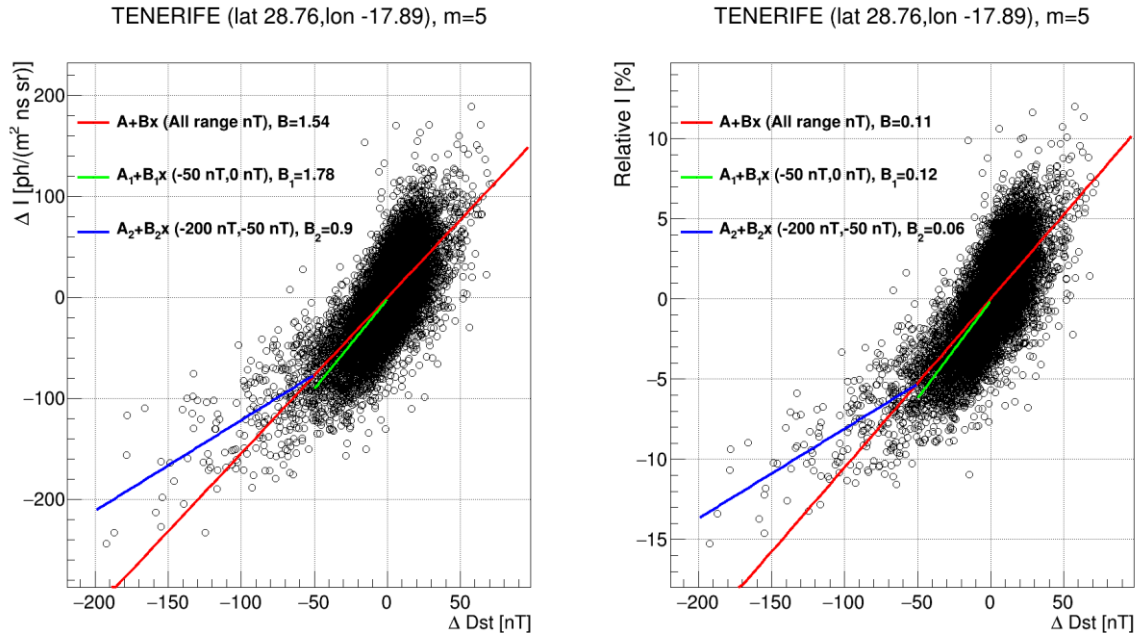


Figure 3.25: Absolute (left) and relative (right) intensity change in comparison with absolute change in  $Dst$  for Tenerife position.

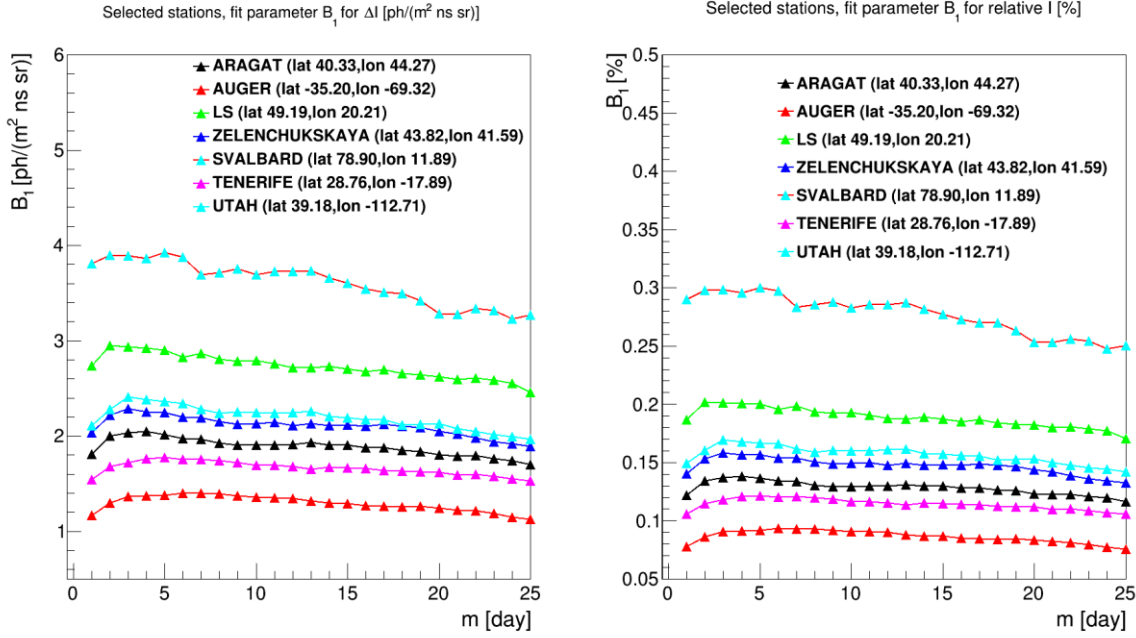


Figure 3.26:  $B_1$  parameter as a function of preceding period length  $m$ .

The found values of parameter  $B_1$  show that effect could be observable at ground in wavelength range from 300 to 500 nm. Observed light intensity will change during magnetic storms in range which one pixel UV detector could detect. For example at Lomnicky stit moderate storm when Dst change from 0 to -50 nT induce decrease in light intensity at the ground about 10% (green fit in figure 3.24. right panel). Strong storm when Dst reach value -100 nT mean decrease in light intensity by 12% (blue fit in figure 3.24. right panel). At Tenerife, the effect is smaller, 6% for -50nT strong storm, and around 8% for -100nT strong storm. Taking into account expected one pixel UV detector abilities, we conclude that magnetic storm could be observed at Lomnicky stit and maybe also on Tenerife. Better situation than on Tenerife will be on Utah, Zelenchukskaya and Aragat site. Worst situation will be at Auger site.

### 3.2.2 The Optimal wavelength range for geomagnetic storms detection

The next analysis was done to check optimal wavelength range for geomagnetic disturbances observation in airglow production. We assume detector observing in wavelength ranges wide 10 nm. We checked regions 250-260 nm, 260-270 nm ect. till region 890-900nm. For every region we realize same analysis as for full one pixel UV detector sensitivity range (300-500 nm). Taking in account airglow production, starlight and zodiacal spectra and radiative transfer we evaluate  $B_1$  parameter from signal time evolution at the ground.

The next figure (Fig. 3.27.) show a  $B_1$  values for 10 nm wide wavelength windows. The values of  $B_1$  parameters decreasing from 300-310 nm window till 490-500 nm region. The relative changes characterized by  $B_1$  parameter decreases with raise of wavelength. Increase in zodiacal and starlight radiation and diminish airglow towards 500 nm wavelength cause sloping dependence of  $B_1$  parameter. Let us note also that zodiacal light and starlight does not depend on geomagnetic disturbances.

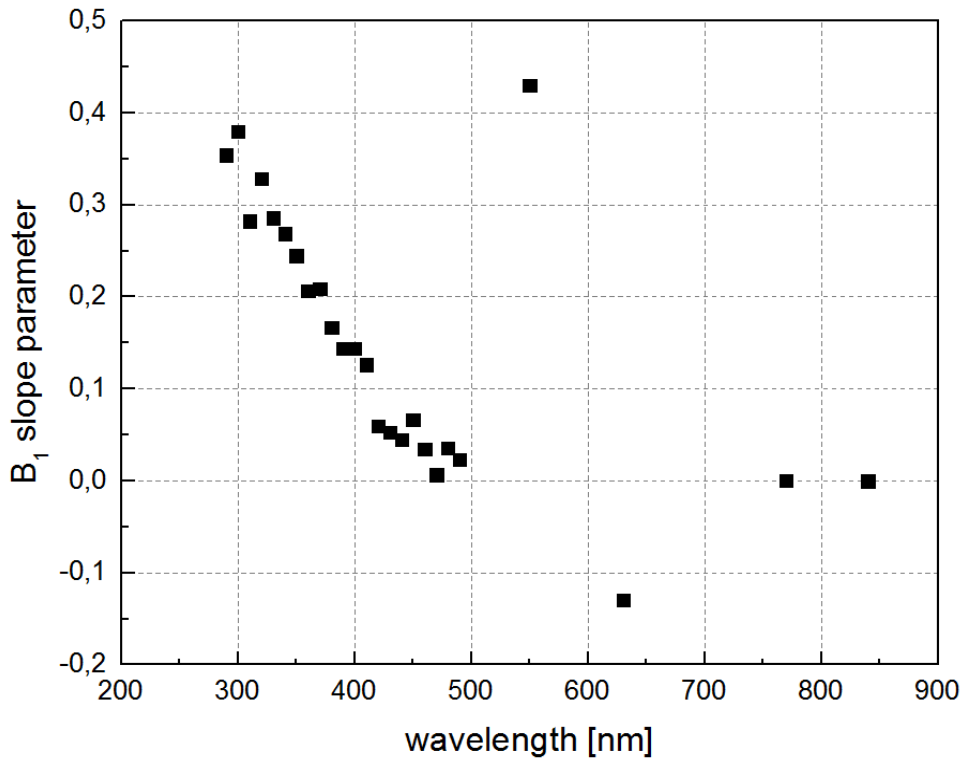


Figure 3.27:  $B_1$  parameter for 10 nm wide wavelength range windows at Lomnický stit.

If we evaluate average detector responses (multiplication of quantum efficiency and optical filter transmittance) in 10 nm wide wavelength ranges and include them to analysis to taking in account also detector response, then  $B_1$  parameter for relative changes of signal does not depend on detector response to observed light.

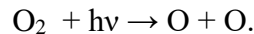
The region with emission line at 557 nm will be more sensitive to geomagnetic changes than regions between 300-500 nm if narrow filter will be used. With 10 nm optical filter is roughly two times more sensitive than one pixel UV detector measuring in full 300-500 nm range. However with filter which will change one pixel UV detector sensitivity to 300-400 nm range, we could measure with efficiency more similar to 557 nm. Reducing sensitivity of one pixel UV detector to 300-400 nm could be cheaply done by adding second layer of BG3 filter on detector. Sensitivity to geomagnetic storm then increases about 60% (increase from 10% to 16% for storm with  $Dst = -50$  nT), amount of detected light decreases about  $\frac{1}{3}$ . We will test such setup in the next months. With application of optical filters 10 nm wide to “positions” in 300-400 nm range we will face the low levels of observed intensities, order of magnitude closer to dark current of detector. But with wider collimator, this could be safe solution. Such change is still not major change in design of detector, but we will not classify it as small change.

We could conclude, that relative changes in observed light intensity are more easily detected in 300-400 nm region and at region including 557 nm emission line. Improvement at 557 nm line depend on width of observed wavelength region. More narrow wavelength region means better sensitivity due to suppression of Zodiacal light and star light components. With current one pixel UV detector design, some improvement could be reached by changing optical filters. However, even with current design detector is in theory still capable to observe geomagnetic disturbances.

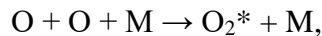
## 4. Data analysis review (WP4)

### 4.1.1 Description of the airglow monitor detector prototype

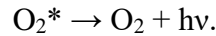
The one pixel UV detector for airglow monitoring (hereafter called AMON) is a prototype of an instrument that could observe the ionospheric disturbances by the measuring the airglow radiation. It is designed to measure the light in the range 300-500 nm which is generated in the Earth's upper atmosphere by the following process. The molecules of oxygen ( $O_2$ ) are dissociated by the solar UV radiation (with  $\lambda < 242.2$  nm) during the day,



During the night, the atoms of oxygen (O) are recombined to  $O_2^*$  excited molecules



where M represents another atom (oxygen or nitrogen) that is needed for the reaction. The molecules in metastable state have a short lifetime. Therefore the previous reaction is followed by the emission of photon



According electronic transitions responsible for UV emission the band systems are defined. The most intensive band systems are Herzberg I, Herzberg II, Herzberg III, and Chamberlain system with the maximum of production at altitude  $\sim 90 - 100$  km a.s.l.

To detect this faint UV airglow light, the very sensitive photomultiplier (PMT) is employed in the AMON detector. The Hamamatsu  $\mu$ PMT H124-00-01

(<http://www.hamamatsu.com.cn/UserFiles/DownFile/Product/20130813100246944.pdf>) is a convenient sensor for this task as it is tiny and high-sensitive. Before the light reaches the photosensor, it is filtered by Thorlabs BG3 bandpass filter (<https://www.thorlabs.de/drawings/3496ffa5bd62b30a-9C079BED-D035-CBDE-4B52634219083D7F/FGB25S-AutoCADPDF.pdf>) and collimated by narrow collimator with geometrical factor  $3.45 \cdot 10^{-6} \text{ cm}^2 \text{ sr}$ . Due to spectral characteristics of  $\mu$ PMT from and BG3 filter, approx. 70% of observed airglow light is in the 300-400 nm wavelength range. The photons are acquired during the 1s period and subsequently converted to ADC counts. The AMON is waterproof with weight 575 grams and dimensions 110 x 75 x 57 mm (Figure 4.1). The complementary sensors in detector are thermometer, barometer, luxmeter and GPS sensor. They provide information important for AMON safe operation. The data transfer as well as the operating commands are transferred via standard internet connection.

The AMON is continuously in a development process within the separated activity of the presented project. Its complex specification, further calibration, testing, improvement and modification based on operation experiences from first prototypes of four AMON detectors will be performed within the future PECS project "Follow-up of feasibility study to observe ionospheric disturbances by airglow monitoring network (AMON-net)" that was proposed by our Department of Space Physics (DSP, IEP, SAS) for 2<sup>ND</sup> CALL FOR OUTLINE PROPOSALS UNDER THE PLAN FOR EUROPEAN COOPERATING STATES (PECS) IN SLOVAKIA.

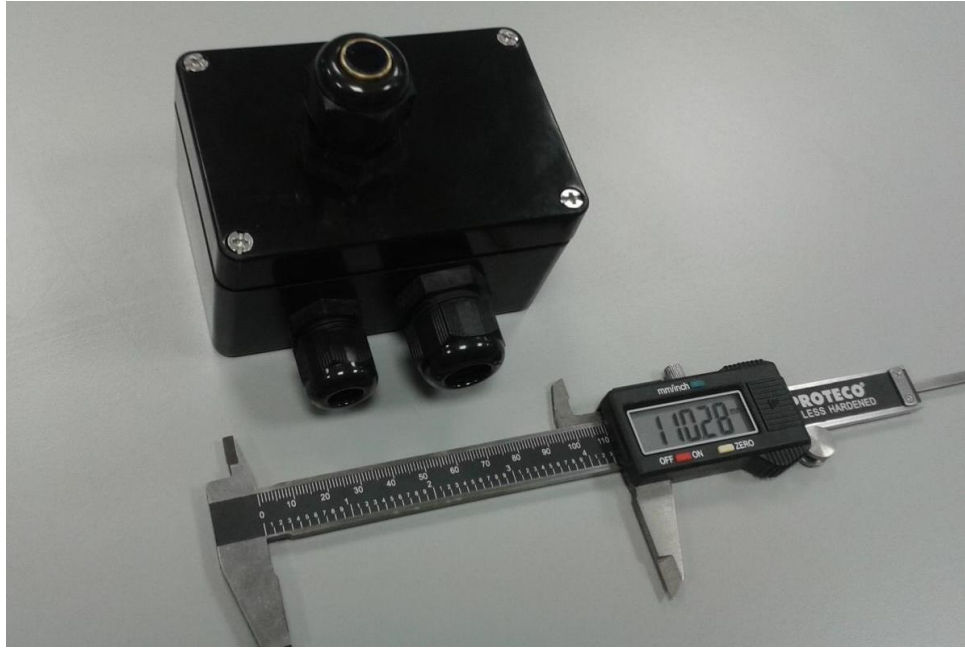


*Figure 4.1: AMON - the prototype of airglow monitor detector.*

#### 4.1.2 Selection of the suitable data for the analysis

The main condition for the airglow measurements analysis is the selection of the data based on the altitude of the Sun above the horizon. The brightness of the day sky is  $\sim 10^7$  times higher than the brightness of the night sky. Therefore the AMON measurements are not possible during the day, to protect the very sensitive PMT before damage. Also when the Sun is below the horizon the twilight sky is still too bright due to scattering of the sun light in the atmosphere. The common used phrase ‘the astronomical dusk’ describe the instant when the Sun is at 18 degrees below the horizon and the following night is dark enough for the astronomical observations. The sensitivity of the AMON with respect to the Sun altitude is plotted in the Figure 4.2 and Figure 4.3 for the dusk and dawn period, respectively.

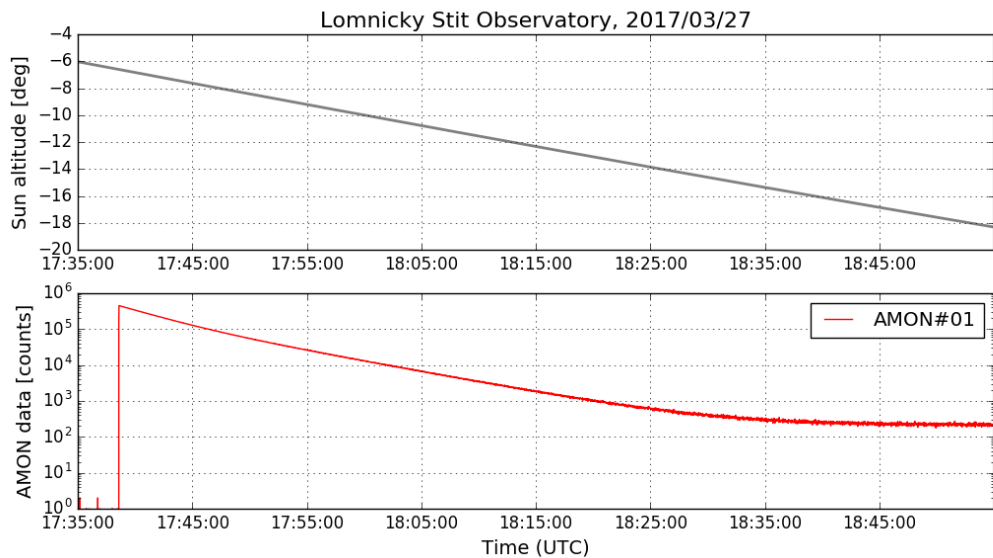


*Figure 4.2: Top: The altitude of the Sun above the horizon (the negative values represent the fact that Sun is already below the horizon). Bottom: The measurements of the AMON#01 detector located at Lomnický Štít Observatory. The y axis is displayed in the logarithmic scale.*

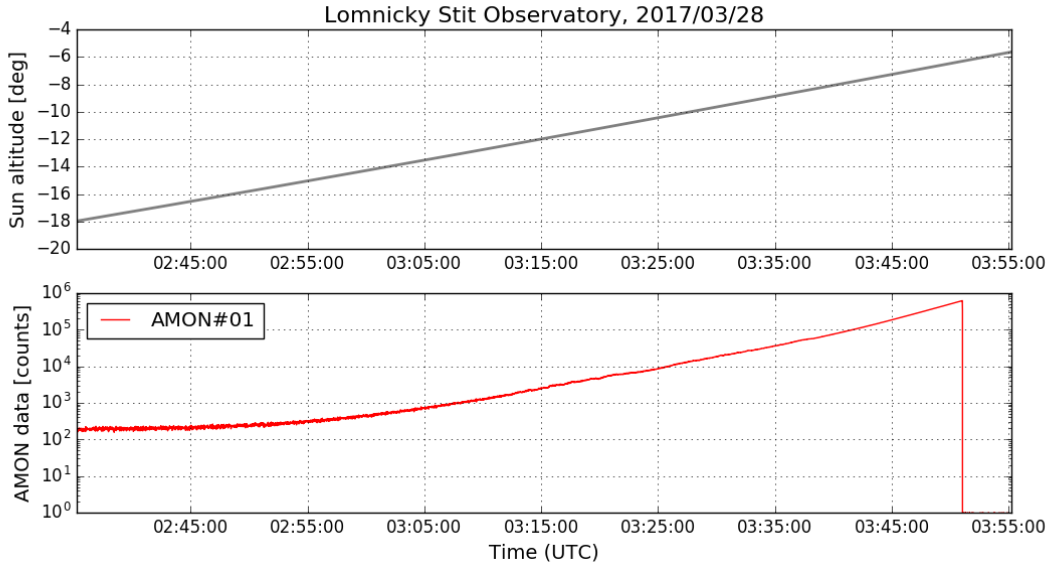


*Figure 4.3: The same as in the Figure 4.2 but for the dawn period.*

The second most important condition for the data selection for the analysis is the exclusion of the moonlight effect. During the Full Moon period (see Figure 4.4), the measured intensities are  $\sim$  tens times higher than during the New Moon period (see Figure 4.5). As it is presented in the Figure 4.6, when the Moon is above the horizon the data are contaminated by the moonlight. Therefore, only the data when the Moon is below the horizon (its altitude is  $< 0$  degrees) can be used for the analysis.

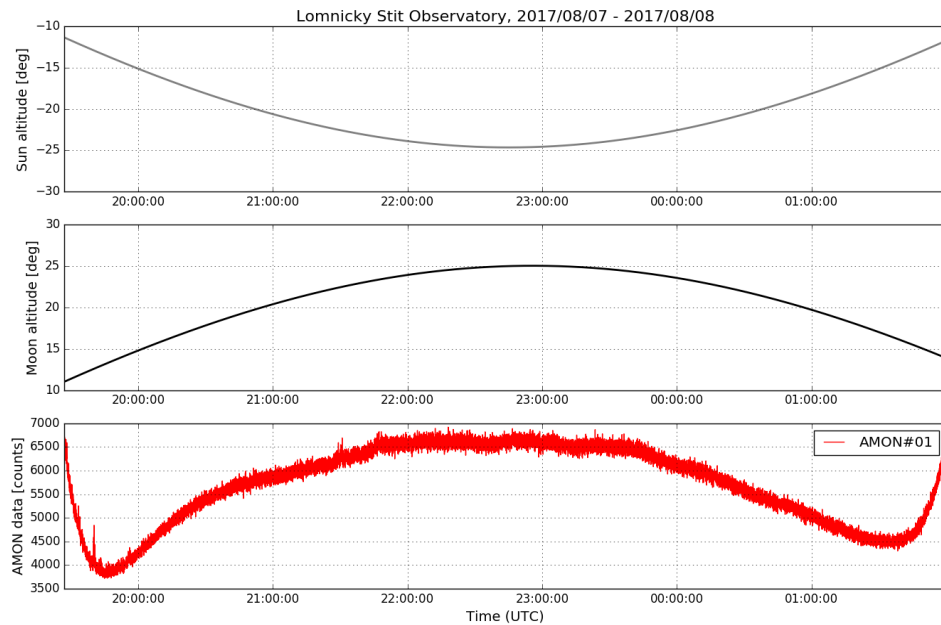


*Figure 4.4: Top: The altitude of the Sun above the horizon. Middle: The altitude of the Moon above the horizon for the Full Moon period. Bottom: The measurements of the AMON#01 detector located at Lomnický Štít Observatory.*

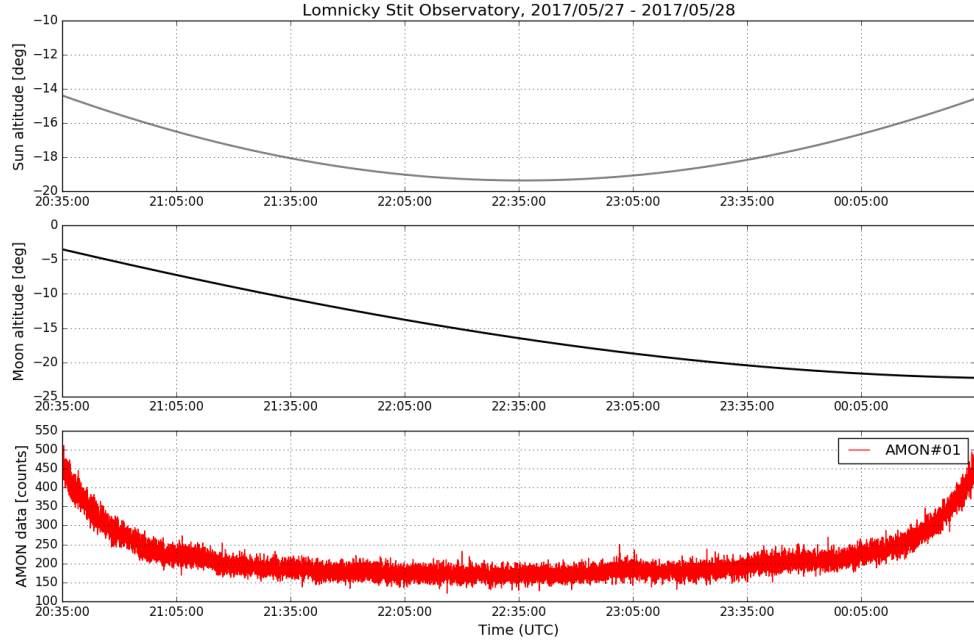


*Figure 4.5: The same as in the Figure 4.4 but for the period 2 days after the New Moon.*

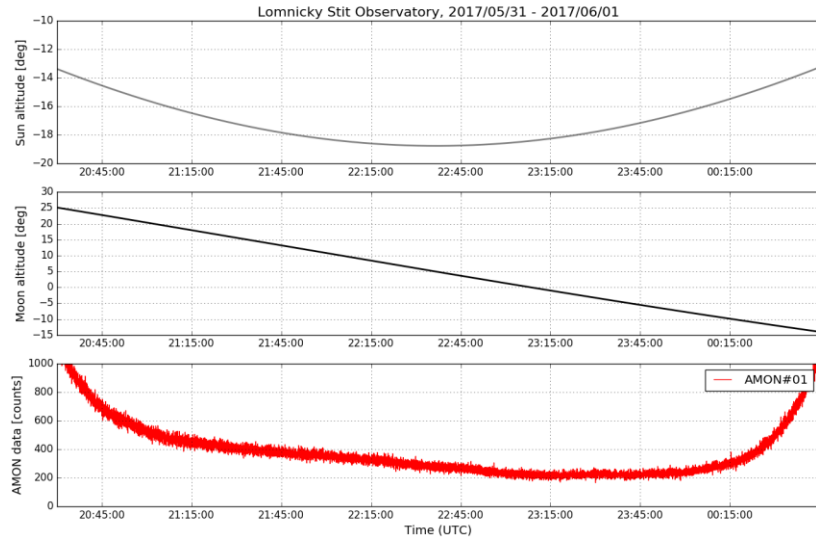


*Figure 4.6: The same as in the Figure 4.4 but for the period 6 days after the New Moon.*

The another source of the AMON measurements light contamination is the presence of the bright astronomical objects in the FoV. The presence of the bright stars can be recognized and eliminated from the data easily. The star which passing the FoV is represented as a sudden increase and decrease of the intensity (see Figure 4.7). The distribution of measured intensities during several minutes when stars are in detector FoV become non Poissonian. Precise condition applied was a comparison of square root of

measured intensity multiplied by 1.5 with standard deviation of all intensities measured during 5 minutes. If standard deviation was smaller, data were included to the analysis. Coefficient 1.5 was chosen as parameter to select data without stars (see Figure 4.18).

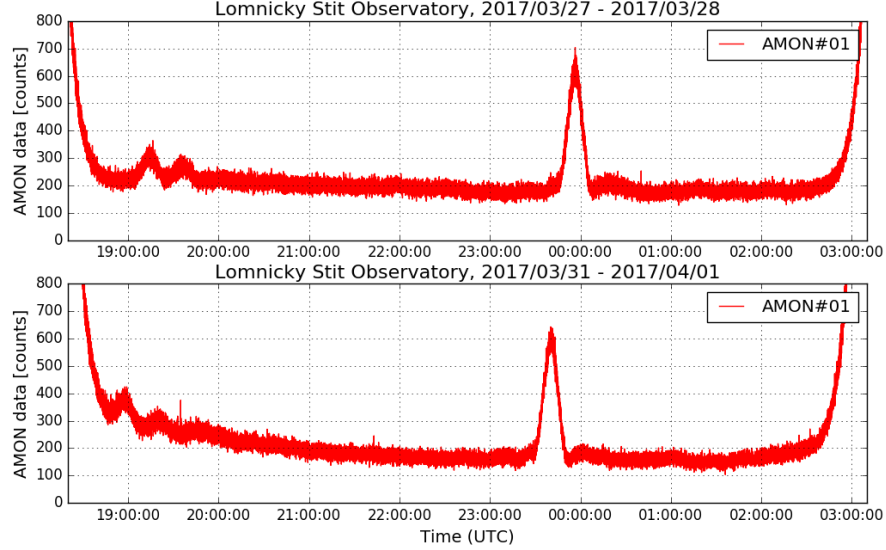


*Figure 4.7: The AMON#01 measurements for two nights (top and bottom). The light contamination by the star Alkaid ( $\eta$  UMa, spectral type B4V) can be seen as the peak at the midnight.*

The elimination of the effect of the groups of stars, as it is in the Milky Way, is not so straightforward. This issue could be overcome by specific pointing orientation of the detector. In the Figure 4.8, the measurements by AMON#01 and AMON#02 are displayed for the same time. Both of them were located at Lomnický Štít Observatory (LSO) while the AMON#01 pointed to the zenith and the AMON#02 pointed to the north celestial pole. The measurements in the May were not affected by the presence of the Milky Way in the FoV. But the measurements of AMON#01 in July started to be influenced by Milky Way light (see Figure 4.9). According simulations of the night sky movement during the year for the LSO location, the Milky Way is passed the zenith from July to December. Therefore the pointing orientation to the north celestial pole is much more convenient.

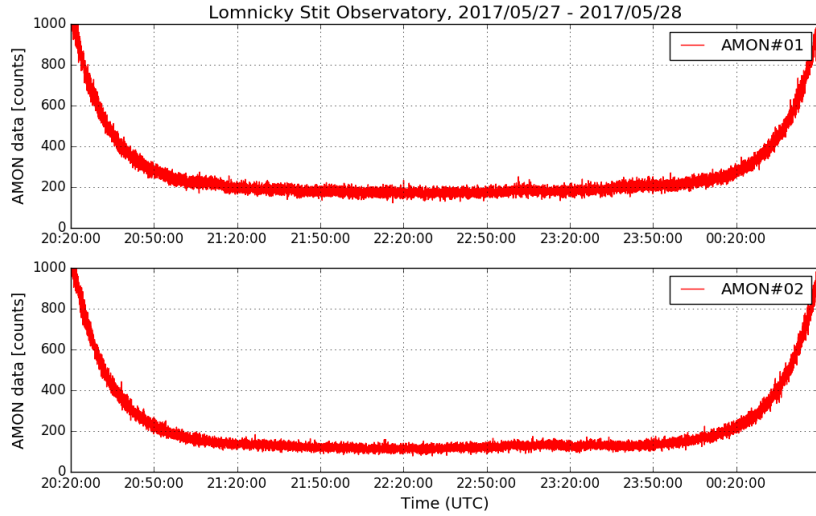


*Figure 4.8: Top: The AMON#01 measurements with pointing to the zenith. Bottom: The AMON#02 measurements with pointing to the north celestial pole. The measurements are not affected by the presence of the Milky Way.*

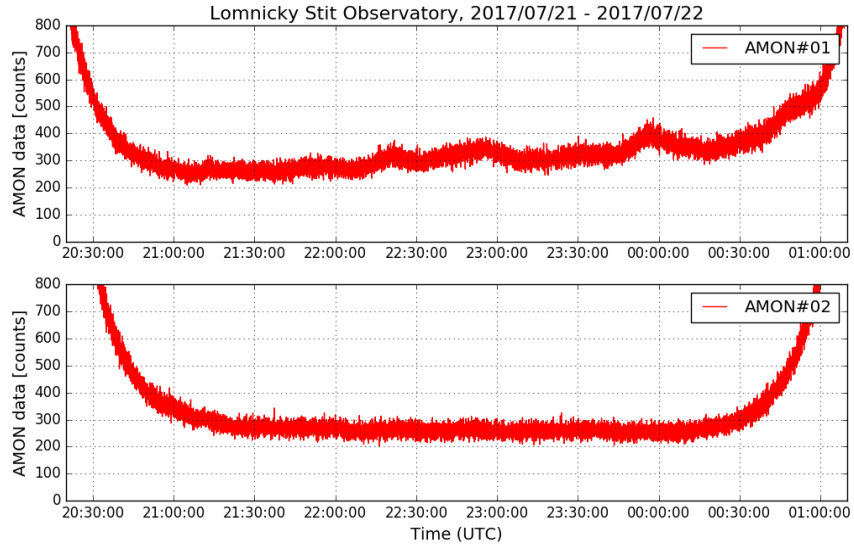


*Figure 4.9: The same as in the Figure 4.8 but the AMON#01 data (top) are contaminated by the light of Milky Way.*

All of the above mentioned conditions are predictable and the appropriate data for the analysis can be selected by well defined rules. The selection process is not predictable for the weather conditions. According the results presented in the Section 3.1.2 the main weather condition that needs to be filtered out properly is the cloud coverage. We have employed three types of the approaches to make a confident selection of the clear sky night hours.

The first type were the simulated data of the cloud coverage from the forecast model initially developed at the University of Basel (Switzerland) that are available for scientific usage (<https://content.meteoblue.com/en/products/time-dimensions/history/weather-simulation-data>). They provide percentage of low, middle and high cloud coverage for any location on Earth with sufficient precision. The second type of the data are the measurements of the cloud coverage by simple infra-red detector of clouds (<http://space.astro.cz/meteo/LS/LS-M0/data/2017/>). The time series for the both data types and for period 2017-02-26 - 2017-04-12 are plotted in the Figure 4.10. The periods where the temperature is low are consistent with the cloudless situations according the model. This could be explained by the following fact. When there are no clouds the infra-red sensor measures temperature of higher atmospheric layers which are colder. However, this assumption was not confirmed for all observations. Therefore the precise characterization of the cloud coverage for particular observations is a mandatory task. The example of AMON measurements during the clear sky and cloudy conditions are displayed in Figure 4.11 and Figure 4.12, respectively.

The third approach that used the AMON data directly is described in section 4.2.1.

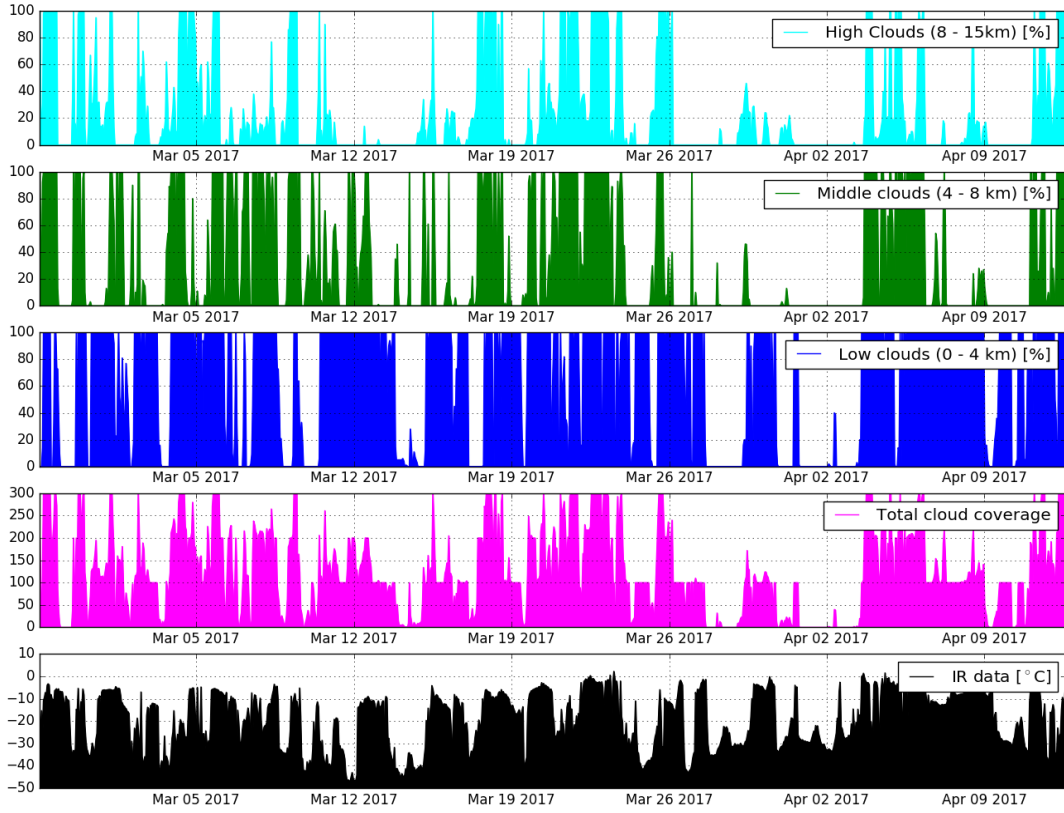


*Figure 4.10: The time series of cloud coverage from the simulated data for high clouds (first row), middle clouds (second row), low clouds (third row), total cloud coverage - the sum of cloud coverage for all altitudes (fourth row), and the measured temperatures of the sky by infra-red sensor (fifth row).*

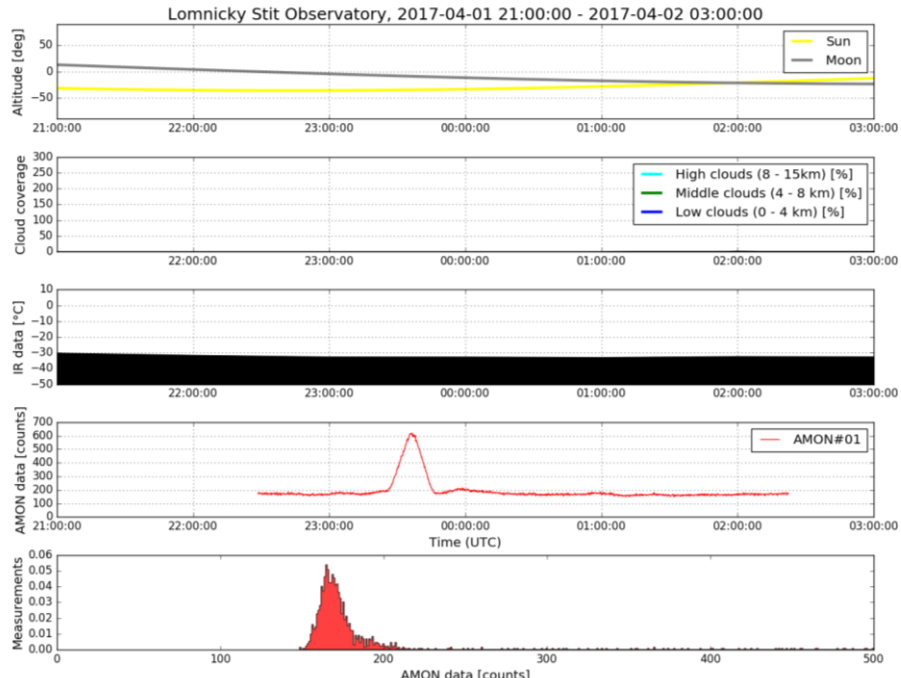


*Figure 4.11: The example of AMON measurements during clear sky conditions of particular night. The first row: The altitude of the Sun and the Moon. The second row: The cloud coverage according the meteoblue.com model data (in this case - no clouds). The third row: The temperature measured by the*

*IR sensor. The fourth row: The AMON#01 data. The clear sky is also indicated by presence of the star.*  
*The fifth row: The histogram of AMON#01 data.*

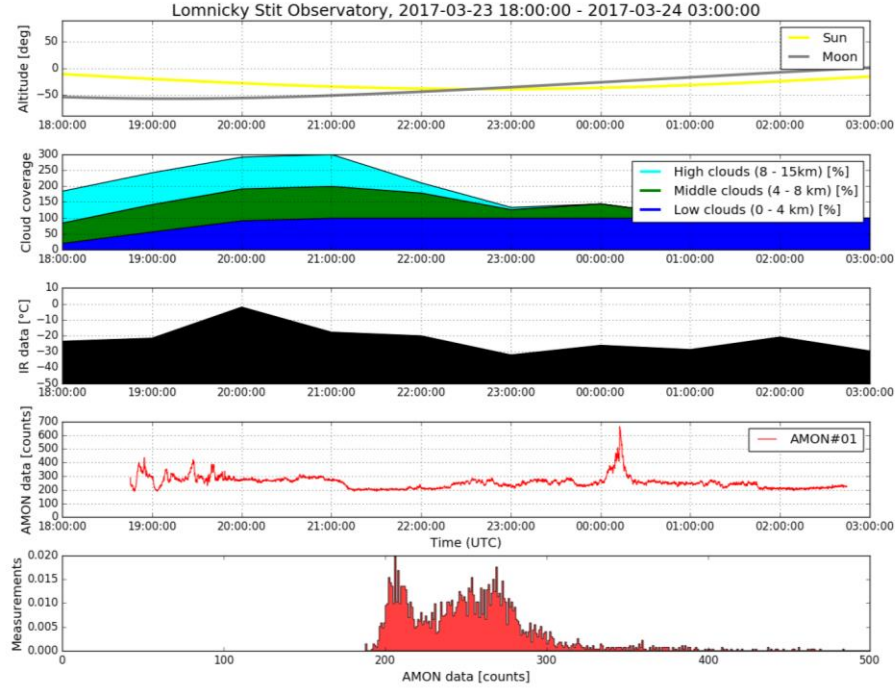


*Figure 4.12: The same as in Figure 4.11 but for cloudy conditions.*

### 4.1.3 Analysis of AMON measurements – general view

The four instruments of one pixel UV detector for airglow monitoring (AMON) operate at four location, in the present time (March 2018). The list of observational sites with the position information is presented in the Table 4.1. The pictures of the AMON instruments at these sites are displayed in the Figure 4.13.

*Table 4.1: The locations of the AMON instruments operation in the present time.*

Observational site	Acronym	Latitude [deg]	Longitude [deg]	Altitude [m a.s.l.]
Lomnický Štít Obs. (Slovakia)	LSO	49.19	20.21	2634
National Astronomical Obs. San Pedro Martir (Mexico)	OAN	31.05	-115.46	2788
El Roque de Los Muchachos Obs. La Palma (Spain)	ORM	28.76	-17.89	2167
Karby, Stockholm (Sweden)	STO	59.55	18.20	29

The data relevant for the analysis, presumably not affected by any contamination (light from the Sun, Moon, bright stars, clouds) are displayed in the Figures 4.14 – 4.17. The AMON data are presented together with the daily averages of the Dst index that characterizes the evolution of geomagnetic storms. Each point in the AMON plot represents the mean value of the measurements for particular night together with its standard deviation. An example of one night measurements from ORM observatory together with distribution of these measurements are presented in the Figure 4.18.



Figure 4.13: The pictures of AMON instruments at 4 locations. The name of the particular observation site is labeled on the top of each picture.

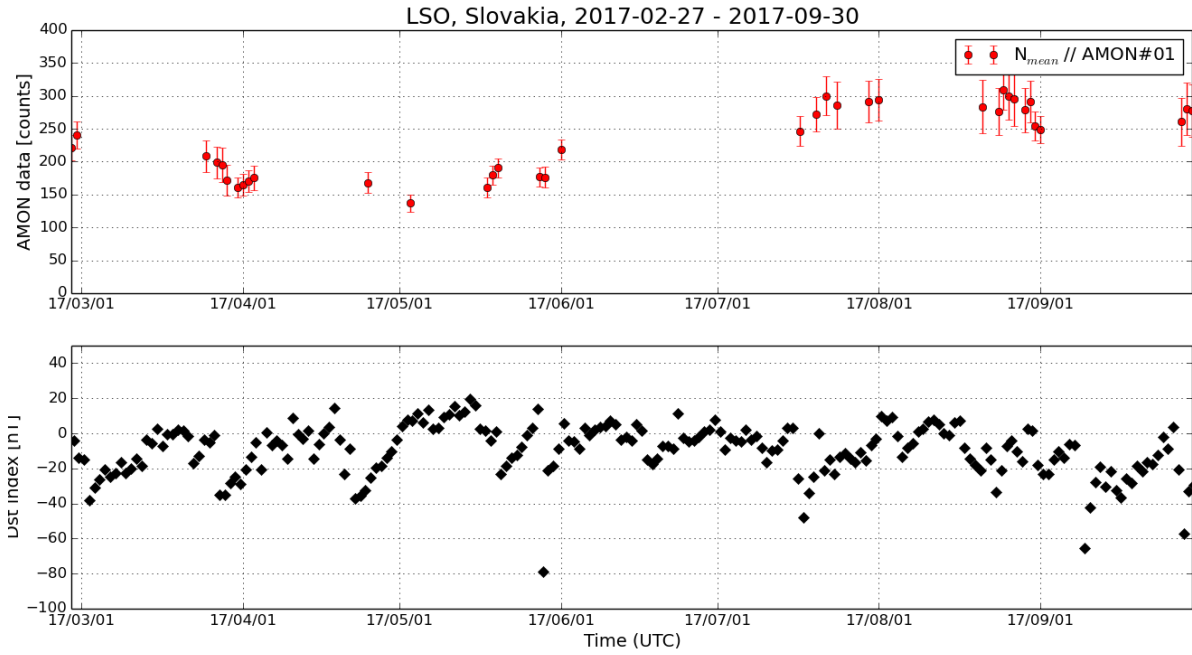
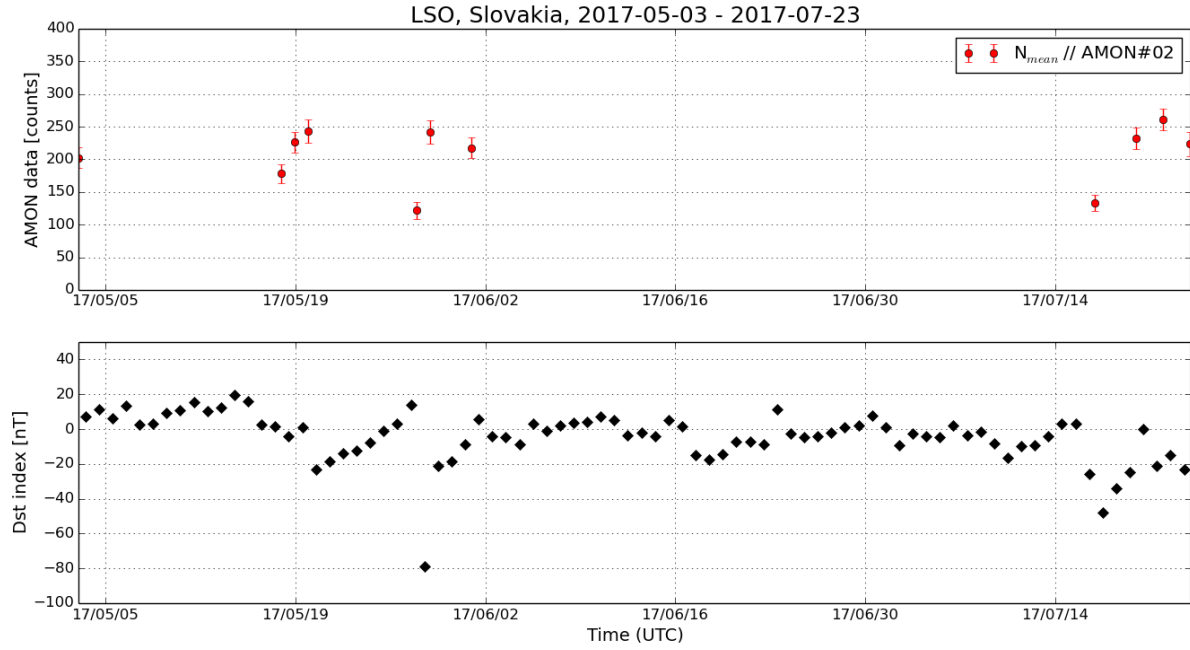
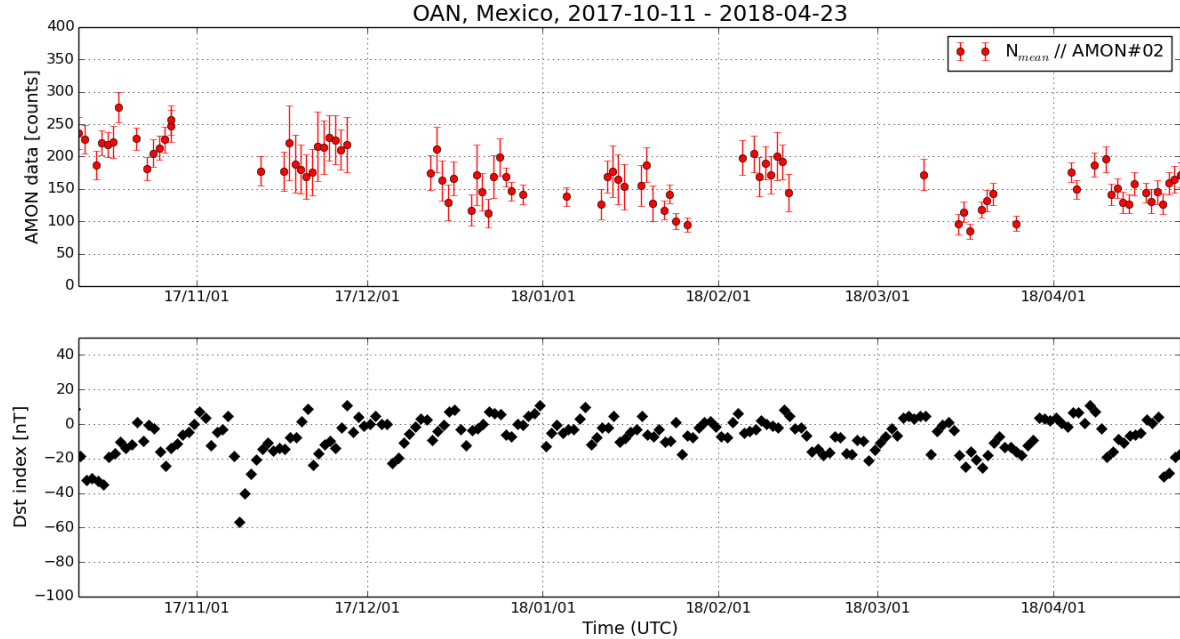


Figure 4.14: Top: The mean values with their standard deviations of AMON measurements at LSO. The AMON was pointed to the zenith. The instrument operation period is indicated on the top of the Figure and its serial number is labeled in the top right corner. Bottom: The daily averages of the Dst index.



*Figure 4.15: Top: The mean values with their standard deviations of AMON measurements at LSO. The AMON was pointed to the north celestial pole. The instrument operation period is indicated on the top of the Figure and its serial number is labeled in the top right corner. Bottom: The daily averages of the Dst index.*



*Figure 4.16: Top: The mean values with their standard deviations of AMON measurements at OAN. The AMON was pointed to the zenith. The instrument operation period is indicated on the top of the Figure and its serial number is labeled in the top right corner. Bottom: The daily averages of the Dst index.*

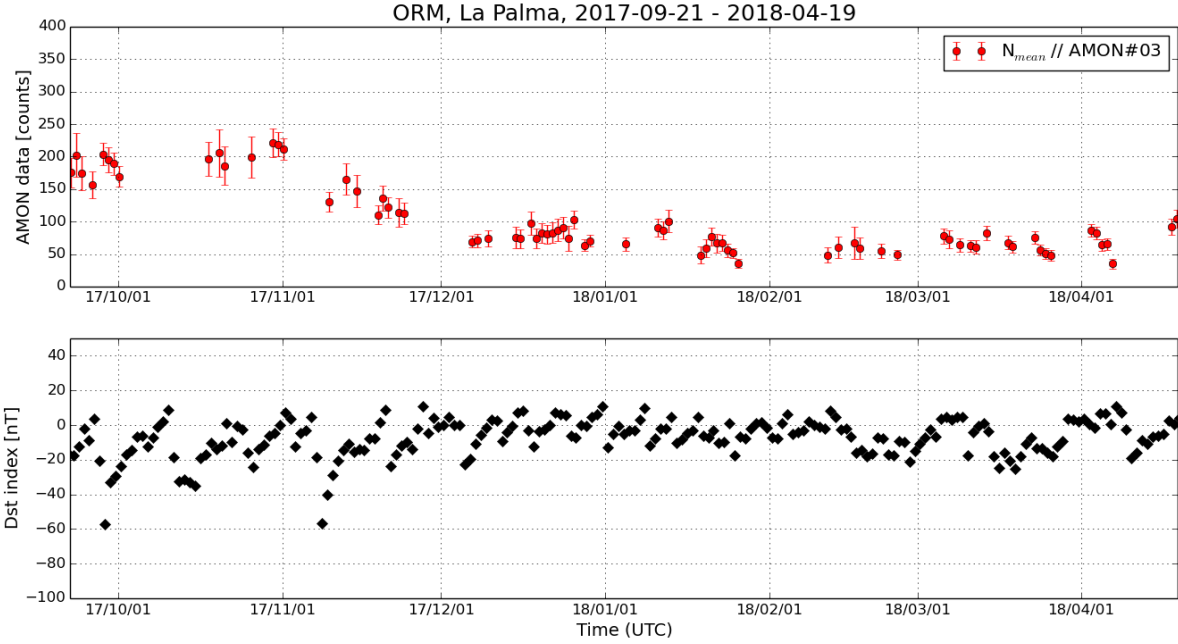


*Figure 4.17:* Top: The mean values with their standard deviations of AMON measurements at ORM. The AMON was pointed to the zenith. The instrument operation period is indicated on the top of the Figure and its serial number is labeled in the top right corner. Bottom: The daily averages of the Dst index.

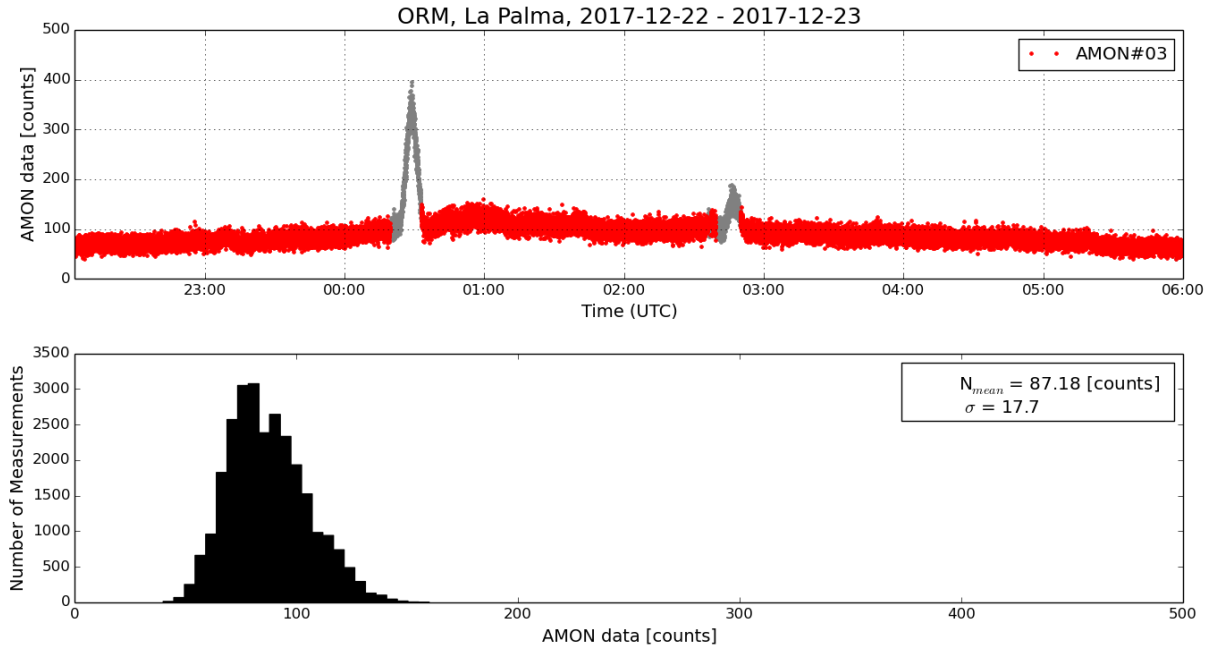


*Figure 4.18:* The detailed view of one data point from the Figure 4.17 (top). Top: The AMON measurements with the time resolution 1 s. The data used in the analysis are marked with the red dots. The peaks are originated by light contribution from bright stars. These contaminated data are marked with gray dots and they were excluded from the analysis. Bottom: The distribution of measured data. The mean value of these data is labeled together with its standard deviation in the top right corner.

We note, the duration of measurement during different night is not constant. It depends mainly on the

time when the Moon and Sun is below the horizon. The longest valuable measurements took ~ 10 hours and the shortest used ~ 1 hour. In total, AMON#03 and AMON#02 measured valuable (not contaminated) data during 57% and 46% of night hours of their continuous operation at OAN (Mexico) and at ORM (Spain), respectively. This is enormous higher percentage than for the LSO (Slovakia). On the other hand, unfortunately, the percentage of valuable measurements during night hours at STO (Sweden) site is lower than 1%. The AMON#04 operated there in periods April - May 2017, while the measurements were affected by the malfunction of the electronics and in November 2017 - February 2018, while almost all data were affected by the presence of clouds. There are no relevant data from AMON#01 LSO (Slovakia) since October 2017 due to technical issues of the instrument, presence of clouds and due to laboratory tests of this instrument since March 2018. This instrument will be placed in the new location in Slovakia at Astronomical Observatory on Kolonica Saddle from May 2018.

#### 4.1.4 Analysis of AMON measurements - detailed view

In this section, we are focusing on the several short period (several days) measurements that might be interesting for the study of ionospheric disturbances. Our whole project is concentrated on the possible monitoring of disturbances caused by geomagnetic storms. Therefore we compare AMON measurements with the Dst index values. According to the AURIC model of airglow production (see Section 2.2.3 and 3.2.1), the connection between UV airglow production and geomagnetic disturbances expressed by Dst index should be straightforward. In reality, these connections might be much more complicated and many different ionospheric processes might play the role.

According the AURIC model, during the disturbed period, that is indicated with decrease of Dst index, the measured airglow radiation is lower. The example of a scuh observation case is displayed in the Figure 4.19. The measured intensity by AMON during the night 27-28 May 2017 is significantly lower than the intensity measured during the night 28-29 May 2017. The detailed view of measurements used in Figure 4.19 together with their histograms are plotted in the Figure 4.20 and 4.21.

To confirm that this significant decrease of intensity is not caused by presence of clouds, we have employed measurements from external detectors at LSO. We have applied two methods presented by (Ahn et al., 2015) to the data from infrared (IR) sensor, thermometer and humidity meter. The first method is based on the comparison of the sky temperature, that is measured by IR sensor, with the simulated temperature of clear sky, that is estimated from the ground temperature and humidity. This method is effective for detection of optically thick clouds with low altitude. The second method is based on the variation of the sky temperature within the time period. If the standard deviation of the sky temperature measurements over the time period is lower than the set threshold, the sky is clear. This method is effective for detection of optically thin clouds with high altitude and quick movement. The measured data from external sensor together with the applied methods for cloud detection is presented in the Figure 4.22 and 4.23, while the time period overlaps the period in the Figure 4.19.

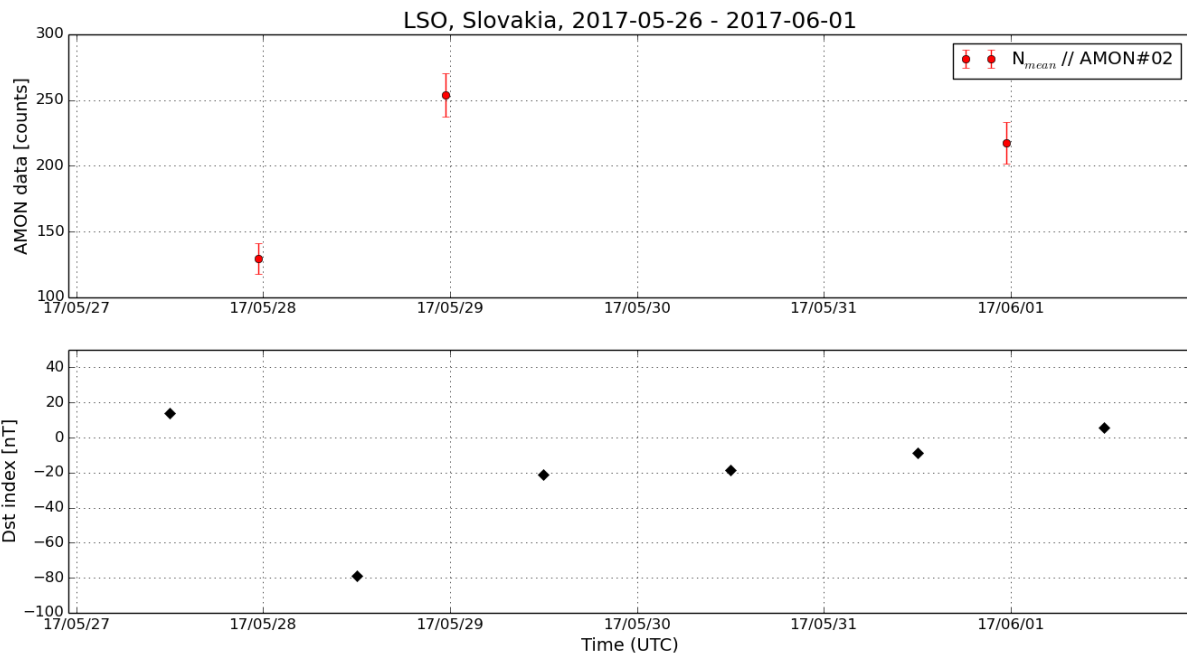


*Figure 4.19: The same as in Figure 4.15 but for period of 6 nights. The data from 23:10 to 23:30 UTC for each cloudless night are used.*

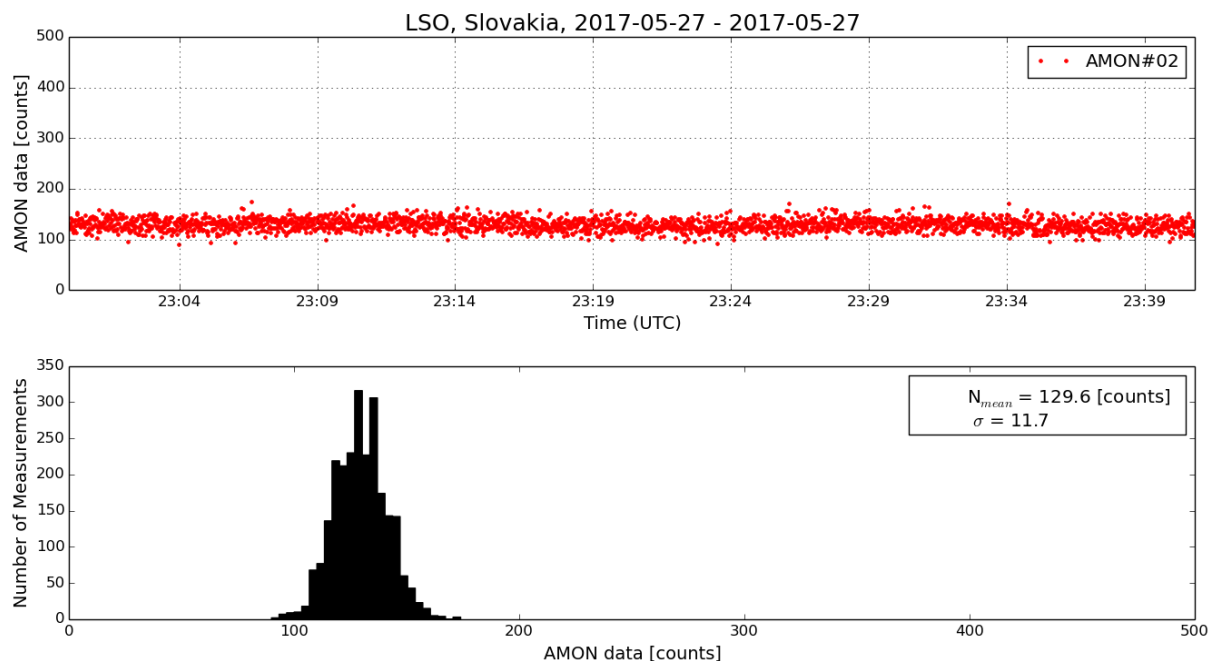


*Figure 4.20: The time series of AMON measurements (top) together with histogram of these data (bottom) during the night 27 - 28 May 2017.*

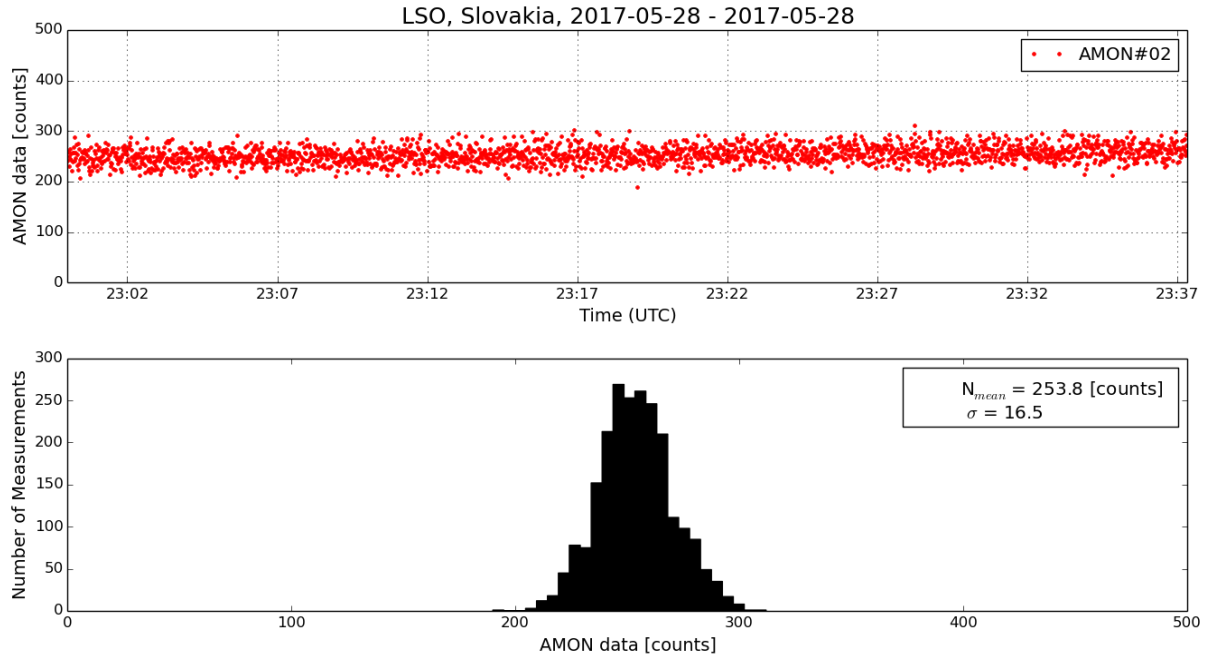


*Figure 4.21: The time series of AMON measurements (top) together with histogram of these data (bottom) during the night 28 - 29 May 2017.*

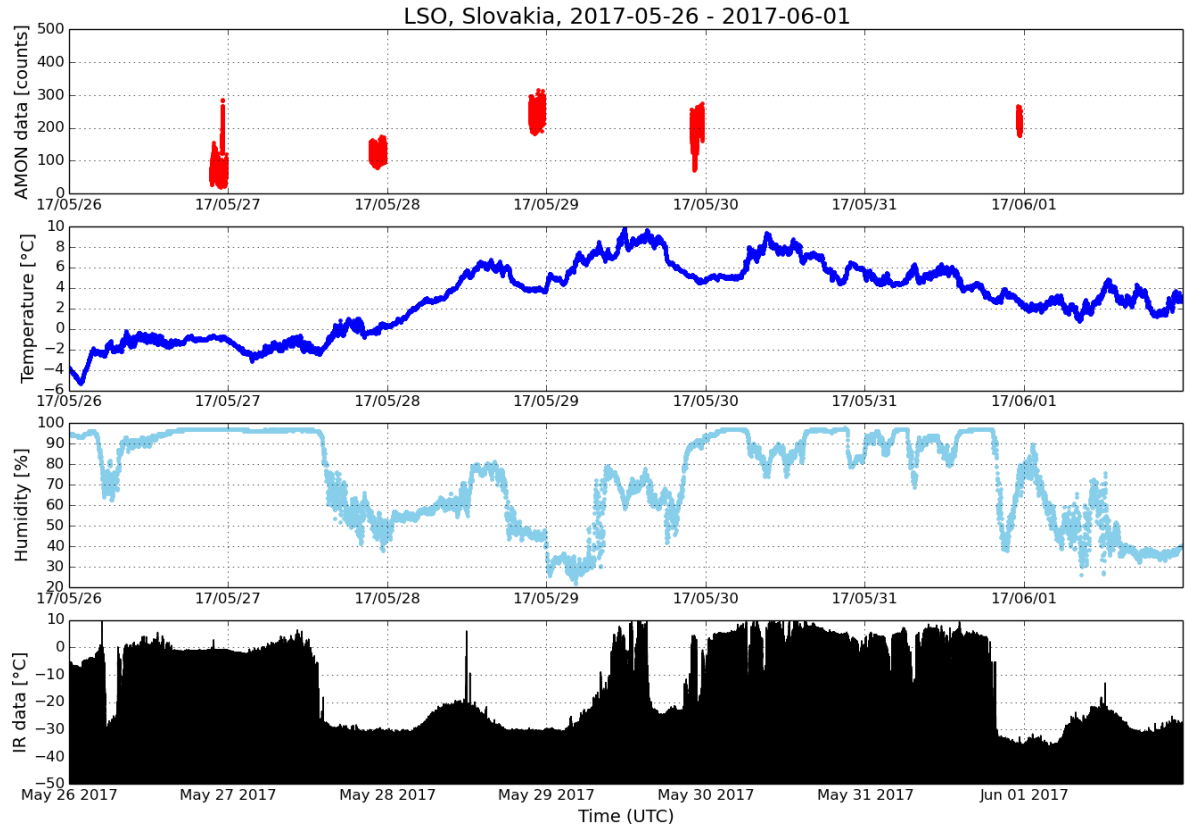


*Figure 4.22: First row: The AMON measurements that are not contaminated by the light from Moon and Sun. Second row. The measurements of ground temperature [ $^{\circ}\text{C}$ ] by external thermometer located at LSO. Third row. The measurements of ground humidity [%] by external humidity meter located at LSO. Fourth row: The measurements of sky temperature [ $^{\circ}\text{C}$ ] by external IR sensor located at LSO.*

The measurements during night 27 - 28 May 2017 might be slightly affected by optically thin clouds (Figure 4.23, second and third row) during a few minutes. But most of the night, the sky was clear. It is coincidentally documented by picture taken by DSLR camera from place nearby High Tatras Mountains (where LSO is located) at 23:00 on 27 May 2017 (Figure 4.24).

In general, presence of clouds decrease the measured intensity of airglow as the clouds block the downwelling radiation. This is the case for AMON measurements during the night 26 - 27 May 2017. But the low intensity measured during night 27 - 28 May 2017 is not caused by presence of clouds but probably by ionospheric disturbances. Another examples of significant variations of measured intensity is in Figure 4.25 and 4.26. The displayed AMON data were measured during the cloudless conditions. It was confirmed by the same methods as we used in the Figure 4.23.

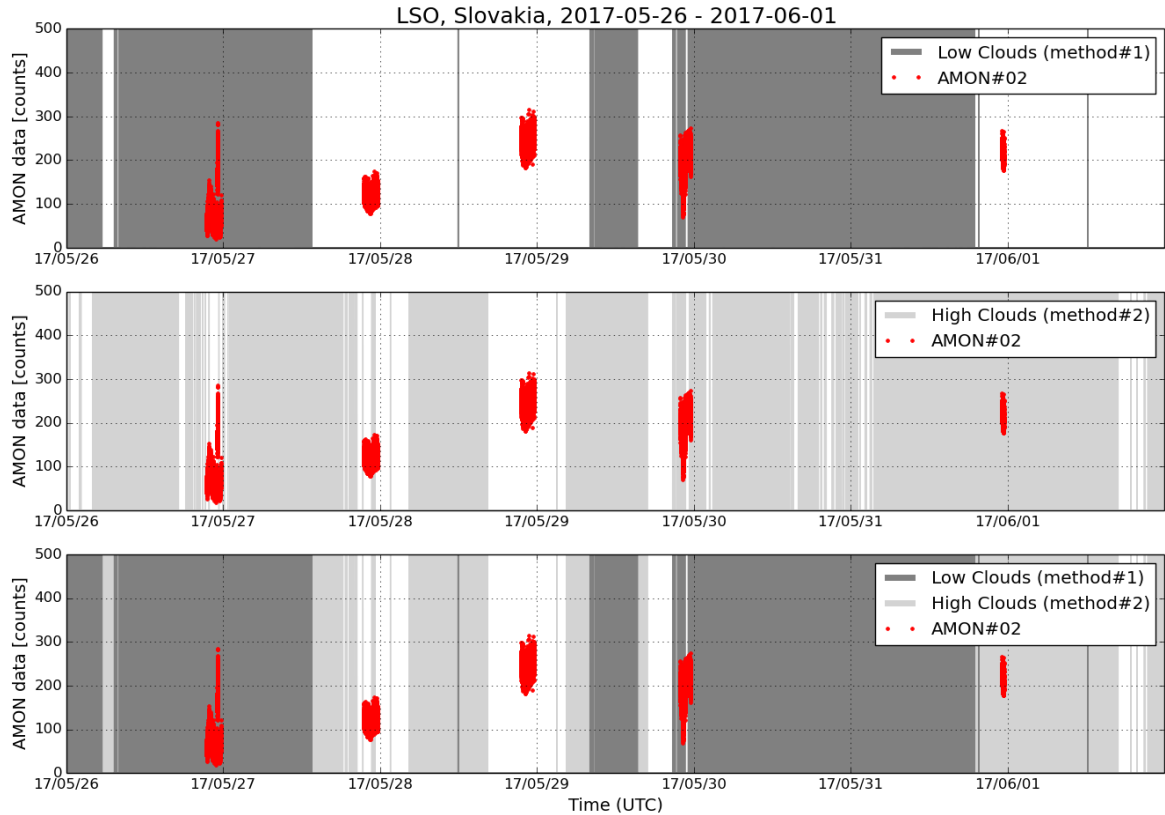


*Figure 4.23: First row: The AMON data (the same as in Figure 4.22, first row) together with results of the first method described in text. The presence of low clouds is indicated with dark gray filling. Second row: The AMON data together with results of the second method described in text. The presence of high clouds is indicated with light gray filling. Third row: The AMON data together with results of both methods for cloud detection. The white are represent the period without any clouds.*



Figure 4.24: High Tatras panorama taken by DSLR camera on 27 May 2017 (S. Mackovjak)

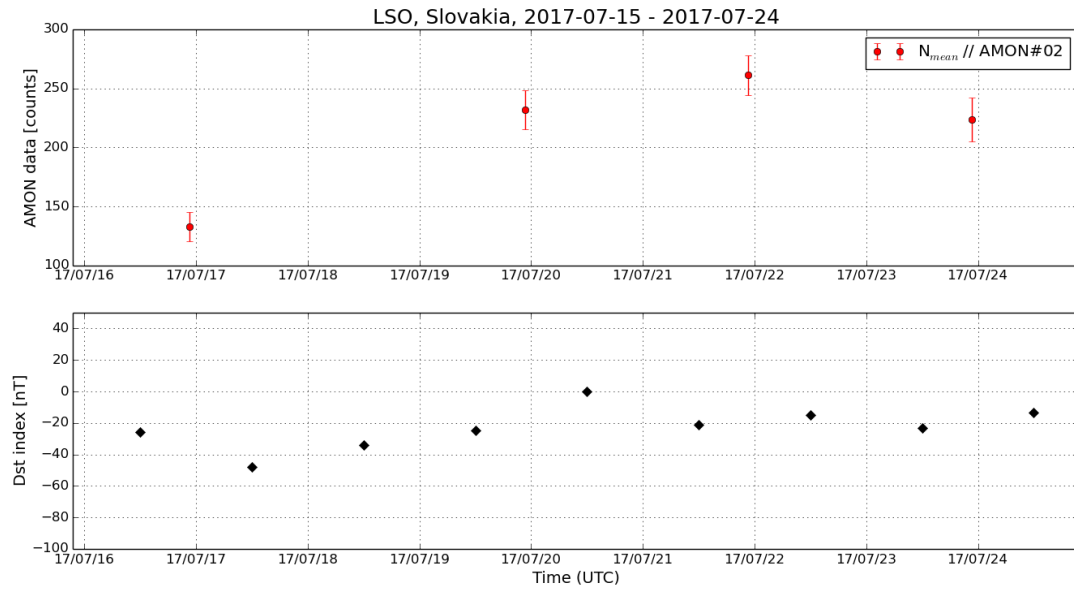
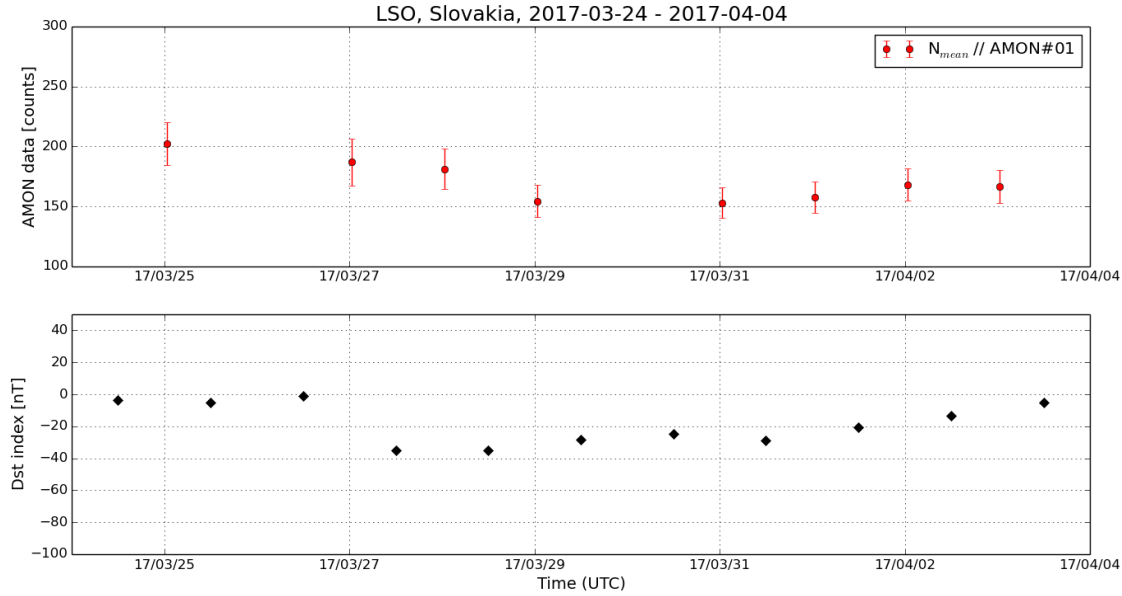


Figure 4.25: The same as in Figure 4.19 but for period 15 - 24 July 2017. The data from 21:30 to 22:30 UTC for each cloudless night are used. The significant low intensities were measured during night 16 - 17 July 2017. During this night, the ionosphere was disturbed by geomagnetic storm, which is expressed by decrease of Dst index.



*Figure 4.26: The same as in Figure 4.19 but for period 24 March - 04 April 2017. The data from 00:20 to 01:00 UTC for each cloudless night are used. The significant low intensities were measured during night 28 - 29 March 2017. During the period of several nights, the ionosphere was disturbed by geomagnetic storm, which is expressed by decrease of Dst index.*

We have also observed several other significant variations of the measured AMON intensities. But their connection to the ionospheric disturbances caused by geomagnetic activity is not so straightforward. The examples are in the Figures 4.27 – 4.30. The explanation of these variations as a consequence of clouds presence was excluded.

Here it is important to note that since half of November 2017 the geomagnetic activity is very quiet and the Dst index is not lower than -30 nT. Even more, the OAN and ORM observational sites are located at low latitudes that make detection of geomagnetic disturbances even more difficult. Nevertheless, we were able to detect some noticeable variations in the AMON measurements. It can be seen from the data of the subsequent nights that are displayed in the Figure 4.27. During the nights 20 - 24 December 2017, the measurements indicate unchanging ionospheric conditions. However, the measurements before and after this period indicate noticeable change of the measured ionospheric conditions. According detailed inspection of the weather conditions for these nights, the noticeable variation was not caused by presence of clouds. So the possible interpretation is that some ionospheric disturbances were presented in 19 December and 25 December that caused the variation of density of molecular oxygen ( $O_2$ ) which is responsible for airglow light production in UV range.

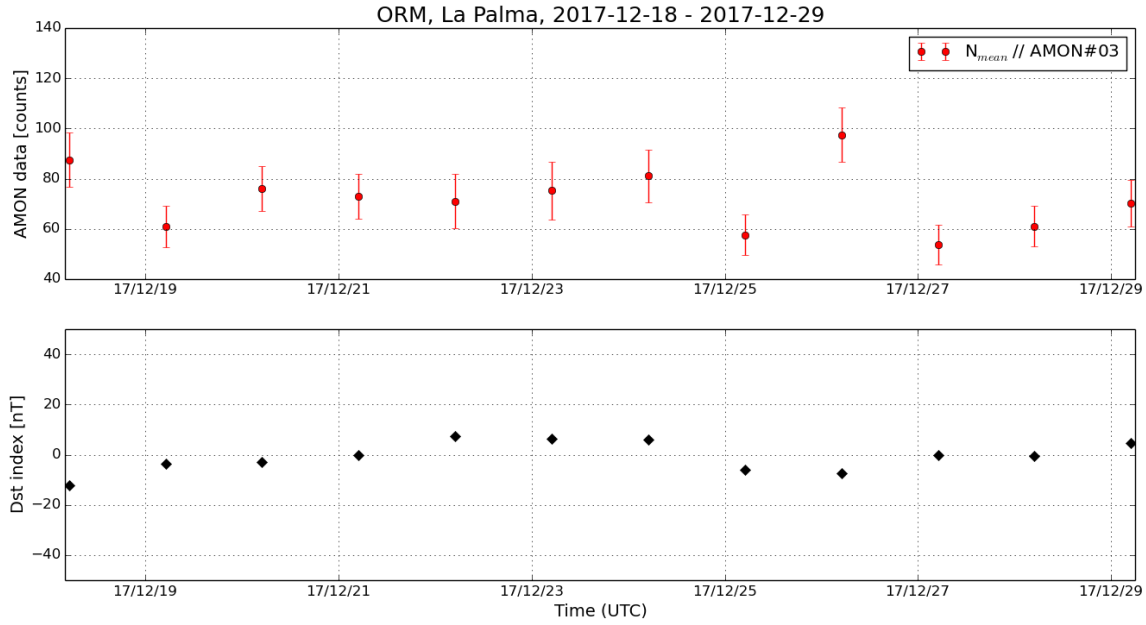


*Figure 4.27: The same as in Figure 4.17 but for period 18 - 29 December 2017. The data from 04:00 to 06:00 UTC for each night are used.*

The observational case displayed in the Figure 4.28 is different as it was expected according cases displayed in the Figures 4.19, 4.25, and 4.26. The variation of AMON data seems to be not related to the geomagnetic disturbance expressed by variation of Dst index.

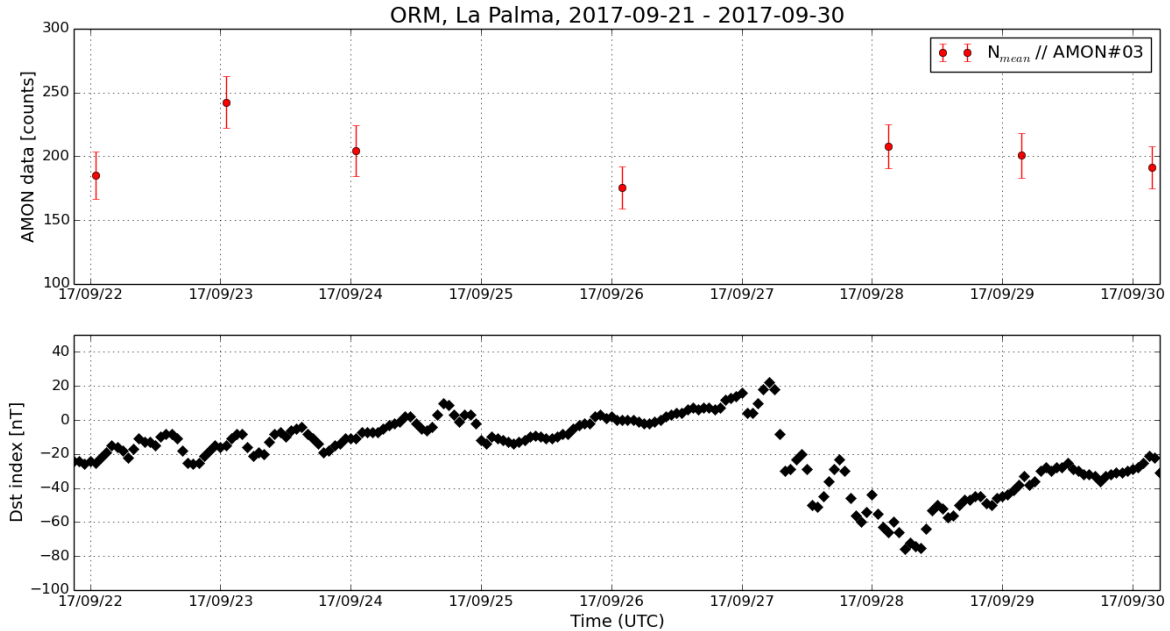


*Figure 4.28: The same as in Figure 4.17 but for period 21 - 30 September 2017. The data from 03:00 to 05:00 UTC for each night are used. Although the geomagnetic storm occurred on 28 September, the measured intensity didn't change significantly.*

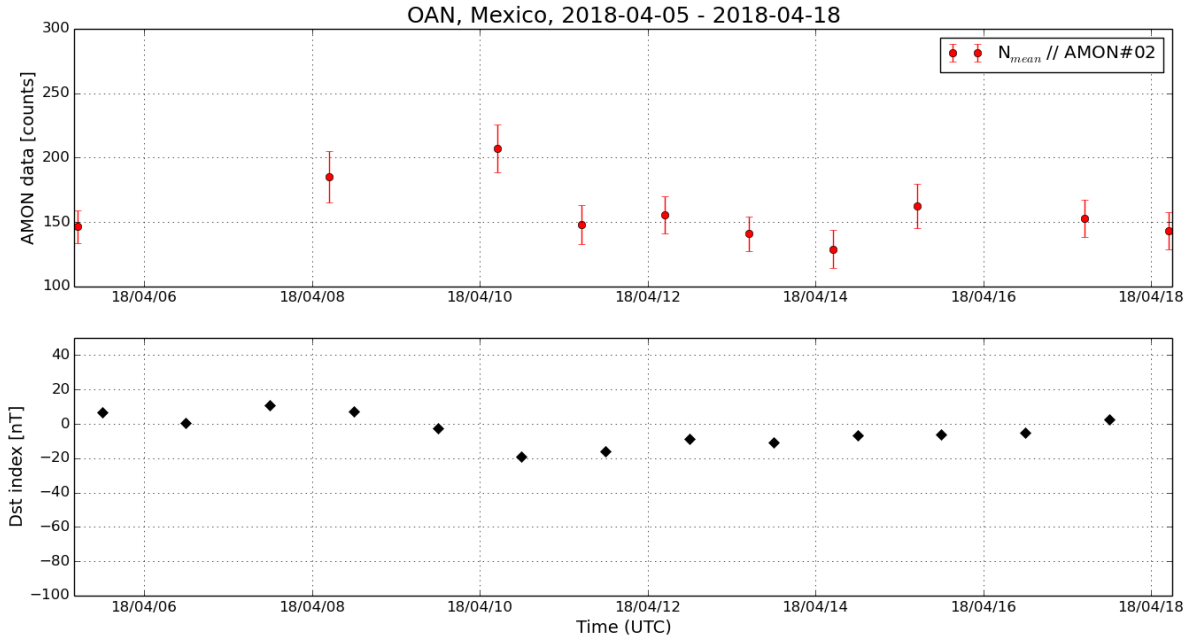


*Figure 4.29: The same as in Figure 4.16 but for period 05 - 18 April 2018. The data from 04:00 to 06:00 UTC for each night are used. The Dst index indicates quiet magnetosphere but measured intensities variated.*

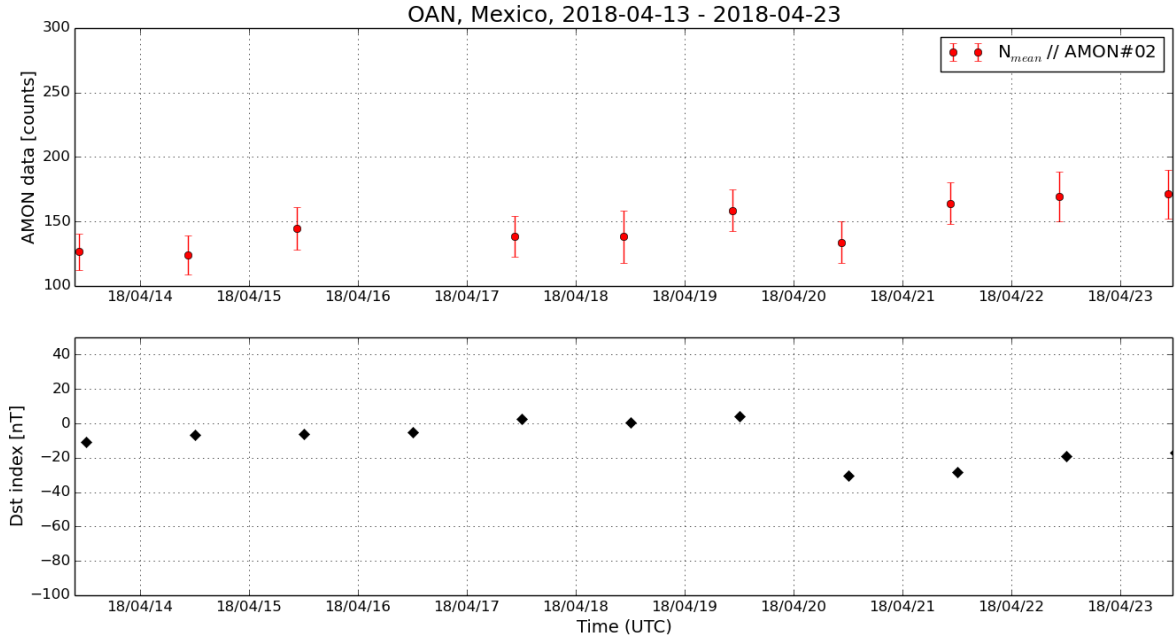


*Figure 4.30: The similar period as in Figure 4.29 (period 13 - 23 April 2018) but the data from 09:30 to 11:30 UTC for each night are used.*

All of these results demonstrate that AMON is able to detect some variations in the upper Earth's atmosphere. But two tasks are mandatory. At first we need to precisely filter out all sources of data contamination. This task was performed in our analysis but it needs to be performed in fully automated way. The second task is a wider understanding and monitoring of processes in the upper atmosphere. Then we will be able to associate the variation of measured intensities to the ionospheric phenomena. To perform these tasks the follow-up project is desired.

#### 4.1.5 Statistical analysis of UV airglow data

The slope method (Section 2.2.1) works with one hour step, due to Dst index one hour step. During five months measurements of AMON#01 at Lomnický štít (LSO), number of hours with moonless night measurements was 400. This number was reduced to 83 hours due to presence of clouds. And than it was reduced to 58 hours due to presence of stars and Milky Way. The measurements from these 58 hours were used for Slope method analysis. The Slope method compares nights intensities with preceding night intensities. As we have shown in Sections 2 and 3, length of preceding window could be only one night. Even with one night long window the method works well. We choose one night long window to maximize number of nights in analysis. Because clouds appear in most of the nights, the two consecutive nights with at least 30 minutes long cloudless periods are more frequent than longer periods. In Sections 2 and 3 analysis from model results we used nights longer than 3 hours. For analysis of measured intensities we exclude this condition, with same intention to maximize number of nights in analysis.

The final number of points at Slope method graph is representing number of nights whose intensities could be compared with preceding night. The final number is nine points. The Figure 4.31 shows a B slope evaluation for full range of Dst indexes.  $B_1$  parameter which shows B slope in range from  $-50\text{nT}$  to  $0\text{nT}$  will limit five from nine point in full range analysis. B slope does not show any significant dependency of intensity changes on changes of geomagnetic indexes represented by Dst index.

Inspection of figures from Section 2.2.1, which show models results indicate that points shown in Figure 4.31 are in area covered by points from bigger statistics. That nine points are not sufficient to show relevant result in Slope method. The nine points in Slope method analysis does not show any final negative or positive conclusion about feasibility to observe geomagnetic disturbance in AMON measurements.

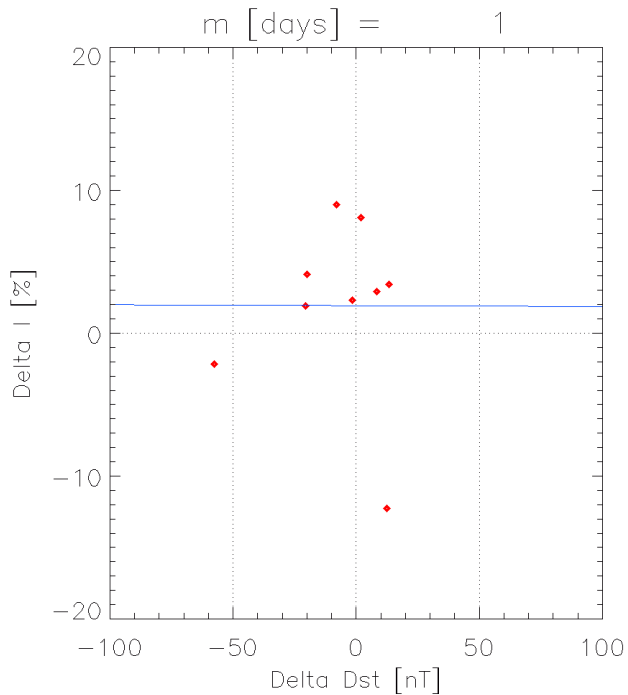


Figure 4.31: Slope method result for Lomnický štít measurements. Nights with preceding nights are presented as red diamonds. Blue line is linear fit of Slope method.

The measurements from AMON#02 and AMON#03 located in Mexico (OAN) and La Palma (ORM) are significantly less affected by clouds than measurements at LSO. So we apply slope method to these data. Here it is important to remind that since half of November 2017 the geomagnetic activity is very quiet and the Dst index is not lower than -30 nT. Because of low number of occurred storms, OAN and ORM data allow just limited statistical description.

The clean data (all contaminations mentioned above were excluded), were processed by slope method analysis for parameter  $m=5$ . Results are at Figures 4.32 and 4.33. For ORM we obtained 58 points and for OAN 75 points. Due to low statistics of geomagnetic storm occurrences, we don't provide meaningful fit in whole range of  $\Delta Dst$  and for range from -200 to -50nT. Data allow us to provide only the fit in range from 0 to -50 nT. In the Figures 4.32 and 4.33 on left side is absolute change in counts (not in  $ph/(m^2 ns sr)$ ) like it is shown for theoretical prediction in Section 3.2.1) with respect to absolute change in Dst. For ORM we can see that slope  $B_1$  is negative,  $-0.402$  count/nT and  $-0.561\%$  per nT. For OAN the absolute change of counts  $B_1$  is  $0.216$  count/nT and for relative change  $0.085\%$  per nT.

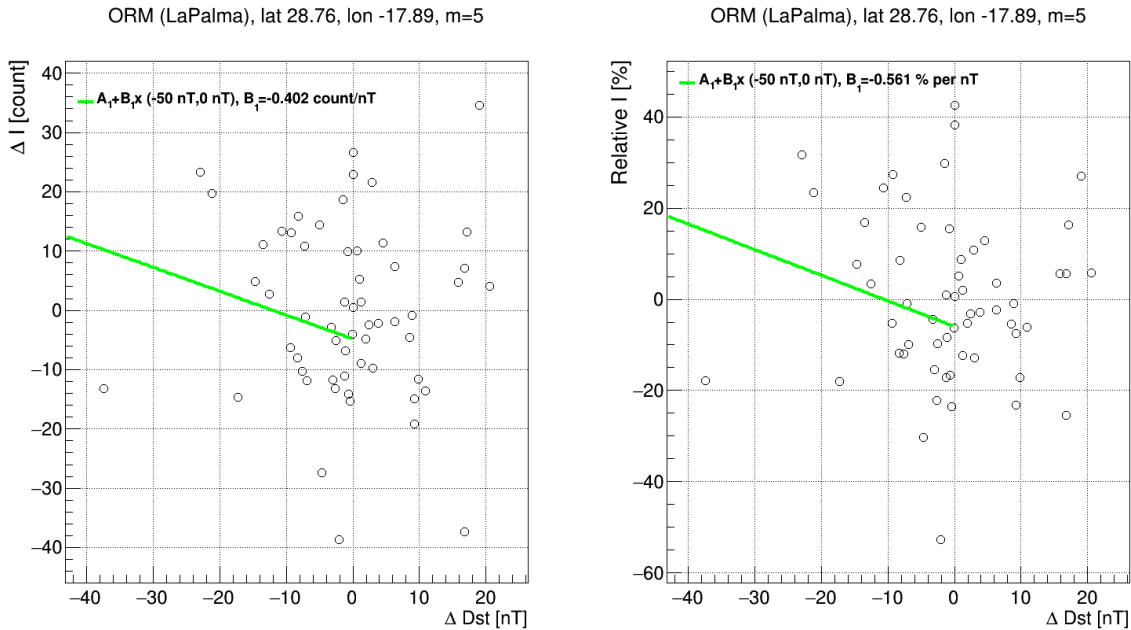


Fig. 4.32: Slope method for ORM position. Data consist of 58 points. On left side absolute change in counts (not in  $ph/(m^2 ns sr)$ ) and on right side relative change in percent with respect to absolute change in Dst.

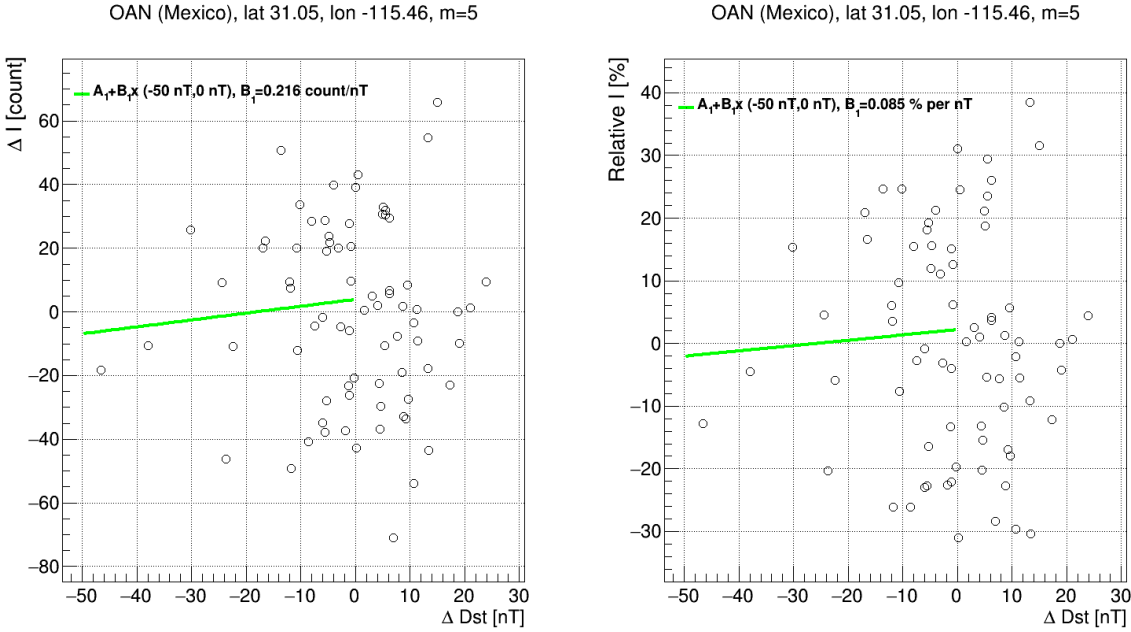


Fig. 4.33: Slope method result for OAN position. Data consist of 75 points. On left side absolut change in counts (not in ph/(m<sup>2</sup> ns sr)) and on right side relative change in percent with respect to absolute change in Dst.

Both positions are geomagnetically almost identical. Mexico geomagnetic position (geomag. latitude 37) is very close to the geomagnetic positions of La Palma (geomag. latitude 33). For this position we provided theoretical calculation in Section 3.2.1 (Tenerife position). This calculation took in to account not just airglow but also star and zodiacal light and transport of light through atmosphere. B1 parameter was 0.12 % per nT (see Figure 3.25, right). It is not clear at all why we obtain negative B1 parameter for ORM position in contrast to positive values of parameter obtained by model. It could be partially caused by very low statistic or unknown natural airglow variations. However in OAN (0.085 % per nT) position situation is more clear. This is ~70% of predicted value. It need to be taken in account that theoretical predictions depend on m parameter (see Figure 3.26). From Figure 3.26 we can see that for Tenerife position B1 parameter slightly decreased to value 0.1 % per nT for m=1. The value 0.12 % per nT was obtained for continuous data which doesn't suffer from any selection (except selection of solar zenith angle) mentioned previously. In case of real data they were cleared by several filters. It cause that statistics in m=5 window (real data) was in reality closer to model statistics corresponding to lower m. Of course 0.085 is still just 85% of 0.1. We could assume that measured data are between 70 and 85% of model prediction. This in our opinion is promising agreement between data and model which should be explored more in following projects focused on accumulation of more statistics under better weather monitoring.

In the end of this section we want to note that we developed simple statistic pattern recognition method to clean signal of AMON detector. The aim is to clean cloudy periods and periods with stars in detector FoV by dedicated algorithm and do it only from AMON intensities without help of meteorological data. The first example of such algorithm focused only on stars in detector FoV is in this report mentioned Poisson filter. Another algorithm focus on clouds and stars. Simple method for automatic searching of clear sky condition is based on assumption that during clear sky condition data will have smooth shape. Opposite, during cloudy condition we observe many peaks and valleys in the data. Of course some atmospheric phenomenon (local density fluctuations) could also produce peaks and valleys, but we

assume that such phenomenon have longer duration in comparison to fluctuation caused by clouds. In method we search each data point surrounding area. This area is defined by  $\pm 12$  minutes interval around given point. If 90 percent of points in this area is lower than given point (in case of peak) or higher (in case of valley) such area is candidate to be removed from our data. We tested also different intervals width for points selection and value  $\pm 12$  minutes give us best selection. To ensure that we don't remove very low fluctuations (because also in case of smooth data during clear sky condition small fluctuations appear) we check if average value of given point and two closest points on both sides is close to average value of rest of the points in selected area. Only if average value of rest of the points is out of interval given by  $\text{Ave\_3\_points} \pm (9\% \text{ of Ave\_3\_points})$ , fluctuation is selected and remove from data. In Figure 4.34 these points are marked such as a background (green). In the Figure 4.34 is shown example of such selection. Red points represent smooth data with one minute step. Green points represents removed peaks and valleys (one minute step). Black points show clear sky data with one hour step. For calculating of black points only red points was taken in account. Figure shows that method found smooth areas around star peak at 2:00 and around two small peaks and valley around 22:00. Method also marked some areas in earlier hours (before 21:00). These areas probably don't correspond to clear conditions.

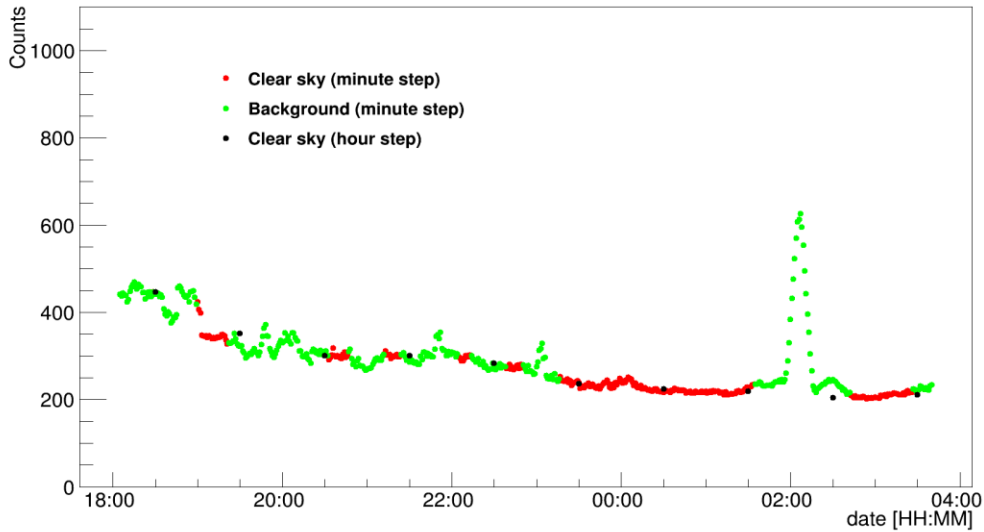


Figure 4.34: Simple method for automatic searching of clear sky condition results (see text for details).

## 5. Programmatic section

The main technical objectives of project were divided into three work packages. Results of each work package / technical objective were inputs or methods used in the following work package. Work packages were consecutive, does not run in parallel. Only Work package 1 providing overall project management and progress reporting run in parallel to all other work packages.

Main technical objectives in work packages were:

**Work package 2 - Airglow study – time and space dynamic of airglow production:** Simulations of airglow production on the global scale in few decades including spectra of produced light to find out response of upper atmosphere to magnetospheric disturbances. Simulations include global maps evaluations (1st phase of Work package 2) to find out appropriate points for airglow monitoring during the geomagnetic storms. Simulations of airglow production evolution on hourly scale for selected appropriate points (2nd phase of Work package 2).

**Work package 3 - Radiation transfer models study:** Realize radiation transfer of produced light together with other light components (zodiacal light and star light) through the atmosphere to Earth's ground. Spectra of light components at the ground allow to evaluate response of ground detectors to incoming light and observability of the changes induced by geomagnetic storms.

**Work package - 4 UV model comparison with available data:** Compare model results with data measured by small network of ground detectors. Data were provided and detectors operation is realized in separate non ESA activity.

The planed timeline of project started in 1. June 2016. Five progress report on quarterly base were planed, all were delivered in planed delivery date. Milestone 1 report with results from Work package 2 was planed and delivered 30.11.2016. ESA approve report and Work package 2 (WP2) as completed. There was no unexpected problems and issues in project activities during the WP2 period. Work package 2 was also delivered in planed date 31.5.2017. Milestone 2 was successfully completed. There was no unexpected problems and issues in project activities during the WP3 period too.

However report from Work package 4 was delivered in planed time, due to insufficient statistics of data from separate activity, no conclusive answer about feasibility to observe ionospheric disturbances by one pixel UV detector was reached. Insufficient number of cloudless dark night periods from half year long measurements at two observation places (Lomnický štít observatory and Stockholm) lead to activity in organizing observations at new places with better meteorological conditions. New simultaneous measurements by one pixel detector start in September 2017 on the two excellent astronomical sites - La Palma (Canary Islands) and Mexico. In parallel we asked ESA for prolongation of project duration by half year. Request was approved by ESA at the start of October 2017. In the extended period we reached reasonably higher statistics of acquired data. On the other hand the additional measurements at observational sites with perfect weather conditions fall to period with almost no geomagnetic storms.

s

From the management point of view all pieces of machinery for planed feasibility study was done/delivered. Models, models results, methods for analysis were delivered and finally also measurements are ongoing as is needed. Conclusive result was finally hampered by very quiet geomagnetic period in last months. Progress report from extended period was delivered at the end of extended period (24. April 2018).

Because current measurements indicate that ionospheric disturbances are visible in airglow light produced by upper atmosphere, we wish to continue in this research in next follow-up project. Final report and other final deliverables were delivered at 11. May 2018.

The deliverables and delivery times are summarized in the following table.

*Table 5.1. Project deliverables status*

<b>Deliverable Identifier</b>	<b>Title/ Description</b>	<b>Original Delivery Date</b>	<b>Planned Delivery Date</b>	<b>Associated Milestone</b>	<b>Status</b>
PR 1.1	1st Progress report / WP2 – progress report	31.8.2016	31.8.2016		Delivered
D2.1	Airglow production report / WP2 –review of airglow study	30.11.2016	30.11.2016	Milestone 1	Delivered
PR 1.2	2nd Progress report / WP2 –progress report	30.11.2016	30.11.2016		Delivered
PR 1.3	3rd Progress report / WP3 - progress report	28.2.2017	28.2.2017		Delivered
D3.1	Radiation transfer models review / WP3 - review of radiation transfer study	31.5.2017	31.5.2017	Milestone 2	Delivered
PR 1.4	4th Progress report / WP3 - progress report	31.5.2017	31.5.2017		Delivered
D4.1	UV background data analysis report / WP4 - review of data analysis	31.8.2017	31.8.2017		Delivered
PR 1.5	5th Progress report / WP4 - progress reports	31.8.2017	31.8.2017		Delivered
PR 1.6	5th Progress report / WP4 - progress reports of prolonged project period	-	24.4.2018		Delivered
Final report	Final report / WP1 - final report	31.10.2017	31.04.2018	Final Review	Delivered
Technical Data Package	Technical notes / WP2&WP3&WP4 - technical notes	31.10.2017	31.04.2018	Final Review	Delivered
Executive Summary Report	Project Executive Summary Report / ESR - summarized outcomes of each WP	1.11.2017	31.04.2018	Final Review	Delivered

## 6. Conclusion

During the first phase of Work package 2 (Section 2) we evaluated the global maps of airglow production with one month time step for 25 years long period. The maps were produced for measured/empirical input parameters and for input parameters characteristic for non and very disturbed magnetosphere. The maps analysis shows that the airglow production at higher latitudes is more sensitive to the magnetospheric disturbances. On the other hand, at high latitudes, the airglow observations could be hampered by auroral lights. This leads to selection of optimal points for observation of airglow changes induced by geomagnetic activity at auroral ovals positions for very disturbed magnetosphere ( $K_p=8$ ). This selection is a compromise between as most high latitude position as possible and reasonably equatorward position to not be influenced by auroral lights. For selected positions on auroral ovals (around north hemisphere auroral oval 10 position and another 10 at the south hemisphere auroral oval) and seven other selected positions, we evaluated airglow production with one hour step during nights from 42 years. Two of seven selected points were located relatively close (geomagnetic latitude  $\sim 45^\circ$ ) to auroral oval (Slovakia, Utah) and some points were located away from auroral oval (more than  $10^\circ$  of geomagnetic latitude) to understand airglow behavior out of auroral oval. Svalbard (Norway) was chosen to cover higher geomagnetic latitude position and Canary Island to cover lower geomagnetic latitude position. Also positions which could be used alternatively for the detectors location were included: Zelenchukskaya District (Russia), Aragats (Armenia) and Pierre Auger Observatory (Argentina). We developed method called Slope method to analyze and quantify average effect of geomagnetic disturbances on airglow production data represented by simulated time series. Based on realized simulations and following analysis results we conclude that airglow production decreases during the magnetospheric disturbances by tens percents. The change of airglow production with change of global geomagnetic Dst index is clearly seen from Slope method results. The 1 nT change of geomagnetic Dst index leads to 0,45-0,85 % change in produced airglow intensity for moderate storms at auroral oval positions (for  $K_p=8$ ).

The Work package 3 (Section 3) consists of two main parts. In the first part, we have described the basics of the radiative transfer topic and we have presented why the libRadtran model is a suitable tool for calculation of the radiative transfer from the top of the atmosphere to the ground. We have analyzed all main atmospheric conditions and their influence to the transmitting UV light. We can conclude, that according model of radiative transfer, the variations of the atmospheric conditions should not preclude the detection of ionospheric disturbances by observation of airglow intensity with one pixel UV detector. However, there is a one exception - presence of clouds - that need to be seriously monitored. To estimate the portion of measurements that might be possible during the year, we have assessed clear sky probability for the particular observational sites. This fact will need to be taken into account in the selection of the future observational sites. We have discussed possible variations of permanent astronomical UV light sources - starlight and zodiacal light. According this analysis, we can assume the constant spectrum of these sources. We have also provided a brief overview of successful detections of space weather impacts in airglow measurements by other authors that indicates possibility to detect geomagnetic storms by airglow measurements. In the second part, we have evaluated airglow spectra at ground level for selected observation sites and we have justified possibility to observe geomagnetic disturbances by one pixel UV detector. The best observation conditions are localized at higher latitudes (Sweden). Still satisfying condition ( $\sim 10\%$  relative change) are at Lomnicky stit position. Observations at lower latitudes could be more problematic, but not impossible, based on model predictions. However these sites have advantage in statistics. Based on this analysis, Aragat and Zelenchukskaya positions were considered as not optimal for ground detector location. Improvement of detector sensitivity to geomagnetic storms effects on airglow light production could be achieved by observation in optimal

wavelength ranges. In comparison with 300-500 nm sensitivity range of one pixel UV detector, relative changes in observed light intensity are more easily detected in 300-400 nm region and at narrow region including 557 nm emission line. However improvement is ~60% for 300-400 nm region and 100% in 10 nm observation window around 557 nm emission line for Lomnický štit station. For moderate storm with Dst change about -50nT it is improvement from one pixel UV detector's 300-500nm 10% average change of light intensity to 16% for 300-400nm and ~20% for 10 nm region with 557 nm emission line.

In the Work package 4 (Section 4), we processed and analyzed the data from four one pixel detectors located on the Lomnický štit Observatory (Slovakia) that operated in the time interval February - August 2017, on location near Stockholm (Sweden) that operated in November 2017 - February 2018, on Observatorio del Roque de Los Muchachos, Baja California in Mexico, and on Observatorio Astronomico Nacional de San Pedro Martir on La Palma (Canary Islands, Spain), that operated in the time interval October 2017 - April 2018. Detailed reduction of the data was performed while we excluded the data affected by the presence of the light from the Sun, Moon, Milky Way and bright stars. We employed also data of cloud coverage to select only these data that were taken during cloudless (clear sky) conditions. These UV airglow intensity measurements were investigated and possible connections to the ionospheric disturbances caused by geomagnetic storms were indicated in 3 periods: 2017/03/26 – 2017/04/04, 2017/05/27 - 2017/06/02, and 2017/07/16 - 2017/07/25. Despite of strong improvements in the data quality by measurements in Mexico and La Palma, the measurement period and hence data therein does not contain enough geomagnetic active periods. Quantification of airglow production sensitivity to the ionospheric disturbances caused by geomagnetic storms was due to this obstacle not established. Nevertheless, all of the results demonstrate that one pixel UV detector is able to detect variations in airglow intensity and so some disturbances in the lower ionosphere. To explain potential sources of these disturbances, two tasks are mandatory. At first we need to precisely filter out all sources of data contamination. This task was performed in our analysis but it needs to be performed in a fully automated way. The second task is a wider understanding of all other processes and phenomena that influence the airglow production. Because current measurements indicate that ionospheric disturbances are visible in airglow light produced by upper atmosphere, we plan to continue in this research in next follow-up project “Follow-up of feasibility study to observe ionospheric disturbances by airglow monitoring network (AMON-net)” that has been recommended for implementation within AO/1-8673/16/NL/Nde.

## References

- Ahn, M.-H. et al., 2015, A cloud detection algorithm using the downwelling infrared radiance measured by an infrared pyrometer of the ground-based microwave radiometer, *Atmos. Meas. Tech.*, 8, 553
- Anderson, G., Clough, S., Kneizys, F., Chetwynd, J., and Shettle, E.: 1986, AFGL atmospheric constituent profiles (0-120 km), Tech. Rep. AFGL-TR-86-0110, Air Force Geophys. Lab., Hanscom Air Force Base, Bedford, Mass
- Bag, T., Singh, V., Sunil Krishna, M. V.: 2017, Study of atomic oxygen greenline dayglow emission in thermosphere during geomagnetic storm conditions, *Advances in Space Research*, 59, 302
- Berk, A., Anderson, G., Acharya, P., Bernstein, L., Muratov, L., Lee, J., Fox, M., Adler-Golden, S., Chetwynd, J., Hoke, M., Lockwood, R., Cooley, T., and Gardner, J.: 2005, MODTRAN5: a Reformulated Atmospheric Band Model with Auxiliary Species and Practical Multiple Scattering Options, in: *Multispectral and Hyperspectral Remote Sensing Instruments and Applications II*, no. 5655 in Proc. SPIE Int. Soc. Opt. Eng., pp. 88
- Bernstein, R. A., Freedman, W. L., & Madore, B. F.: 2002, The First Detections of the Extragalactic Background Light at 3000, 5500, and 8000 Å. II. Measurement of Foreground Zodiacal Light, *Astrophys. J.*, 571, 85
- Cahalan, R., Oreopoulos, L., Marshak, A., Evans, K., Davis, A., Pincus, R., Yetzer, K., Mayer, B., Davies, R., Ackerman, T., H.W., B., Clothiaux, E., Ellingson, R., Garay, M., Kassianov, E., Kinne, S., Macke, A., O'Hirok, W., Partain, P., Prigarin, S., Rublev, A., Stephens, G., Szczap, F., Takara, E., Varnai, T., Wen, G., and Zhuraleva, T.: 2005, The International Intercomparison of 3D Radiation Codes (I3RC): Bringing together the most advanced radiative transfer tools for cloudy atmospheres, *Bulletin of the American Meteorological Society*, 86, 1275
- Chandrasekhar, S.: 1960, *Radiative Transfer*, Dover, New York
- Deutsch, K. A. & Hernandez, G.: 2003, Long-term behavior of the OI 558 nm emission in the night sky and its aeronomical implications, *J. Geophys. Res.*, 108, A12, 1430
- Didebulidze, G. et al.: 2011, Long-term changes in the nightly behaviour of the oxygen red 630.0 nm line nightglow intensity and trends in the thermospheric meridional wind velocity, *International Journal of Remote Sensing*, 32, 11, 3093
- Feister, U. & Grewe, R.: 1995, Spectral albedo measurements in the UV and visible region over different types of surfaces, *Photochemistry and Photobiology*, 62, 736
- Fishkova, L.M.: 1983, *The Night Airglow of the Earth Mid-latitude Upper Atmosphere*, Metsniereba Publ. House, Tbilisi (in Russian)
- Gerasopoulos, E., Amiridis, V., Kazadzis, S., Kokkalis, P., Eleftheratos, K., Andreae, M. O., Andreae, T. W., El-Askary, H., and Zerefos, C. S.: 2011, Three-year ground based measurements of aerosol optical depth over the Eastern Mediterranean: the urban environment of Athens, *Atmos. Chem. Phys.*, 11, 2145
- Gonzalez, W. D., Joselyn, A., Kamide, Y., Kroehl, H. W., Rostoker G., Tsurutani, B. T., and Vasyliunas, V. M.: 1994, What is a geomagnetic storm?, *Journal of Geophysical Research*, 99, A4, 5771

- Gordley, L.L., Marshall, B.T., and Allen Chu, D.: 1994, Linepak: algorithms for modeling spectral transmittance and radiance, *Journal of Quantitative Spectroscopy & Radiative Transfer*, Vol. 52, No. 5, pp. 563
- Hess, M., Koepke, P., and Schult, I.: 1998, Optical Properties of Aerosols and Clouds: The Software Package OPAC, *Bulletin of the American Meteorological Society*, 79, 831–844
- Hofzumahaus, A., Kraus, A., Kylling, A., and Zerefos, C.: 2002, Solar actinic radiation (280-420 nm) in the cloud-free troposphere between ground and 12 km altitude: Measurements and model results, *J. Geophys. Res.*, 107, 10.1029/2001JD900142,
- Jin, Z., Charlock, T.P., Rutledge, K., Stamnes, K., and Wang, Y.: 2006, Analytical solution of radiative transfer in the coupled atmosphere–ocean system with a rough surface, *Applied Optics*, Vol. 45, No. 28
- Kurucz, R.L.: 1992, Synthetic infrared spectra, in *Infrared Solar Physics*, IAU Symp. 154, edited by D.M. Rabin and J.T. Jefferies, Kluwer, Acad., Norwell, MA
- Leinert, C., Bowyer, S., Haikala, L. K., et al.: 1998, The 1997 reference of diffuse night sky brightness, *Astron. Astrophys. Suppl. Ser.* 127, 1-99
- Leonovich, L.A., Mikhalev, A.V., and Leonovich, V.A.: 2011, The 557.7 and 630 nm Atomic Oxygen Midlatitude Airglow Variations Associated with Geomagnetic Activity, *Atmospheric and Oceanic Optics*, 24, 4, 396
- Leonovich, L.A., Mikhalev, A.V., and Leonovich, V.A.: 2012, Covariations in atomic oxygen emissions and ionospheric total electron content during geomagnetic storms, *Journal of Atmospheric and Solar-Terrestrial Physics*, 80, 247
- Makela, J. J., et al.: 2014, Storm time response of the midlatitude thermo-sphere: Observations from a network of Fabry-Perot interferometers, *J. Geophys. Res. Space Physics*, 119, 6758
- Mayer, B., Seckmeyer, G., and Kylling, A.: 1997, Systematic long-term comparison of spectral UV measurements and UVSPEC modeling results, *Journal of Geophysical Research*, 102, 8755
- Mayer, B. and Kylling, A.: 2005, Technical note: The libRadtran software package for radiative transfer calculations – description and examples of use, *Atmos. Chem. Phys.*, 5, 1855
- Mayer, B.: 2009, Radiative transfer in the cloudy atmosphere, *Eur. Phys. J. Conferences*, 1, 75
- Melo, S.M.L., Takahashi, H., Clemesha, B.R.: 1996, The O<sub>2</sub> Herzberg I bands in the equatorial nightglow, *Journal of Atmospheric and Solar-Terrestrial Physics*, 59, 3, 295
- Noll, S., Kausch, W., Barden, M., et al.: 2012, An atmospheric radiation model for Cerro Paranal, *Astron. Astrophys.*, 543, A92
- Ogawa T., Iwagami N., Nakamura M., Takano M., Tanabe H., Takechji A., Miyashita A. and Suzuki K.: 1987, A simultaneous observation of the height profiles of the night airglow OI 5577 Å, O<sub>2</sub> Herzberg and atmospheric bands, *J Geomag. Geoelectr.*, 39, 211
- Patat, F.: 2008, The dancing sky: 6 years of night-sky observations at Cerro Paranal, *Astron. Astrophys.*, 481, 575
- Rayleigh, L., & Jones, H.S.: 1935, The Light of the Night-Sky: Analysis of the Intensity Variations at Three Stations, *Proceedings of the Royal Society of London. Series A, Mathematical and Physical Sciences*, 151, 872, 22

- Reid, I. M., Spargo, A. J., and Woithe, J. M.: 2014, Seasonal variations of the nighttime O(1S) and OH (8-3) airglow intensity at Adelaide, Australia, *J. Geophys. Res. Atmos.*, 119, 6991
- Ricchiazzi, P., Yang, S., Gautier, C., and Sowle, D.: 1998, SBDART: A research and Teaching software tool for plane-parallel radiative transfer in the Earth's atmosphere, *Bulletin of the American Meteorological Society*, 79, 2101–2114.
- Rosenfeld, D. and Lensky, I. M.: 1998, Satellite-based insights into precipitation formation processes in continental and maritime convective clouds. *Bull. Amer. Meteor. Soc.*, 79, 2457-76
- Rozanov, A., Rozanov, V., Buchwitz, M., Kokhanovsky, A., Burrows, J.P.: 2005, SCIA TRAN 2.0 – A new radiative transfer model for geophysical applications in the 175–2400 nm spectral region, *Advances in Space Research*, 36, 1015
- Shettle, E.: 1989, Models of aerosols, clouds and precipitation for atmospheric propagation studies, in: Atmospheric propagation in the uv, visible, ir and mm-region and related system aspects, no. 454 in AGARD Conference Proceedings
- Silverman, S.M., Ward, F., Shapiro, R.: 1962, The Correlation between the 5577 Å Night Airglow Intensity and Geomagnetic Activity, *Journal of Geophysical Research*, 67, 6, 2255
- Silverman, S. M.: 1970, Night airglow phenomenology, *Space Sci. Rev.*, 11, 341
- Slanger, T.G., Cosby, P.C., Huestis, D.L.: 2004, Co-variation of nightglow emission from the O<sub>2</sub>(A<sup>3</sup>Σ<sub>u</sub><sup>+</sup>) and O<sub>2</sub>(c<sup>1</sup>Σ<sub>u</sub><sup>-</sup>) states and the oxygen green line, observed with the Keck I/II telescopes, *Journal of Atmospheric and Solar-Terrestrial Physics*, 66, 617
- Stamnes, K., Tsay, S.C., Wiscombe, W., and Jayaweera, K.: 1988, Numerically stable algorithm for discrete-ordinate-method radiative transfer in multiple scattering and emitting layered media, *Appl. Opt.*, 27, 2502–2509
- Strickland, J.: 1999, “Atmospheric Ultraviolet Radiance Integrated Code (AURIC): theory, software architecture, inputs, and selected results”, *Journal of Quantitative Spectroscopy and Radiative Transfer*, 62, 6, 689-742
- Sugiura, M., Kamei, T.: 1991, Equatorial Dst Index 1957-1986, *IAGA Bull.* 40
- Todua, M. and Didebulidze, G.: 2014, Cosmic Factors Influence on the Inter-Annual Variations of the Green 557.7 Nm Line and Red 630.0 Nm Line Nightglow Intensities and their Possible Coupling with Cloud Covering at Abastumani (41.75°N, 42.82°E), *Acta Geophysica*, 62, 381
- Wilson A.M., Jetz W.: 2016, Remotely Sensed High-Resolution Global Cloud Dynamics for Predicting Ecosystem and Biodiversity Distributions. *PLoS Biol* 14(3): e1002415. doi:10.1371/journal.Pbio.1002415. Data available on <http://www.earthenv.org/cloud>
- World Data Center for Geomagnetism Kyoto, Real-time Dst index, <http://wdc.kugi.kyoto-u.ac.jp/dstae/index.html>, (accessed April, 2018)